FACULTY
OF MATHEMATICS
AND PHYSICS
Charles University

DOCTORAL THESIS

Patrik Švančara

Experimental investigations of liquid helium flows

DEPARTMENT OF LOW TEMPERATURE PHYSICS

Prague 2021

I declare that I carried out this doctoral thesis independently, and only with the cited sources, literature and other professional sources. It has not been used to obtain another or the same degree.

I understand that my work relates to the rights and obligations under the Act No. 121/2000 Sb., the Copyright Act, as amended, in particular the fact that the Charles University has the right to conclude a license agreement on the use of this work as a school work pursuant to Section 60 subsection 1 of the Copyright Act.

In .... date ....
                                             Author's signature

Title
Experimental investigations of liquid helium flows

Author
Patrik Švančara

Department
Department of Low Temperature Physics

Supervisor
doc. Dr. Marco La Mantia, Ph.D.
Department of Low Temperature Physics

Abstract
Selected turbulent flows of He II, the superfluid phase of liquid ^{4}He, are investigated experimentally. The second sound attenuation technique is employed to directly probe the tangle of quantized vortices, thin topological defects within the superfluid, while relatively small particles made of solid hydrogen are dispersed in He II to visualize the overall flow of the liquid via the particle tracking velocimetry. Considering the known particle-vortex interaction mechanisms, steady thermal counterflow in a square channel is investigated. Significant inhomogeneity of the vortex tangle density along the channel height (near the flow-generating heater) is shown to develop. The means of energy transport in turbulent flows of He II are found strikingly different from those taking place in turbulent flows of viscous fluids. Moreover, individual particles in counterflow are observed to intermittently switch between two distinct motion regimes along their trajectories. The regimes are identified and qualitatively described. Steady counterflow jets in He II are realized and the spatial arrangement of the underlying vortex tangle is explored. Finally, macroscopic vortex rings are thermally generated and observed in He II. A method for tracking their propagation in the fluid is developed and their dynamics is shown to be classical-like. The quantized vortex tangle present in the rings and their turbulent wakes is found to be self-similar, highly reproducible, but non-trivial to interpret.

Acknowledgements

Contents

Preface

The phenomenon of fluid turbulence is ubiquitous in Nature. For example, turbulent flows occur during some chemical reactions, they are essential for the mixing of pollutants in the atmosphere, the weather and climate formation and even the formation of the stars.

Instead of defining what is turbulence, it is preferred to describe it by the set of properties it possesses [1]. Turbulent flows of classical viscous fluids are irregular, rotational and to some extent chaotic; the instabilities tend to grow in time, due to a nonlinearity embedded in the Navier-Stokes equation, the fluid's equation of motion. The resulting flow features an extremely large number of interacting degrees of freedom and includes a wide range of length or time scales. Naturally, such system imposes a challenge for theoretical description and experimental observation. Large experimental facilities and computationally expensive tools are employed to capture all the relevant scales, starting from the large scales at which the energy is usually supplied, until the smallest scales, at which the same energy is dissipated by viscosity.

A surprising order emerges when turbulence is described statistically. If we consider steady, three-dimensional turbulence, an ordered flux of energy may establish between the scales. The process is known as the Richardson cascade [2] and is observed in many turbulent flows. Eddies that correspond to the length scale at which the energy is supplied are unstable and constantly break into smaller ones, transferring the energy from larger to smaller scales, until the dissipative scale is reached. In his statistical theory of homogeneous and isotropic turbulence, Kolmogorov [3] argued that the breakup of turbulent eddies is dominated by inertial forces and correctly predicted how the energy is distributed across the scales.

In this work, we study turbulence in the superfluid phase of liquid ^{4}He, historically denoted as He II, to distinguish it from the normal liquid phase called He I. One can obtain He II only in a narrow range of temperatures, starting from the absolute zero ($0\,\mathrm{K}$ or $-273.15\,°\mathrm{C}$) up to ca. $2.2\,\mathrm{K}$. He II is one of the few known quantum fluids, which differ from classical fluids (such as water or air) by the emergence of macroscopic quantum-mechanical effects. A number of unusual and fascinating phenomena is characteristic to He II. For instance, it supports the existence of dissipation-free flows, which can be demonstrated by the ability of the superfluid to flow through fine sinters or narrow cavities [4], impenetrable to viscous fluids. Furthermore, the discovery of fountain and mechano-caloric effects [5, 6] revealed that the pressure and temperature gradients in He II are

coupled together. This hints that the overall mechanism of heat transport is unique to He II [7, 8], having no direct analogue in classical physics.

Quantum coherence of individual helium atoms in the superfluid is usually described by a complex order parameter $\psi(\boldsymbol{x}, t)$, which is a function of space $\boldsymbol{x}$ and time t [9]. Feynman predicted that thin, line-like topological defects of the order parameter may exist in He II [10], which was experimentally confirmed by Vinen [11]. The defects—now called quantized vortices—significantly influence the He II hydrodynamics. With the onset of turbulence, the number and length of quantized vortices grows, eventually forming a vortex tangle. Although the internal structure of the tangle is not yet fully understood, there is evidence that it may develop order and shares some aspects with classical turbulent eddies described above; our aim is to discern these similarities and differences.

The thesis is based on experimental works carried out mostly in Prague and partly in Grenoble. We employ two powerful experimental techniques, the flow visualization, which is based on embedding small solid particles into the fluid and analyzing their flow-induced motions [12], and the attenuation of the second sound waves, i.e., propagative waves of temperature that are characteristic to quantum fluids [13]. Starting from the known interaction between the visualized particles and quantized vortices, we identify signatures of these interactions in the analyzed data, in order to probe the presence and spatial abundance of quantized vortices in turbulent flows of He II. We then focus on thermally activated turbulent jets and macroscopic vortex rings. We probe these spatially inhomogeneous structures by the second sound, in order to describe the spatial arrangement of the underlying vortex tangle. And, in the case of the rings, we successfully combine both experimental techniques to analyze their propagation in He II. Since it is expected that large, coherent structures in He II behave quasi-classically [14], we compare the dynamical properties of superfluid vortex rings with their classical counterparts.

We organize the thesis as follows. In Chapter 1 we introduce the main concepts related to superfluidity and turbulence in quantum fluids. Detailed description of the employed experimental methods provides Chapter 2. Main scientific outcomes of this work are presented and discussed at the same time in the following chapters. We explore steady thermal counterflow in Chapter 3, counterflow jets in Chapter 4 and macroscopic vortex rings in Chapter 5. Finally, in the following Chapter we formulate our conclusions.

The presented results are partially published as research articles in Physical Review B, Physical Review Fluids and the Journal of Fluid Mechanics. These articles are reprinted as Attachments.

1 Superfluidity and quantum turbulence

Basic physical principles related to the dynamics of superfluid ^{4}He are introduced in this chapter. Fundamental properties of He II are summarized in §1.1. Quantum turbulence, i.e., the turbulent state of He II, is described in §1.2, with the focus primarily on thermally driven flows. The relation between quantum and classical turbulence is discussed in §1.3.

1.1 Properties of superfluid ^{4}He

Phase diagram of ^{4}He, displayed in the left panel of Fig. 1.1, reveals existence of a solid, gaseous and two liquid phases. We distinguish the normal liquid phase (He I) and the superfluid phase (He II), which are separated by the second-order phase transition (yellow line). It is often called the lambda transition, since the temperature dependence of the specific heat resembles the Greek letter λ drawn across the transition temperature T_λ, equal to ca. $2.17\,\mathrm{K}$ (yellow point) at the pressure of saturated vapours (red line).

The two-fluid model provides a useful macroscopic description of He II at finite temperatures [15–17]. It postulates existence of two interpenetrating components, which together constitute He II. The normal component represents the gas of thermal excitations and it behaves as it were a viscous fluid; the normal component also carries the entire entropy content of He II. On the other hand, the superfluid component has zero entropy and viscosity, and it is related to the quantum-mechanical ground state of ^{4}He atoms. Densities of both components, ρ_n and ρ_s, steeply depend on temperature. We plot their relative density as the function of temperature in the right panel of Fig. 1.1. At T_λ, He II only consists of the normal component. But, as the temperature decreases, the normal component is gradually replaced by the superfluid one until $\approx 1\,\mathrm{K}$, where He II is almost entirely composed of the superfluid component. At lower temperatures, a hydrodynamic description of the normal component is no longer adequate [9], because the mean free path of thermal excitations gradually becomes comparable to any large scale considered, such as the size of the container. Note that the total density of He II, $\rho = \rho_\mathrm{n} + \rho_\mathrm{s} \approx 145\,\mathrm{kg/m^3}$ is nearly temperature independent between $1\,\mathrm{K}$ and T_λ [18].

The two-fluid framework introduces two independent velocity fields, denoted $\boldsymbol{v}_\mathrm{n}$
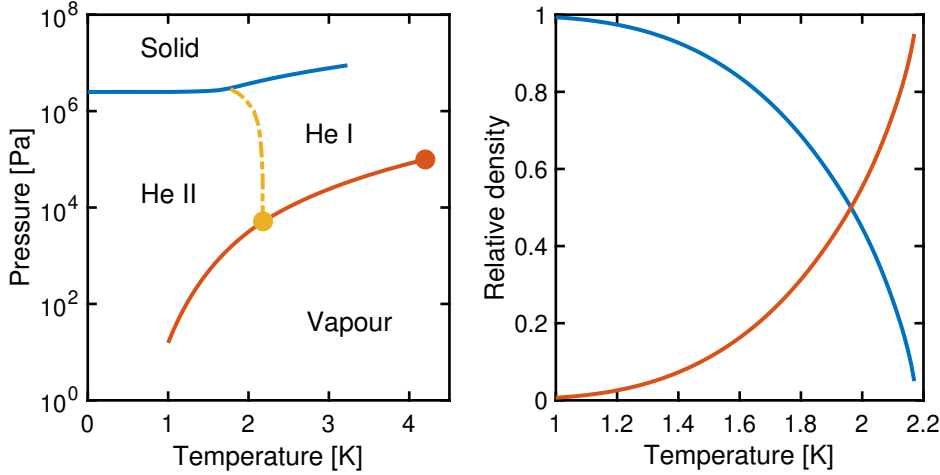
Figure 1.1: *Left panel:* phase diagram of ^{4}He. Red point: boiling point at the atmospheric pressure (≈ 4.2 K). Yellow dot-dashed line: lambda transition. Yellow point: lambda point at the pressure of saturated vapours (≈ 2.17 K). *Right panel:* temperature dependence of the normal fluid fraction ρ_n/ρ (red) and the superfluid fraction ρ_s/ρ (blue line). Data from Refs. [8, 18].

and $\boldsymbol{v}_\mathrm{s}$ for the normal and superfluid component, respectively. The superfluid velocity is coupled to the phase p of the macroscopic quantum order parameter $\psi \sim \mathrm{e}^{ip}$ as [14]

$$\boldsymbol{v}_\mathrm{s} = \frac{\hbar}{m_4}\nabla p, \tag{1.1}$$

where $\hbar = h/2\pi$ is the reduced Planck constant and m_4 denotes the mass of the ^{4}He atom. In consequence, the flow of the superfluid component is not only inviscid, but also potential ($\nabla \times \boldsymbol{v}_\mathrm{s} \equiv 0$). The circulation of the superfluid component, integrated along a closed path $\mathcal{P}$, must be then quantized [9]:

$$\Gamma_\mathrm{s} = \oint_\mathcal{P} \boldsymbol{v}_\mathrm{s} \cdot \mathrm{d}\boldsymbol{\ell} = \frac{\hbar}{m_4} \oint_\mathcal{P} \nabla p \cdot \mathrm{d}\boldsymbol{\ell} = n\kappa, \tag{1.2}$$

where n is an integer and $\kappa = h/m_4 = 9.96 \cdot 10^{-8}\,\mathrm{m^2/s}$ is called the quantum of circulation. Requirement on ψ to be singly-valued in every point in space implies that Γ_s can be nonzero ($n \neq 0$) only in multiply connected regions,[1] that is, in the presence of topological defects. We call these defects quantized vortices, as they can be imagined as one-dimensional[2] vortex lines with the superfluid component circulating around them.

In the simplest case of one straight vortex line, we obtain from Eq. (1.2) that the superfluid velocity field in cylindrical coordinates is $\boldsymbol{v}_\mathrm{s} = n\kappa/(2\pi r)\boldsymbol{e}_\varphi$, where r denotes the radial distance from the vortex and $\boldsymbol{e}_\varphi$ is a unit vector in the azimuthal direction. Kinetic energy of such flow field, per unit length of the

---

[1]Multiply connected is a region that supports existence of closed loops that cannot be contracted to a single point within that region.

[2]Radius of the vortex core is of the order of 1 Å [9], much smaller than any relevant hydrodynamic length scale.

vortex line, is equal to

$$\mathcal{E}_v = \int\limits_{a_v}^{A_v} \pi \rho_{\mathrm{s}} v_{\mathrm{s}}^2 r \, \mathrm{d}r = \frac{n^2 \rho_{\mathrm{s}} \kappa^2}{4\pi} \ln\left(\frac{A_v}{a_v}\right), \qquad (1.3)$$

where $a_v \approx 1\,\text{Å}$ is the radius of the vortex core and A_v denotes either the size of the fluid container or the characteristic distance between the quantized vortices in the container [9]. Since the energy is proportional to n^2, it is energetically favourable for all vortices to be singly quantized ($n = 1$). The vortices are further constrained by the Kelvin theorem [9]. Vortex lines must originate either on the container walls or on the free surface of the liquid; they may also exist in the form of closed vortex loops.

The presence of quantized vortices in He II provides a coupling mechanism between the normal and superfluid components. Origin of this interaction lies in the scattering of quasiparticle excitations off vortex lines, which results in a macroscopic force called mutual friction. Since the force is proportional to $(\boldsymbol{v}_{\mathrm{n}} - \boldsymbol{v}_{\mathrm{s}})$, the friction couples together the otherwise independent velocity fields [9]. Note that this force plays an important role in the dynamics of turbulent He II flows, or during the formation of turbulent jets and vortex rings, discussed in §4 and §5 of this work.

1.2   Quantum turbulence in He II

New quantized vortices nucleate intrinsically or extrinsically. Intrinsic nucleation is opposed by a potential barrier related to a relatively large critical flow velocity, of the order of $10\,\mathrm{m/s}$, which can be induced in He II, e.g., by a fast-moving ion [19]. On the other hand, extrinsic nucleation from the already existing vortex lines[3] requires considerably smaller velocities than the former one, of the order of $10^{-2}\,\mathrm{m/s}$ [9,19]. By the action of the flow, the vortex lines are subjected to twisting and reconnections, which results in the generation of vortex loops that diffuse and collide with the surrounding vortices. These processes eventually lead to the growth of the overall line length in the volume of He II and the formation of a vortex tangle, the main ingredient of quantum turbulence.

In general, the term quantum turbulence is used to describe the turbulent state of a quantum fluid. In He II, it accounts for the dynamics of the vortex tangle, the flow of the normal and superfluid components and their mutual interaction. Transition to turbulence may occur in the two components of He II independently [9], which means, for example, that a turbulent vortex tangle can develop alongside the laminar flow of the normal component.

Experimentally, turbulence in He II can be generated, e.g., by mechanical stirring [20], by towing or oscillating a grid [21,22], by macroscopic or microscopic electromechanical resonators [23,24] or thermally [25].

---

[3]First quantized vortices form in He II, e.g., by the Kibble-Zurek mechanism during the superfluid transition [19].

The flow of He II driven by heat—called thermal counterflow—is unique to quantum fluids and owes its existence to their two-fluid nature. Thermal counterflow is typically obtained by the dissipation of heat at the closed end of a channel fully submerged in the liquid and open to the bath at the opposite end. Applied heating power P deposits entropy inside the channel with the rate $\mathrm{d}S/\mathrm{d}t = P/T$, where T denotes thermodynamic temperature. At the same time, the flow of the normal component with an average velocity v_n is established, and transports the produced entropy into the bath with the rate equal to $\rho s v_\mathrm{n} \mathcal{A}$, where s denotes the specific entropy of He II and $\mathcal{A}$ is the channel cross section. In the steady state, the production and transport terms are equal, which allows to derive a relation for the normal fluid velocity,

$$v_\mathrm{n} = \frac{q}{\rho s T}, \tag{1.4}$$

where we denote by $q = P/\mathcal{A}$ the corresponding heat flux. The outflow of the normal component from the channel is compensated by the inflow of the superfluid one, so that the net mass flow rate remains zero (i.e., $\rho_\mathrm{n} \boldsymbol{v}_\mathrm{n} = -\rho_\mathrm{s} \boldsymbol{v}_\mathrm{s}$). Therefore, the two components of He II are found to flow, on average, in opposite directions, and their relative velocity (called counterfow velocity) can be expressed as

$$v_\mathrm{ns} = |\boldsymbol{v}_\mathrm{n} - \boldsymbol{v}_\mathrm{s}| = v_\mathrm{n}\left(1 + \frac{\rho_\mathrm{n}}{\rho_\mathrm{s}}\right) = \frac{q}{\rho_\mathrm{s} s T}. \tag{1.5}$$

Due to the outlined mechanism of heat transport, a temperature gradient ∇T is established along the channel length. For small enough heat fluxes, i.e., for small values of v_ns, the gradient is proportional to the applied heat flux (Landau regime) [7]. However, above some critical q, the scaling changes to $\nabla T \sim q^3$ (Gorter-Mellink regime) [26]. The latter regime can be explained by the onset of quantum turbulence; the formation of a dense vortex tangle decreases efficiency of the heat transport and the resulting heat conductivity of He II actually becomes dependent on the applied heat flux [7].

A straightforward parameter used to characterize the vortex tangle is the vortex line density (VLD) L, defined as the length of quantized vortex lines in a unit volume. This quantity is associated with the length scale ℓ defined as

$$\ell = \frac{1}{\sqrt{L}}, \tag{1.6}$$

which is usually interpreted as the mean distance between quantized vortices.

Experimentally determined scaling of VLD in steady channel counterflow can be written as [27]

$$L = \gamma^2 \left(v_\mathrm{ns} - v_\mathrm{c}\right)^2, \tag{1.7}$$

where γ denotes an empirical parameter that depends on temperature and the channel geometry, and its value is of the order of $10^6 \,\mathrm{s/m^2}$ [28]. We consistently use values of γ reported in Ref. [29], which are obtained from numerical simulations [30] and are in a relatively good agreement with the experiments. Critical velocity v_c is of the order of $1\,\mathrm{mm/s}$ and its exact value depends on the channel size and shape [31].

Different scaling of the vortex line density is observed in experiments where turbulence is generated mechanically. In this case, it is thought that the normal and superfluid components are locked into a single velocity field by the action of the mutual friction, i.e., $\boldsymbol{v}_\text{n} \approx \boldsymbol{v}_\text{s}$, and it holds that [27, 32]

$$L \sim v^{3/2}, \tag{1.8}$$

where v denotes the flow velocity.

1.3 Relation to classical turbulence

Quantization of circulation is the key aspect that divides the classical and superfluid turbulence[4] on a fundamental level. In the classical case, the vortices are allowed to exist in many sizes and strengths and vorticity is a continuous field. In the superfluid case, the vortices are all alike and the turbulent state of the fluid is characterized only by the spatial configuration of the vortex tangle. Despite this difference, there are numerous situations when vortex lines organize themselves into structures that allow He II to resemble a classical fluid [14].

We take He II under rotation for the famous example of such behaviour. When the container of He II is spun with a constant velocity about its vertical axis, the superfluid will eventually reach the state of a solid body rotation [33] with angular frequency Ω equal to the driving frequency. The related macroscopic vorticity, $\omega = 2\Omega$ is mimicked in the superfluid component by the triangular mesh of vortex lines, which stretch and align parallel to the axis of rotation with the area density of ω/κ vortex lines; note that the triangular mesh is the lowest energy configuration possible [10]. This phenomenon can be easily checked by the direct visualization of the vortex line array. When we disperse small solid particles in He II, they can decorate individual vortices, making them visible to a camera [34], see §2.1 for more details on the technique.

The ability of the vortex tangle to display quasi-classical features is more general [9, 14]. Coherent, metastable vortex bundles were identified in numerical simulations of superfluid turbulence [35] and experimentally, in a wide range of the superfluid density fractions [36]. The vortex bundles are usually polarized, i.e., they mimic larger eddies, which can break into smaller ones in the process analogous to the Richardson cascade. The similarity with classical energy transfer mechanisms is underlined by the emergence of the Kolmogorov energy spectra, found in numerical simulations [35] as well as in experiments [20, 37]. In the latter case, the shapes of the energy spectra acquired in He I and He II were found indistinguishable.

The analogy between classical and quantum turbulence was recently extended by Müller et al. [38]. The authors studied the scale-dependent velocity circulation in numerical simulations of superfluid turbulence. In the range of scales larger than the intervortex distance, they observed the quasi-classical behaviour

---

[4]Term superfluid turbulence is equivalent to quantum turbulence in the zero temperature limit, i.e., at the absence of the normal component.

of turbulence, including the effects of intermittency, which were studied via the higher-order moments of circulation. On the other hand, when the circulation was evaluated at length scales comparable to the intervortex distance, the analogy was lost due to the discrete nature of the quantized vortex tangle.

Moreover, the lack of viscosity in superfluid turbulence requires another small-scale mechanism of energy dissipation. It is thought that the energy is first transferred from the intervortex scales to the Kelvin waves, helical perturbations along the vortex lines [39]. The waves are excited by vortex reconnections and subjected to mutual nonlinear interactions, which generate waves with gradually larger wavelengths, creating a Kelvin wave cascade [40]. The energy is ultimately dissipated into the bath by phonon emission [41], at scales much smaller than ℓ.

The situation becomes more complex when we consider finite temperatures, where both components of He II are present. Due to the mutual friction, the normal-fluid vorticity and the vortex line density are correlated at scales larger than ℓ [42]. Robust locking of the normal and superfluid components is observed along the energy cascade [43], from the energy-containing scale until the dissipation scale, whose value depends on temperature, i.e., on the relative density of the components. Processes that take place in the vicinity of the intervortex distance are still debated in literature [39]. The main obstacle is to find suitable tools to describe the continuous dynamics of classical eddies, alongside with the dynamics of Kelvin waves, as both mechanisms are important in this spectral range. Fully-coupled numerical models of quantum turbulence at finite temperatures are under development [44].

2   Methods of investigation

Two experimental methods employed for the investigation of He II flows are discussed. In §2.1 we introduce the particle tracking velocimetry in the context of similar techniques and approaches towards the cryogenic flow visualization. The second sound attenuation technique and the design of relevant acoustic sensors is summarized in §2.2.

2.1   Particle tracking velocimetry

There is a relatively large number of flow visualization techniques developed by date. Some of them offer a qualitative insight into the studied flow (e.g., the visualization by smoke or ink), others provide quantitative information, usually aimed to determine the underlying velocity field. However, only a few methods are nowadays adapted to visualize the flows of quantum fluids, especially He II. Despite of difficulties related to the optical access to low-temperature vessels, successful realizations of the particle imaging velocimetry (PIV) and particle tracking velocimetry (PTV) techniques in He II are reported in literature [12, 45].

Both methods require small solid particles, which are dispersed in the liquid; their motion, assumed to follow that of the fluid, is observed by a fast digital camera. In PIV, there is no need to resolve individual particles. The obtained images are analyzed by splitting them into small overlapping investigation areas. Local displacement of the fluid and hence the velocity field is estimated from the cross-correlation coefficients, computed between the areas in subsequent camera frames [46]. Note that velocities are estimated in fixed points relative to the camera field of view (FOV).

Various thermally-driven flows described in this work were investigated by PTV, which is a Lagrangian technique. It aims to distinguish individual particles captured by the camera and track their motion in time, that is, between the frames [47]. Information provided by PTV hence consists of a time-dependent velocity, measured along the trajectories of the detected particles.

Tracer particles

Both PIV and PTV techniques rely on the particles to accurately follow the local flow field. We discuss this issue in simplified terms, aiming to roughly

11

determine what properties the particles should possess to be applicable for the visualization of He II flows. The general question of particle motion in a fluid is rather complex [48]; a more detailed analysis of Lagrangian particle dynamics provides, e.g., Ref. [49].

In brief, we require that the particles scatter enough light to be visible by the camera, but they are small enough to promptly respond to the flow of He II. They should also be near to neutrally buoyant to stay long enough in the camera FOV [45]. As we will see, the requirements on the size (we assume in the following that the particles are spheres with radius a) and density ρ_p are only partially met by various particles, due to the low density and viscosity of He II.

Mismatch between ρ_p and the fluid density, ρ_f is responsible for the buoyancy effects. When $\rho_p < \rho_f$, the particles tend to float and when $\rho_p > \rho_f$, the particles sink. In a quiescent fluid, a nonzero buoyancy force results in some settling velocity $\boldsymbol{u}_\infty$, which can be expressed from the equality between the buoyancy and Stokes drag forces:

$$\boldsymbol{u}_\infty = \frac{2a^2 \boldsymbol{g} \left(\rho_p - \rho_f \right)}{9 \mu_f}, \tag{2.1}$$

where $g = |\boldsymbol{g}| = 9.81\,\text{m/s}^2$ is the acceleration due to gravity and μ_f is the fluid dynamic viscosity. Since the density of He II is about $145\,\text{kg/m}^3$ [18], it is difficult to obtain neutrally buoyant particles and one has to frequently consider the particle settling effects [45]. Note, however, that $u_\infty \equiv |\boldsymbol{u}_\infty|$ depends quadratically on the particle radius a, which means that the settling effects are appreciably reduced when the particles are small enough. In practical terms, it is acceptable when the settling velocity is up to a few per cent of the typical velocity of the investigated flow.

Besides settling, one must consider the particle response to fast, turbulent variations of the flow field, which is affected by the particle inertia. Relaxation time of a spherical, neutrally buoyant particle can be expressed as [45]

$$t_{\text{rlx}} = \frac{\rho_f a^2}{3 \mu_f}, \tag{2.2}$$

and it represents the time scale at which the particle equilibrates with the fluid [50]. A typical value of t_{rlx} required to track He II flows is of the order of $1\,\text{ms}$ or less, which limits the particle size to be $10\,\mu\text{m}$ at most [50]. Moreover, we may further require that the particle size is smaller than the mean distance between the quantized vortices ℓ.

The final limitation comes from the used imaging technique. Since the illumination of most particles relies on the Rayleigh scattering, it is required for the sufficient scattering intensity that the particle radius is at least 5λ, where $\lambda \approx 500\,\text{nm}$ is the wavelength of the employed light source. The smallest acceptable particle radius is $a \approx \lambda$ [45].

As we have already mentioned, the main challenge for finding suitable particles is the low density of He II. For example, hollow glass spheres can be prepared to be neutrally buoyant in He II, but their size is usually polydisperse and ranges between $20\,\mu\text{m}$ to over $100\,\mu\text{m}$, which makes them unsuitable for accurate flow

visualization [50]. More promising particles are solid glass and polymer micro-spheres. Despite their large density (ca. $1100 \, \text{kg/m}^3$ [50]), it is possible to prepare them with a narrow size distribution, with the mean radius of the order of a few microns. The small size is here favourable, as it appreciably decreases the particle settling velocity, making them usable for the PIV assessment of He I [51] and He II flows [50, 52, 53]. A promising alternative to these particles represent fluorescent nanospheres [54], which are even smaller ($20 \, \text{nm}$ or $100 \, \text{nm}$) and are made visible to the camera by the laser-induced fluorescence.

A useful source of small and light enough particles are solidified gasses. The production of such particles occurs in-situ, by injecting small amounts of various gasses into the helium bath. Reported are particles made of solid neon [55] and air [56], but the most promising materials seem to be hydrogen isotopes [50]. Indeed, injections of hydrogen (H_2) or deuterium (D_2) gas, diluted with helium to the volume ratio of ca. $1 : 100$, result in micron-sized particles with a relatively narrow size distribution (see below) and relaxation times of the order of $1 \, \text{ms}$ [50].

The density of solid hydrogen, $\rho_{\text{H2}} \approx 88 \, \text{kg/m}^3$ and deuterium, $\rho_{\text{D2}} \approx 200 \, \text{kg/m}^3$, deduced from the parameters of their crystal structure [57], does not match that of He II. Naturally, one may expect that it is possible to obtain neutrally buoyant particles by preparing an adequate H_2–D_2 mixture [58, 59]. However, it is likely that the isotopic composition of the particles obtained from the mixture is not uniform, due to a small difference in the melting temperatures of hydrogen and deuterium (ca. $14 \, \text{K}$ and $19 \, \text{K}$, respectively [60]). More promising are hence particles made of solid deuterium hydride (HD), whose solid-phase density is $\rho_{\text{HD}} \approx 145 \, \text{kg/m}^3$ [57], i.e., practically equal to that of He II. Note that all outlined hydrogen isotopologues are available in our laboratory and their response to similar flows can be directly compared (see, e.g., Ref. [61] or §3.2 of this work).

Direct injections of hydrogen or deuterium mixtures into He II were found to produce large irregular flakes [62]. Therefore, it is preferred to inject the gas into He I and to cool down the experiment below the lambda point once there are enough particles present in the experimental volume [60]. During the experiment, the particles can be resuspended by injections of pure helium gas. Note that the particles slowly coagulate and their overall quality decreases in time [60], which practically limits the duration of a visualization experiment (to approximately three days in our case). After this period, the cryostat needs to be warmed up and evacuated before another cooldown.

Solidified particles are naturally polydisperse; their size distribution depends on the composition and velocity of the injected gas. The size distribution of hydro-gen or deuterium particles can be estimated from their settling velocities. For instance, if we consider a deuterium particle that sinks in quiescent He II with the mean vertical velocity equal to $\langle u_y \rangle$,[5] it follows from Eq. (2.1) that its radius is

$$a = \sqrt{\frac{9\mu_{\text{n}} \langle u_y \rangle}{2g \left(\rho_{\text{D2}} - \rho \right)}}. \tag{2.3}$$

---

[5] We assume that the mean velocity is measured after the terminal settling velocity is reached by the particle.

13

Fig. 2.1 displays the typical size distribution of deuterium particles estimated by the outlined method. The mean particle radius here is $3.7\,\mu$m and $97\,\%$ of all particles are smaller than $10\,\mu$m.
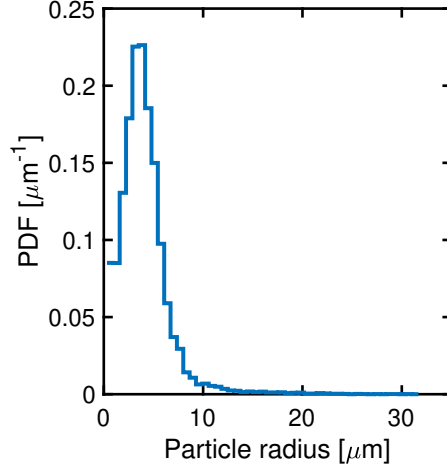
Figure 2.1: Probability density function (PDF) of particle radii a, typically achieved in our experimental set up. The particles are made of solid deuterium and their size was estimated by measuring their settling velocity in quiescent He II, see Eq. (2.3). Velocity measurements were carried out at $(1.68 \pm 0.01)\,$K, at least $30\,$s after the resuspension pulse of pure He gas. The present data set comprises ca. 14.7 thousand trajectories.

Interaction with He II components

Particles embedded in the fluid are subject to simultaneous interactions with the normal and superfluid components, respectively. If we consider small, spherical, neutrally-buoyant particles, their equation of motion can be written as [63]

$$\frac{\mathrm{d}\boldsymbol{u}}{\mathrm{d}t} = \frac{1}{t_\mathrm{rlx}}\left(\boldsymbol{v}_\mathrm{n} - \boldsymbol{u}\right) + \left(\frac{\rho_\mathrm{n}}{\rho}\frac{\mathrm{D}\boldsymbol{v}_\mathrm{n}}{\mathrm{D}t} + \frac{\rho_\mathrm{s}}{\rho}\frac{\mathrm{D}\boldsymbol{v}_\mathrm{s}}{\mathrm{D}t}\right), \tag{2.4}$$

where the substantial derivatives are defined as

$$\frac{\mathrm{D}\boldsymbol{v}_\mathrm{n}}{\mathrm{D}t} = \frac{\partial\boldsymbol{v}_\mathrm{n}}{\partial t} + \left(\boldsymbol{v}_\mathrm{n}\cdot\nabla\right)\boldsymbol{v}_\mathrm{n}, \qquad \frac{\mathrm{D}\boldsymbol{v}_\mathrm{s}}{\mathrm{D}t} = \frac{\partial\boldsymbol{v}_\mathrm{s}}{\partial t} + \left(\boldsymbol{v}_\mathrm{s}\cdot\nabla\right)\boldsymbol{v}_\mathrm{s}. \tag{2.5}$$

The advection term on the right-hand side of Eq. (2.4) indicates that the particles interact with the superfluid velocity field, and hence with the tangle of quantized vortices. This interaction is peculiar, since in classical turbulence, it is known that light particles (e.g., air bubbles) tend to concentrate in filamentary regions of a relatively large vorticity [64], while heavy particles form clusters with a different topology [64, 65]. However, the particles of any density are attracted towards the quantized vortices. This effect is neatly observed especially at relatively low temperatures, when the viscous drag of the normal fluid is low enough [66]. Attractive force originates from radial pressure gradients in the vicinity of a vortex line and the corresponding potential can be expressed, for the simple case of a

single, rectilinear vortex, as [63]

$$\Phi(r) = \frac{-\kappa^2}{4\pi^2 r^3}.$$

(2.6)

When the normal-fluid flow is slow enough, it follows from Eq. (2.4) and (2.6) that the attraction towards the quantized vortices becomes important and particles start to interact with the vortex tangle. Specific nature of near encounters between the particles and vortex lines is investigated by numerical simulations, reviewed in Ref. [67]. Here we discuss one possible outcome of such interaction, that is, when a particle gets trapped on the vortex line.

Since the trapped particle displaces the fast-moving superfluid from the quantized vortex, the process is energetically beneficial. It is hence possible to decorate individual vortex lines, which is especially useful for the study of vortex reconnections [56, 68]. Since the binding energy is not very large, the particles tend to switch between the trapped and free states by the local action of the normal-fluid viscous drag [69]. This behaviour is governed by the small-scale structure of quantum turbulence and it was indeed shown that similar particle dynamics is observed for different large-scale flows of He II [69].

We can hence say that the resulting particle dynamics carries information about the quasi-classical, normal-fluid turbulence, but also about the vortex tangle. Hidden signatures of particle-vortex interactions can be then used to investigate the underlying dynamics of the vortex lines, which we discuss in the case of thermal counterflow in §3.
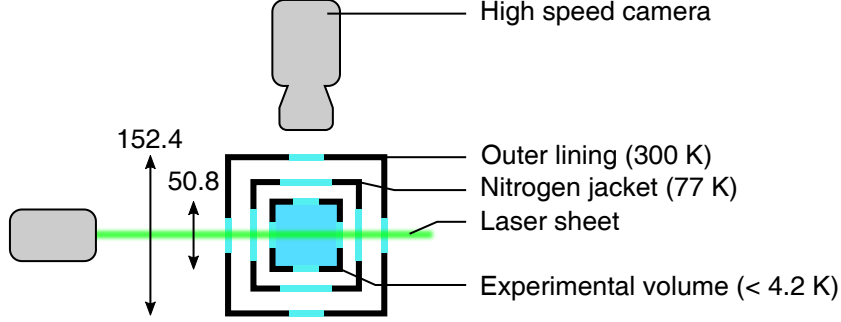
Experimental setup

We employ the cryogenic visualization setup, described in detail in Ref. [60]. Here we summarize its main components. Liquid ^{4}He cryostat is the central part of the apparatus. It consists of an inner helium vessel (ca. 60 L capacity), an intermediate nitrogen jacket, thermally anchored to the liquid nitrogen tank (ca. 30 L of liquid at 77 K) and the outer steel lining. Thermal insulation of the inner vessel is achieved by high vacuum maintained between the individual layers of the cryostat (ca. $5 \cdot 10^{-6}$ torr, further improved by cryopumping), radiative shielding by the nitrogen jacket and layers of superinsulation.

Experimental volume of the cryostat extends from its bottom. This volume has a square cross section with 50.8 mm (2 inch) sides and is 300 mm high. Optical access to the volume is provided by five sets of windows with 25 mm inner diameter. One set of windows is located at the base of the volume, remaining four are mounted on its vertical sides, 100 mm above the bottom window.

In the current setup, sketched in Fig. 2.2, we use three optical ports to perform a two-dimensional PTV. We use a solid-state green laser (Dantec RayPower 5000) and a cylindrical lens to create a relatively thin (≈ 1 mm) laser sheet, crossing the symmetry axis of the experimental volume. Most of the laser power (up to 1 W) passes through the cryostat and is absorbed by a room-temperature screen. When

the particles enter the plane illuminated by the laser sheet, the light scatters off their surface, which makes the particles visible to a high-speed CMOS camera (Vision Research Phantom V12.1) sharply focused to the illuminated plane. This way, the particles can be followed as they move in the illuminated plane, accessing their positions in two spatial dimensions and time.

Figure 2.2: Cross section of the experimental volume, in the plane located 100 mm above its bottom. Dimensions are in millimeters. Light blue: sapphire and quartz windows. Green line: laser sheet, ca. 1 mm thin and 20 mm high, at most. The positions of the laser source and the camera are also sketched (grey).

Stable temperature of the helium bath is maintained by pumping of its vapours. The resulting temperature is given by the pressure of saturated vapours (Fig. 1.1). Such temperature estimation is accurate especially in the superfluid phase, when the fluid is practically isothermal due to the large thermal conductivity of He II. Our pumping system consists of a Roots and rotary vane pumps, connected to the pumping line of the cryostat via a PC-controlled butterfly valve (VAT Series 615). The pressure inside the cryostat is probed by a Pfeiffer and MKS Instruments pressure gauges with the resolution better than 0.1 torr. The position of the valve (from fully closed to fully open) is continuously adjusted by a PID loop that aims for setting a constant pressure inside the cryostat. As a result, we regularly access temperatures between ca. 1.20 K and 2.17 K with the temperature stability of the order of 1 mK.

Additional temperature monitoring is ensured by a pair of Cernox NTC thermometers, read by a Lake Shore 336 temperature controller. One temperature probe is located in the bath, above the experimental volume, while the other one is usually mounted near the flow cell. Calibration of the probes in temperature range from 1.23 K to 4.20 K was carried out in our laboratory, against the pressure of saturated vapours (in this case the thermometers were kept next each other).

Image processing

Particle positions are acquired with the maximum resolution of 1280×800 px (ca. 1 Mpx), with the typical frame rate of several hundred to a few thousand Hz, up to the maximum available rate of ca. 6.3 kHz. Each movie consists typically of a few thousand images, which are first saved into the camera memory, and later downloaded to the data storage as a binary file. The camera receives software

triggers that launch and stop the recording; the latter trigger is executed with a large time precision and it is used to time-stamp the movie, which is useful for its further analysis. The movies are usually recorded via a custom LabVIEW script.

Binary data received from the camera are exported to greyscale tiff images. The images are black, with the particles appearing as small white areas. Example of a composite image with an exceptionally high level of the background noise is displayed in the top panel of Fig. 2.3. We first pre-process these images to remove the static background, mask the visible objects and increase the contrast, see the middle panel of the same figure.

The following step is to detect particles in the individual frames and reconstruct their trajectories. Several methods of detection and the subsequent particle tracking are available; the performance of different algorithms depends on the background noise or particle concentration [70]. Here we chose to employ the MosaicSuite tracking software [71] implemented for the ImageJ and Fiji image processing platforms. In short, individual particles are identified as bright spots in the camera frames and their positions are refined with a sub-pixel resolution. The particles are then linked across the frames into trajectories. In the end, the process yields a list of trajectories that contains two-dimensional particle positions $\boldsymbol{x}(t)$.

The trajectories are then post-processed: we linearly interpolate the missing positions and discard too short trajectories (typically less than 5 points). The final result—individual particle trajectories—are plotted in the bottom panel of Fig. 2.3.

Estimation of velocity and acceleration

The following step is to differentiate the trajectories in order to obtain the particle velocity and acceleration. Perhaps the simplest method of velocity estimation is that of central differences. Velocity $\boldsymbol{u}(t)$ can be computed from the particle positions, $\boldsymbol{x}(t)$ as

$$\boldsymbol{u}(t) = \frac{\boldsymbol{x}\left(t + \tau\right) - \boldsymbol{x}\left(t - \tau\right)}{2\tau}. \tag{2.7}$$

Particle acceleration $\boldsymbol{a}(t)$ is obtained similarly, as the three-point estimate of the second derivative:

$$\boldsymbol{a}(t) = \frac{\boldsymbol{x}\left(t + \tau\right) - 2\boldsymbol{x}\left(t\right) + \boldsymbol{x}\left(t - \tau\right)}{\tau^2}. \tag{2.8}$$

In the equations above, τ denotes the sampling time, equal to the inverse of the camera frame rate.

Numerical differentiation defined by Eq. (2.7) is obviously very simple to implement. However, one has to keep in mind that the resulting velocity (acceleration) estimate is appreciably influenced by experimental noise, as it relies on the measurement of two nearby particle positions. If we consider that the typical accuracy of the tracking algorithm is $\Delta_x \approx 0.1\,\mathrm{px} = 1\,\mathrm{\mu m}$ (reported in Ref. [71] for the
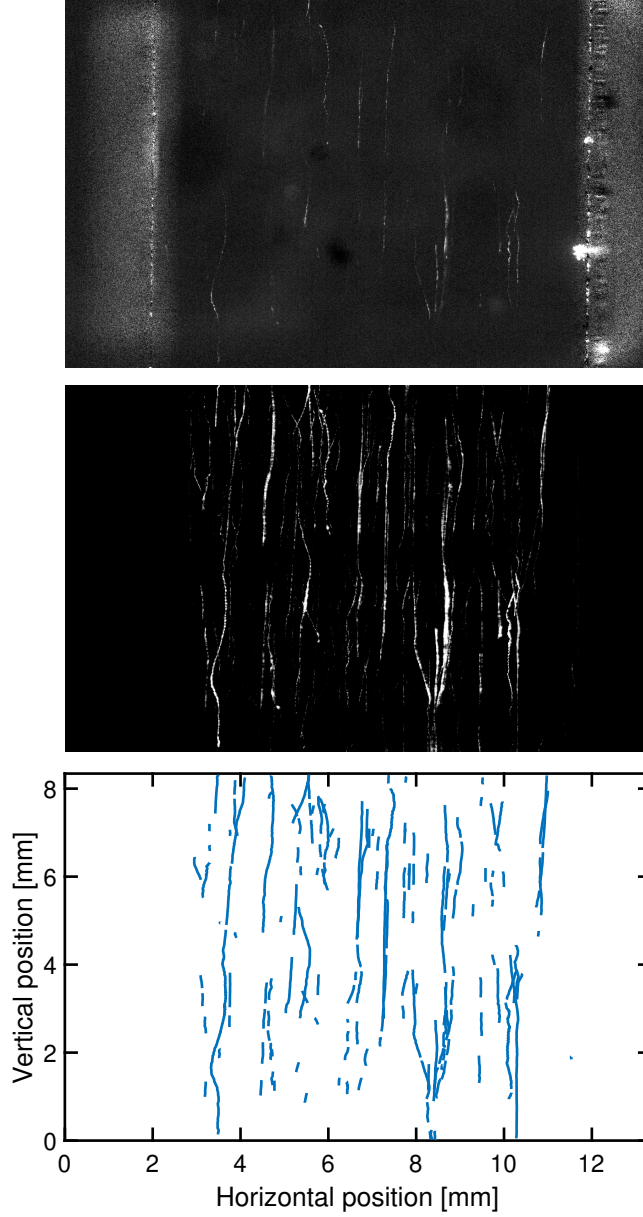
Figure 2.3: Example of the outlined image processing routine. Visualized is thermal counterflow (1.51 K, the normal fluid velocity ca. 5.2 mm/s, particles move up) in a 10 mm wide glass channel. *Top panel:* RMS image obtained from 2000 raw camera frames (camera frame rate is 500 Hz). Pixel intensities are multiplied by 40 for the sake of clarity. Bright reflections on the sides are due to vertical channel walls. *Middle panel:* RMS image obtained from the pre-processed frames. Here we multiply the pixel intensities by 20. *Bottom panel:* post-processed trajectories obtained from the tracking software. 466 tracks are here detected, together containing ca. 16.7 thousand positions. Displayed are only tracks longer than 20 points.

signal-to-noise ratio of ca. 7.5), the absolute error of u can be estimated as $\Delta_u = (\Delta_x + \Delta_x)/(2\tau)$ and its relative error as $\delta_u = \Delta_x/(u\tau)$. Now, for the typical camera frame rate of $1\,\mathrm{kHz}$ ($\tau = 1\,\mathrm{ms}$), requirement for $\delta_u < 1\,\%$ is met only when $u > \Delta_x/(0.01\tau) = 100\,\mathrm{mm/s}$. This means that velocities smaller than $100\,\mathrm{mm/s}$ are estimated with the relative inaccuracy larger than $1\,\%$. Note that this inaccuracy, in fact, grows with the frame rate, because by increasing the frame rate the position difference that enters Eq. (2.7) decreases.

Another approach is to employ noise-suppressing estimators, which are based on the convolution of the particle trajectory with a suitable kernel $K(t)$. If we restrict the kernel to the finite support $[-\beta\tau, \beta\tau]$, where β is a free positive integer, we can perform a discrete convolution with $\boldsymbol{x}(t)$ as follows:

$$[K * \boldsymbol{x}](t) = \sum_{t'=t-\beta\tau}^{t+\beta\tau} K\left(t - t'\right)\boldsymbol{x}(t'). \tag{2.9}$$

Here the vector notation simply means that individual position components are identically processed. Note that, in practical terms, this equation tells us that K is used to assign weigths to multiple subsequent positions, which are then linearly combined.

In this work we specifically use the one-dimensional Gaussian kernel [72], defined as

$$G_0(t) = N_0 \exp\left[-\left(\frac{t}{\alpha\tau}\right)^2\right], \tag{2.10}$$

where α is a free positive parameter that defines the kernel width and N_0 is a normalization factor that depends on α and β, ensuring that the weights assigned by the kernel sum up to 1. G_0 is known as the Gaussian blur, and a convolution of $\boldsymbol{x}(t)$ with G_0 simply smoothens the trajectory, with the smoothing level given by the value of α.

In order to obtain similarly smoothened velocities, we can differentiate the trajectory and convolute it with G_0. However, the same result is obtained directly by convoluting $\boldsymbol{x}(t)$ with the first time derivative of the kernel,

$$G_1(t) = \frac{\mathrm{d}G_0}{\mathrm{d}t} = -N_1\frac{t}{\alpha\tau}G_0(t), \tag{2.11}$$

where N_1 is another normalization factor. By analogy, the particle acceleration is estimated by taking the second time derivative of G_0, i.e.,

$$G_2(t) = \frac{\mathrm{d}^2G_0}{\mathrm{d}t^2} = N_{2a}\left[2\left(\frac{t}{\alpha\tau}\right)^2 - 1\right]G_0(t) + N_{2b}, \tag{2.12}$$

where N_{2a} and N_{2b} are again constant prefactors. Following Ref. [72], we choose such normalization constants that it follows, for a constant trajectory, $x_0(t) = x_0$, a linearly increasing trajectory, $x_1(t) = ut$ and a quadratically increasing trajectory, $x_2(t) = at^2/2$ that:

$$G_1 * x_0 = 0, \qquad\qquad G_2 * x_0 = 0,$$
$$G_1 * x_1 = u, \qquad\qquad G_2 * x_2 = a.$$

We call the functions G_0, G_1 and G_2 position, velocity and acceleration estimators, respectively. In Fig. 2.4 we plot these estimators for $\alpha = 5$ and $\beta = 15$ as an example.
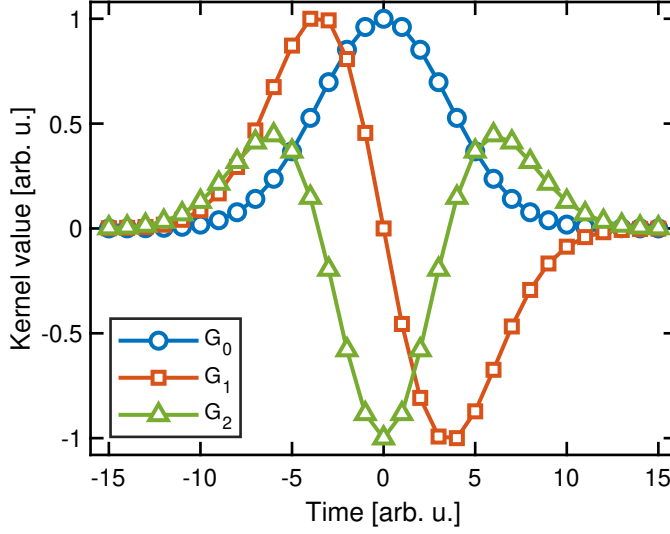
Figure 2.4: Example of estimators G_0, G_1 and G_2, Eq. (2.10)–(2.12), for $\alpha = 5$ and $\beta = 15$. The kernels are rescaled to $[-1, 1]$ interval for the sake of clarity.

Performance of Gaussian estimators was systematically tested and a detailed study is summarized in Ref. [73]. Therein, we compare G_1 with the central difference method by using a single synthetic trajectory, a real trajectory obtained experimentally and a full statistical data set that contains tens of thousands trajectories. Here, we will illustrate the most important features of G_1 with the testing set of particle trajectories, obtained in thermal counterflow (1.95 K, the normal fluid velocity 18.2 mm/s) in a 10 mm wide square glass channel. The mean vertical displacement of the particles between frames is ca. 18 μm, at the camera frame rate of 500 Hz; from this we can estimate that particles move, on average, with the velocity of ca. 8.9 mm/s, in the direction of the normal fluid.

Significant advantage of Gaussian estimators lies in their ability to suppress the noise amplification effects common for numerical differentiation. As we have already stated, the level of smoothing is tuned by the kernel width α. We found that a relatively narrow kernel (say, $\alpha = 3$) is already efficient for an accurate velocity estimation, considering the noise level commonly experienced in our experiments. Although the noise reduction effect further increases with increasing α, one has to be cautious, because the use of too wide kernels decreases the algorithm's ability to resolve sudden position changes, i.e., events of large particle velocity, which are important features of quantum turbulence [74].

Taking the testing data, we find that the standard deviation of the particle vertical velocity decreases as α increases, see the left panel of Fig. 2.5. In this example, the velocities are computed from individual trajectories by using G_1, parametrized by different values of α (between 0.1 and 7) and fixed $\beta = 10$. Constant width of the kernel support ensures that the resulting set of velocities contains the same number of points, equal to ca. 1.88 million in this case. Relative change in the standard deviation is about 13 %, if one compares the largest and smallest vaues

of α considered in this example.
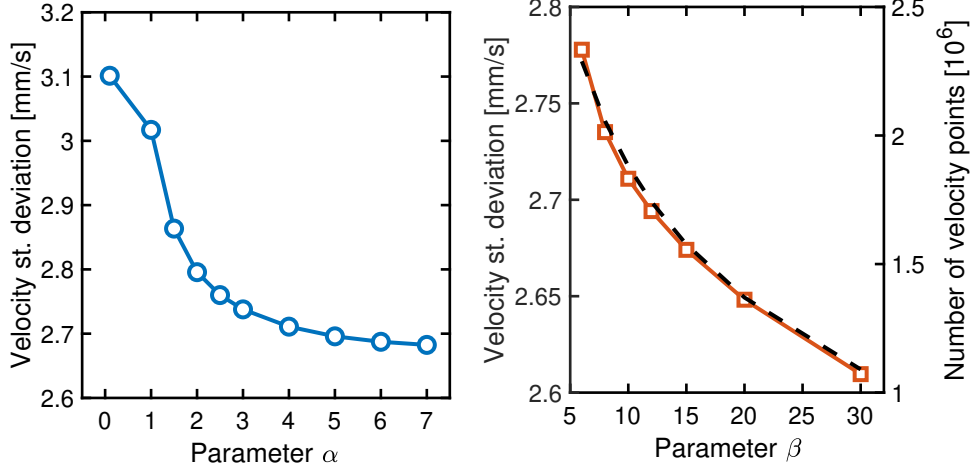
Figure 2.5: Effect of the Gaussian estimator parametrization on the standard deviation of the particle velocity. Employed data set is obtained in thermal counteflow (1.95 K, the normal fluid velocity 18.2 mm/s), see text for details. *Left panel:* standard deviation as the function of the kernel width α. $\beta = 10$ for all cases, each data set contains ca. 1.88 million velocity points. *Right panel:* Standard deviation as the function of the kernel support width β (red squares, left axis). Here, $\alpha = 4$. Black dashed line, right axis: number of the resulting velocity points.

Note that $\alpha = 0.1$ is an extraordinary choice, made solely for the sake of the following argument. Very narrow kernels are ineffective in the noise reduction, since for $\alpha \ll 1$ the convolution with G_0 becomes identity and convolution with G_1 becomes equivalent to Eq. (2.7). In practice, we set $\alpha \geq 1$, to ensure that Gaussian estimators operate as multi-point algorithms. For Fig. 2.5 it means that the standard deviation obtained with $\alpha = 0.1$ is equivalent to what one would have obtained by taking the central difference scheme.

Moreover, we can associate each differentiation method to its time resolution, quantified by the characteristic time scale τ_{p}. It is quite straightforward to find this time for central differences, where we set $\tau_{\mathrm{p}} = 2\tau$ because 2τ is the time difference between the particle positions employed to estimate the particle velocity, see Eq. (2.7).

Similarly, for Gaussian kernels, we can identify all raw positions along a trajectory that significantly influence the resulting position, velocity or acceleration estimate. Since G_0 decays exponentially for late times (Fig. 2.4), we can build up an analogy with the two-sigma rule for Gaussian peaks, which suggests that contributions representing 95 % of the area below G_0 fall into the interval $[-\sqrt{2}\alpha\tau, \sqrt{2}\alpha\tau]$. The characteristic time scale then becomes the width of this interval, which means that τ_{p} of Gaussian estimators can be defined as

$$\tau_{\mathrm{p}} = 2\sqrt{2}\alpha\tau. \tag{2.13}$$

We note in passing that this definition is valid only for $\alpha \geq 1$.

Now, we focus on the effects resulting from the choice of the kernel support width, β. Considering again the exponential decay of the kernels for late times, a finite value of β (we always set $\beta > \sqrt{2}\alpha$) is sufficient to obtain well-converged positions, velocities and accelerations. The convergence can be studied on a small set of trajectories, obtained by two kernels parametrized with (α, β) and $(\alpha, \beta + 1)$, respectively. The smallest necessary β can be then systematically selected, by accepting some minimum level of differences between the estimates, say, 5%.

However, a neat convergence of individual velocity points contrasts with the behaviour of the entire data set. This is illustrated in the right panel of Fig. 2.5, where we plot again the velocity standard deviation, computed from velocity estimates obtained with fixed $\alpha = 4$ and with different values of β. Although we see a similar decrease of the standard deviation as in the left panel of the same figure, here the effect is due to a selection bias, as the use of different support widths alters the size of the resulting data set.

It follows from Eq. (2.9) that the convolution is defined only on a trajectory having at least $2\beta + 1$ subsequent positions. These trajectories are trimmed after the convolution: from n raw positions one obtains $n - 2\beta$ smoothened positions (velocities, accelerations), while the tracks with less than $2\beta + 1$ points are entirely discarded. In other words, the use of too wide kernel supports systematically prefers longer trajectories over short ones.

Due to the bias, the dependence of the velocity standard deviation on β correlates with the size of the resulting data set, see the black dashed line in the right panel of Fig. 2.5. In thermal counterflow, this effect is likely linked to a less frequent occurrence of large velocity events on long trajectories, since these events may cause the particle to leave the illuminated plane. It hence becomes beneficial to choose the support width as small as possible, in order to ensure that the data are adequately converged, but to preserve as much of statistical information as possible.

2.2   Second sound attenuation

Second sound is one of the several propagative modes typical to quantum fluids. It represents temperature (or entropy) waves, which are interpreted within the two-fluid model as anti-phase oscillations of the normal and superfluid components [13]. Similar in-phase oscillations, representing ordinary sound waves, are called the first sound. In He II, the second sound can be transmitted by displacing one fluid component relative to the other one. This can be achieved thermally, by a periodical heat dissipation or mechanically, by oscillating a porous elastic membrane, permeable only to the superfluid component.

Presence of the quantized vortex tangle in He II couples the normal and superfluid components via the force of mutual friction, already introduced in §1.1. As this force tends to diminish differences between the velocity fields of the two components, the amplitude of a second sound wave that propagates through the

vortex tangle decreases. The corresponding attenuation coefficient is [75]

$$\xi_L = \frac{B\kappa}{4c_2} \cdot \frac{1}{\mathcal{V}} \int_{\mathcal{V}} \sin^2\left[\varphi(\ell)\right] \mathrm{d}\ell, \tag{2.14}$$

where B is the mutual friction coefficient, κ denotes the circulation quantum and c_2 is the second sound velocity (B and c_2 are temperature dependent, and their values are tabulated [18]). Term to the right from the multiplication sign denotes the vortex line density projected into the direction of the second sound propagation: we integrate along the vortex line elements $\mathrm{d}\ell$ present in the volume $\mathcal{V}$; $\varphi(\ell)$ denotes the angle between the given line element and the second sound wave vector. For an isotropic vortex tangle, usually taken as the first order estimate of the tangle geometry, all values of φ are equally likely and it holds that $\langle \sin^2(\varphi) \rangle = 2/3$ [13]. Therefore, for the isotropic tangle, the integral in Eq. (2.14) can be replaced by $2L\mathcal{V}/3$, where L is the vortex line density.

The most common attenuation method, employed also in the current work, is based on the second sound resonance, realized in semi-open resonant cavities. Resonant (standing) wave of second sound is generated and detected by a pair of transducers facing each other. Quantity that reflects the vortex line density present in the cavity is the resonance amplitude A, evaluated with respect to the amplitude A_0 obtained in quiescent helium. Under the assumption of tangle isotropy, an approximate relation for the vortex line density is [13]

$$L \simeq \frac{6\pi\Delta_0}{B\kappa} \left(\frac{A_0}{A} - 1 \right), \tag{2.15}$$

where Δ_0 denotes the half-width of the resonance peak measured in a quiescent fluid. Note that, in He II, this method is influenced by the presence of remnant vortices (and remnant VLD L_R), which limits the sensitivity of this method. Typically, $L_\mathrm{R} \approx 10^6\,\mathrm{m}^{-2}$ [13], which corresponds to the mean intervortex spacing of $1\,\mathrm{mm}$, see Eq. (1.6).

Membrane sensors

Design of our sensors is similar to that used in the previous experiments conducted in Prague [13, 28, 32]. The sensors rely on an oscillating porous membrane, which displaces the normal component of He II and is fully penetrable to the superfluid one. As the normal component is set into motion and the superfluid component remains still, the relative motion of two components is established, which eventually results in the propagation of the second sound waves.

A standing second sound wave is obtained by a pair of transducers, mounted on the opposite sides of a custom 3D-printed channel with the square cross section of $10\,\mathrm{mm}$ sides, see Fig. 2.6. The membrane (red) is coated from one side by a thin layer of gold and put in electrical contact with the brass sensor body. The membrane faces the open volume of the channel via a hole with $8\,\mathrm{mm}$ diameter. From the opposite side of the membrane a flat brass electrode presses against it (adequate force is applied by a loaded spring), forming a parallel-plate capacitor with the typical capacity of ca. $100\,\mathrm{pF}$ at low temperature.
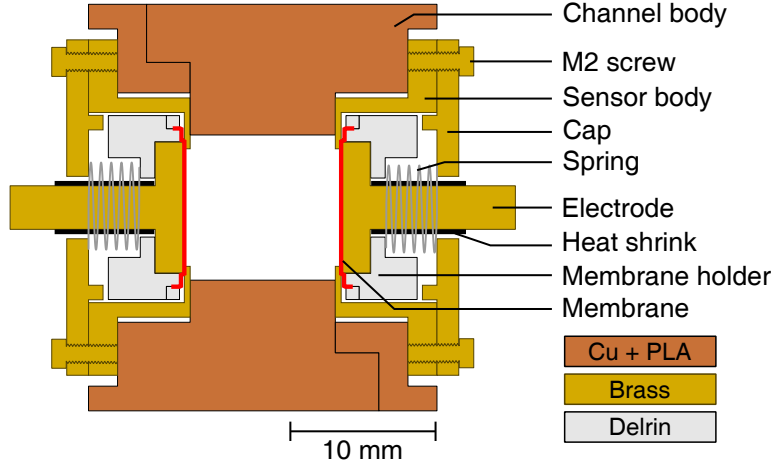
Figure 2.6: Scheme of the channel cross section with the second sound sensors assembled. Employed materials are colour-coded.

Both membranes are held at the bias voltage of $100\,\mathrm{V}$ relative to ground, in order to couple them to the near-ground electrodes. To transmit a second sound wave we supply one of the electrodes with a sine wave signal of the given frequency and amplitude. The latter is typically $7\,\mathrm{V}$ RMS, too low to generate additional turbulence in the channel.[6] Transmitted signal is detected by the second electrode, read by a SR-830 lock-in amplifier, providing in-phase (A_x) and quadrature (A_y) components of the received signal.

Typical frequency sweep across the resonance frequency is shown in the left panel of Fig. 2.7. Acquired data (colour points) resemble a Lorentzian peak, which is phase-shifted by $\pi/2$ for the quadrature component. Indeed, direct fitting of either signal component (grey lines) allows to estimate the resonance frequency, peak amplitude and peak half-width. Alternatively, we can use both signal components to fit the data with a circle [77] in (A_x, A_y) space, as shown in the right panel of Fig. 2.7. In this case, we can only determine the peak amplitude, equal to the circle diameter.

Note that it is possible to utilize multiple harmonic modes in the channel. Their respective resonance frequencies are equidistant, with the increment equal to the fundamental mode frequency, f_0. Since the fundamental mode spans half of its wavelength across the channel, we can estimate the effective width of the resonant cavity as $w = c_2/2f_0$. From the first 10 harmonic modes acquired at $1.65\,\mathrm{K}$ we can estimate for the present set up $w = (10.3 \pm 0.3)\,\mathrm{mm}$, which is slightly larger than the channel width ($10\,\mathrm{mm}$).

Time constant of the lock-in amplifier is set to at least $100\,\mathrm{ms}$ when performing frequency sweeps. This value limits the sampling rate of the signal, which means that the acquisition of resonance curves similar to that in Fig. 2.7 is rather a

---

[6]We observe that the second sound amplitude grows linearly with the amplitude of the input signal. If turbulence were generated by the second sound wave, we would observe that the sound amplitude plateaus with the driving voltage, see Ref. [76] for a recent example of this phenomenon.
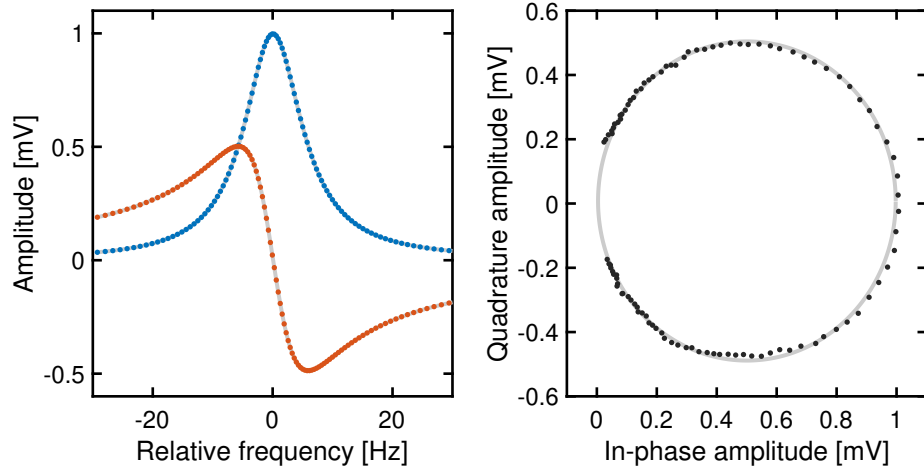
Figure 2.7: Example of the acquired second sound resonance. *Left panel:* frequency sweep across the 4th harmonic mode, measured at $1.65\,\text{K}$. Resonance frequency of $3609\,\text{Hz}$ is subtracted from the data. Points: measured in-phase (blue) and quadrature (red) components. Grey lines: phase-resolved Lorentzian fits. *Right panel:* same data (black points) plotted in (A_x, A_y) space. Grey line: circle fit.

lengthy process. However, only the signal measured at the resonance frequency is necessary to estimate the vortex line density from Eq. (2.15). Hence, for a time-resolved acquisition, we set the lock-in time constant to $30\,\text{ms}$ and we continuously adjust the frequency of the input signal by a software PID loop to ensure that the resonance condition is fulfilled at all times. We then acquire the corresponding amplitude $A(t)$ from the in-phase channel of the lock-in, with the average sampling rate of ca. $15\,\text{Hz}$.

Miniature sensors

Finite size of the resonant cavity imposes a limit on the spatial resolution of the second sound attenuation technique. In the former case of the membrane sensors, the effective cavity volume can be estimated as the volume of a cylinder with $8\,\text{mm}$ diameter, equal to the diameter of the membrane exposed to the channel, and height $w = 10.3\,\text{mm}$. We obtain $\mathcal{V} \approx 520\,\text{mm}^3$. In relation to Eq. (2.14), we can identify this value with the volume of the region where quantized vortices contribute to the second sound attenuation.

Downscaling of the sensors is necessary to improve the spatial resolution of the technique, which is especially useful when the investigated vortex tangle is inhomogeneous. Suitable miniature sensors are developed by the group of P.-E. Roche in Grenoble, and their performance was already demonstrated in a number of experimental works [75, 78]. We employ one of these sensors to probe the vortex tangles above counterflow jets, summarized in §4.

Miniature sensor, depicted in Fig. 2.8, resembles a pair of small tweezers. It consists of two thin arms cut from a silicon wafer, ca. $20\,\text{mm}$ long and $1\,\text{mm}$ thick, placed $w = (2.505 \pm 0.002)$ mm apart. Small resistive heater is fabricated

at the end of one arm, facing a similarly-sized thermometer. Sensitive areas of both components are smaller than $1\,\text{mm}^2$, which means that the cavity volume is less than $\mathcal{V} = 2.5\,\text{mm}^3$, i.e., at least 200-times less than the volume probed by the membrane sensors.
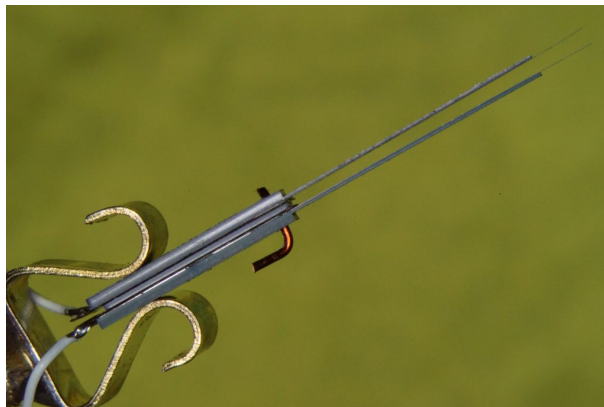
Figure 2.8: Photography of the second sound tweezers similar to those used in the present work. Sensitive area of the sensor, i.e., the heater–thermometer pair, is located in the top right corner of the image. Author: Philippe-E. Roche/CNRS, licensed under CC BY-NC-ND 4.0.

AC signal sent to the heater leads to a periodic heat dissipation at double frequency and a temperature wave (i.e., second sound) is transmitted towards the thermometer, which detects second sound waves in the form of periodical changes of its resistance. Since we polarize the thermometer by a small constant current (ca. $30\,\mu\text{A}$), we detect voltage oscillations, read by a NF Corporation LI5640 lock-in amplifier.

The acquired signal is analogous to that displayed in Fig. 2.7. We access its in-phase and quadrature components, which again display Lorentzian resonance peaks. A wide frequency sweep, obtained in quiescent He II at $1.65\,\text{K}$, is displayed in Fig. 2.9 as an example. VLD measurements presented in §4 as based on the amplitude of the peak highlighted by the green colour. Note that equidistant positions of individual resonance peaks are neatly apparent from this figure (the corresponding frequency increment between the peaks was used to estimate the cavity size w).
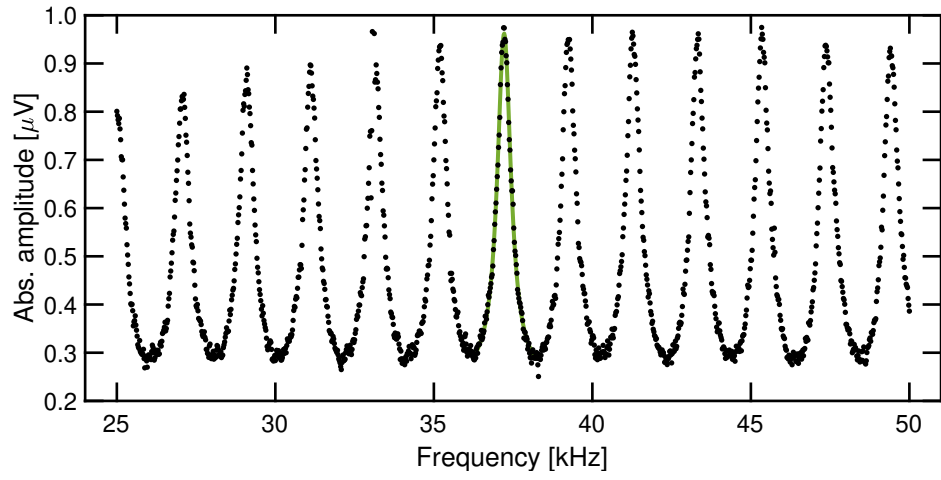
Figure 2.9: Amplitude of the second sound, $\sqrt{A_x^2 + A_y^2}$, detected by miniature tweezers at $1.65\,\mathrm{K}$ in quiescent He II. Green line: resonance peak employed for VLD measurements summarized in §4.

3 Particle-vortex interactions in channel counterflow

Steady thermal counterflow in a semi-closed channel is investigated by flow visualization. We specifically study the motions of small solid particles with the aim to clarify how the particles interact with the quantized vortex tangle [29, 67], to understand the underlying vortex tangle dynamics. This chapter mainly follows the line of scientific enquiry published in Refs. [61, 79–81]. After a short introduction to the key aspects of channel counterflow provided in §3.1, we first study in §3.2 the roles of solid boundaries in the development of quantum turbulence in thermal counterflow. Non-classical energy transfer mechanisms are investigated in §3.3 and finally, in §3.4, we report on a peculiar bimodal regime of the particle motion that occurs exclusively in turbulent counterflow.

3.1 Introduction

The two-fluid model of He II, introduced already in §1.1, postulates two weakly interacting velocity fields attributed to the normal and superfluid components and denoted $\boldsymbol{v}_\mathrm{n}$ and $\boldsymbol{v}_\mathrm{s}$, respectively. In thermal counterflow the components flow, on average, in opposite directions and the characteristic velocity of the flow becomes the counterflow velocity $v_\mathrm{ns} = |\boldsymbol{v}_\mathrm{n} - \boldsymbol{v}_\mathrm{s}|$. The corresponding Reynolds number of thermal counterflow can be then defined as [31]

$$\mathrm{Re} = \frac{\rho v_\mathrm{ns} D}{\mu_\mathrm{n}}, \tag{3.1}$$

where ρ denotes the He II density, D is the channel hydraulic diameter and μ_n indicates the dynamic viscosity of the normal component. Following Ref. [31], thermal counterflow becomes turbulent above $\mathrm{Re} \approx 2300$ in the channel employed for experimental works presented below and depicted in Fig. 3.1. Here, we focus on fully developed turbulence, whose main ingedient is the tangle of quantized vortex lines. The corresponding vortex line density L scales with the square of v_ns, according to Eq. (1.7).

Particle-vortex interactions, whose main physical mechanisms are outlined in §2.1, typically lead towards the existence of events of large particle velocity. Statistical fingerprint of such processes is observed in the form of heavy-tailed velocity distributions [25], clearly identified in both thermally and mechanically driven quantum turbulence [69]. It is the distribution shape that distinguishes quantum
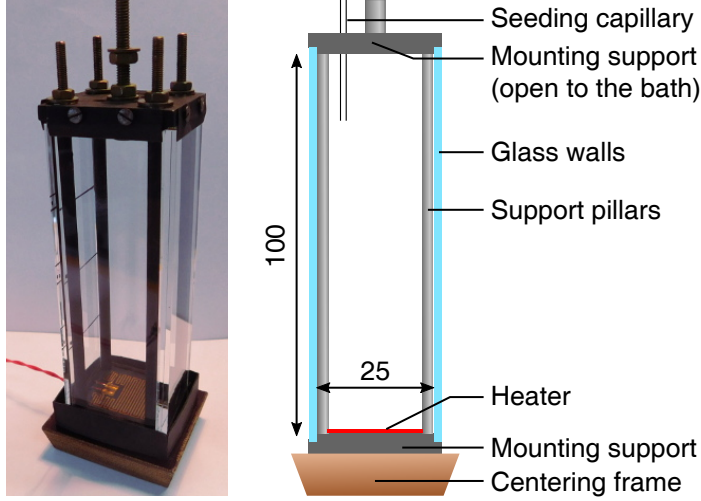
Figure 3.1: Photography (left) and scheme (right) of the counterflow channel employed for the experiments summarized in this chapter. Mounting supports and pillars are made of brass and coated with black paint. Centering frame is made of an epoxy composite. Dimensions are given in millimeters.

turbulence from classical one [74, 82], since in classical turbulence the expected particle velocity distribution is almost Gaussian [83].

However, non-classical tails are not always present and nearly Gaussian velocity distributions arise also in quantum turbulence [22]. In order to understand these phenomena, we need to define two fundamental length scales. The probed scale, s_p indicates what is the experimental resolution, i.e., the smallest length associated with the particles employed for visualization. Since the particle positions are sampled with a finite frequency, s_p can be defined as

$$s_\mathrm{p} = u_\mathrm{abs}\tau_\mathrm{p}, \tag{3.2}$$

where u_abs represents the mean particle velocity and τ_p denotes the time scale at which the velocity is calculated.[7] When the velocity is estimated by the central difference method, Eq. (2.7), τ_p is equal to the time difference between considered particle positions. For Gaussian estimators, τ_p is equal to the characteristic time scale of the employed kernel, defined by Eq. (2.13).

The second length scale is called the quantum scale, s_q and it is equal to the mean intervortex distance ℓ, Eq. (1.6):

$$s_\mathrm{q} = \ell = \frac{1}{\sqrt{L}} \approx \frac{1}{\gamma v_\mathrm{ns}}. \tag{3.3}$$

Note that the right-hand side is obtained by using Eq. (1.7) and neglecting the small offset v_c. Now, these length scales can be combined into a non-dimensional ratio

$$R = \frac{s_\mathrm{p}}{s_\mathrm{q}} = \frac{u_\mathrm{abs}\tau_\mathrm{p}}{1/\sqrt{L}} = \gamma v_\mathrm{ns} u_\mathrm{abs}\tau_\mathrm{p}. \tag{3.4}$$
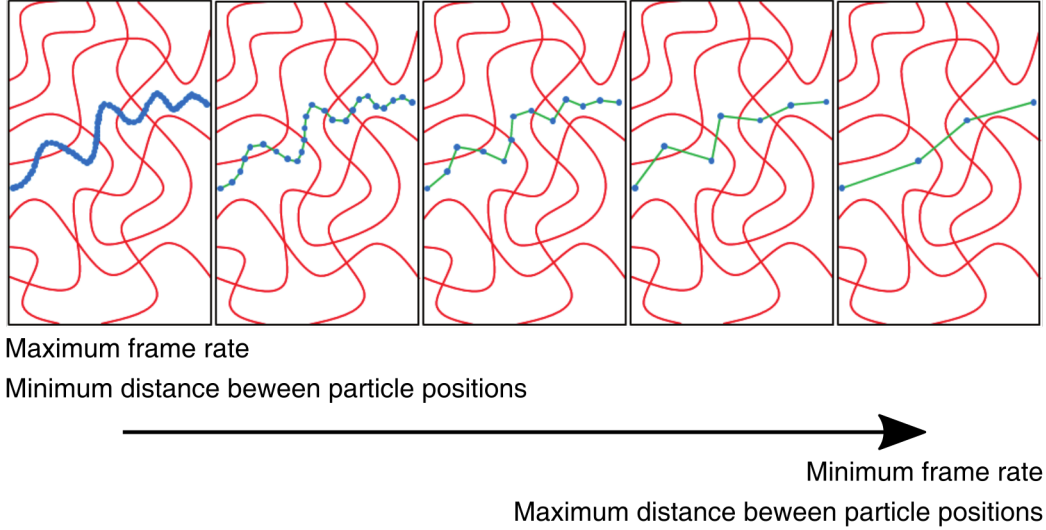
---

[7]Another factor that limits the experimental resolution is the particle size. In most experiments though, the particle size is smaller than s_p defined by Eq. (3.2).

The ratio can be understood also in terms of time scales. In particular, if we define τ_p as the characteristic time scale of the experiment, we can compare it to the time needed by the particle to travel between two quantized vortices. This time, τ_q, can be defined with the intervortex distance and the mean particle velocity as $\tau_q = \ell / u_{abs}$. It can be then shown that the time ratio τ_p / τ_q is algebraically equivalent to R defined by Eq. (3.4).

Strong correlation between R and the occurrence of heavy tails in the velocity distributions is reported in Ref. [74]. The tails are visible for $R < 1$, when the particles probe scales smaller than the intervortex distance. As the scale ratio increases, the tails become less apparent and, as $R \approx 1$, the tails disappear completely [31, 74], the corresponding velocity distribution becomes Gaussian-like and the particles behave as they were probing flows of a classical fluid.

It is now useful to mention that a single visualization data set allows to probe a broad range of scales. The approach, introduced in Ref. [74], consists of removing camera frames from the acquired data sets, see Fig. 3.2. The outlined procedure effectively decreases the camera frame rate, i.e., increases τ_p and by consequence increases also s_p and R. Therefore, a single data set can be employed to investigate a range of scales, which is typically limited by the actual frame rate of the camera and the data set size.

Maximum frame rate
Minimum distance beween particle positions

Minimum frame rate
Maximum distance beween particle positions

Figure 3.2: Illustration of probing large length scales. Particle positions (blue points) are acquired at the maximum frame rate (left panel). By removing camera frames, the particles gradually probe larger length scales (panels from left to right). Red lines indicate the vortex lines (their motion is neglected for clarity). Adapted from [74].

The parameter that quantifies whether the distribution is heavy-tailed or not is its flatness, i.e., the fourth central moment normalized by the standard deviation. When $R < 1$ and the distribution displays non-classical tails, its flatness is significantly larger then 3, which is exactly the value corresponding to the Gaussian distribution. As we begin to increase the probed scale, the flatness decreases until it reaches the value of 3 at $R \approx 1$, and remains near this value for $R > 1$. The

behaviour at large length scales is experimentally tested for R up to ca. 70 for grid turbulence in He II [22].

3.2   Role of flow boundaries

Extensive studies of wall-bounded turbulence in classical fluids indicate that solid boundaries have a significant role in the development of turbulent flows [84]. Similar effects have been observed in quantum turbulence. For example, numerical simulations of turbulent counterflow [85, 86] reveal that quantized vortices preferentially concentrate near the channel walls. Other experimental [27, 87] and numerical [88] investigations point towards the existence of superfluid boundary layers that are characterized by dense vortex tangles.

Consistent observations of wall-bounded thermal counterflow were carried out in Prague. La Mantia [89] visualized counterflow in the vicinity of a solid wall parallel to the heat flux direction. He found that the vortex tangle is indeed inhomogeneous across the channel cross section, which implies that the channel geometry has a significant impact on the development and the resulting steady state of quantum turbulence [31].

In the present work we investigate flows in the proximity of another boundary, which is the closed channel end equipped with the heater. Since the heater represents an equally rough boundary as the channel wall, some modulation of the vortex line density should be expected along the channel height [90]. This concept represents the quantum analogue of the entry length, which is defined for channel flows of classical fluids as the length needed for turbulence to develop. The latter depends mainly on the channel geometry and is of the order of 25 diameters for pipe flows [87]. Recent numerical results suggest that this length is substantially larger in thermal counterflow [91].

Series of visualization experiments were performed in the counterflow channel of 25 mm square cross section, sketched in Fig. 3.1. Motions of solid deuterium and deuterium hydride particles were studied in the 13 mm wide and 8 mm high field of view, located ca. 1 mm above the channel heater and centred between the vertical walls of the channel. We compare the obtained data with reference data sets, obtained in the same channel, but in the bulk, i.e., as far away as possible from the channel boundaries. In this case, we use solid hydrogen and deuterium particles. Experimental conditions of individual data sets are summarized in Tab. 3.1.

The smallest probed time scale, linked to the employed camera frame rate, ranges from 2 ms to 2.5 ms. Considering that the mean velocity of the particles, calculated here by the central difference method, is comparable to v_{ns} [31], we can say that the smallest probed scale is of the order of $2\,\mathrm{ms} \cdot 5\,\mathrm{mm/s} = 10\,\mathrm{\mu m}$, which is at least one order of magnitude smaller than the corresponding quantum scale (Tab. 3.1).

To fully appreciate the scale dependence of particle-vortex interactions, we inves-

Table 3.1: Experimental conditions of individual data sets. Displayed symbols are used in Figs. 3.3 – 3.5. BH, BD: data sets measured in the bulk; D1–D4: near-heater data sets, D_2 particles; HD1–HD4a: near-heater data sets, HD particles. T: thermodynamic temperature; q: applied heat flux; v_{ns}: counterflow velocity; Re: Reynolds number, Eq. (3.1) for $D = 25\,\mathrm{mm}$; s_q: quantum scale, Eq. (3.3); c: correction factor, Eq. (3.5), see text for details.

		T [K]	q [W/m^2]	v_{ns} [mm/s]	Re $/10^3$	s_q [μm]	c
■	BH	1.77	612	6.8	19.0	70	1
◻	BD	1.77	608	6.7	18.8	70	0.5
○	D1	1.24	23	2.2	4.0	674	20
○	D2	1.40	54	2.2	5.2	409	10
○	D3	1.75	235	2.7	7.6	177	10
○	D4	1.95	234	1.9	5.1	183	6
△	HD1	1.24	20	1.9	3.5	770	40
▽	HD2a	1.40	25	1.0	2.5	868	40
△	HD2b	1.40	48	2.0	4.7	455	20
◇	HD2c	1.40	65	2.6	6.3	338	10
▽	HD4a	1.95	200	1.7	4.3	214	10

tigate the particle motions in a broad range of length scales, as outlined above, keeping at least 10^5 points in individual data sets. As a result, our data are fit to probe both quantum and classical features of thermal counterflow. We focus on the horizontal velocity component, as the vertical one is influenced by the mean flow.

We start by plotting the scale-resolved velocity flatness of bulk data (BH, BD) and near-heater data (D1 to D4) in the left panel of Fig. 3.3. Data sets BH and BD neatly follow the expected physical description outlined above, i.e., the corresponding flatnesses are larger than 3 for $R < 1$ and reach the Gaussian value at $R \approx 1$. However, a different picture is offered by the near-heater data. Although the scale-resolved flatness decreases towards 3, the convergence towards Gaussianity occurs at a smaller length scale than expected.

If we consider that the near-Gaussian shape of the velocity distributions should occur only for $R > 1$, we come to the conclusion that, in the heater proximity, the estimation of the quantum length scale provided by Eq. (3.3) is incorrect. We can hence introduce the effective length scale ratio

$$R_{\mathrm{eff}} = cR, \tag{3.5}$$

where the correction factor c accounts for this discrepancy. Experimentally obtained values of c are summarized in Tab. 3.1 and the flatness, now plotted as the function of R_{eff}, is displayed in the right panel of Fig. 3.3.

Two observations can be made at this point. First, we note that $c = 0.5$ for the data set BD, while $c = 1$ for BH. This indicates that the particle inertia cannot be neglected, as solid deuterium particles seem to effectively experience a less

dense tangle than hydrogen ones. The effect of particle inertia is discussed in more detail below. Second, we find that c ranges between 6 and 20 for data sets D1–D4. In other words, there is evidence that the actual intervortex distance in the heater proximity is c-times smaller than in the bulk, at the same temperature and applied heat flux. The corresponding increase of the vortex line density (see Eq. 1.6) near the hater is remarkable, especially when we take into account that deuterium particles likely underestimate its actual value.

Moreover, it seems that the correction factor is temperature dependent. For a roughly constant counterflow velocity we observe that c decreases with temperature, from 20 at $1.24\,\mathrm{K}$ (data set D1) to ca. 6 at $1.95\,\mathrm{K}$ (D4). We believe this dependence is related to the temperature dependence of γ [29], which instead increases with temperature. As a result, for a constant R_{eff}, the increase of γ is compensated by the decrease of c.
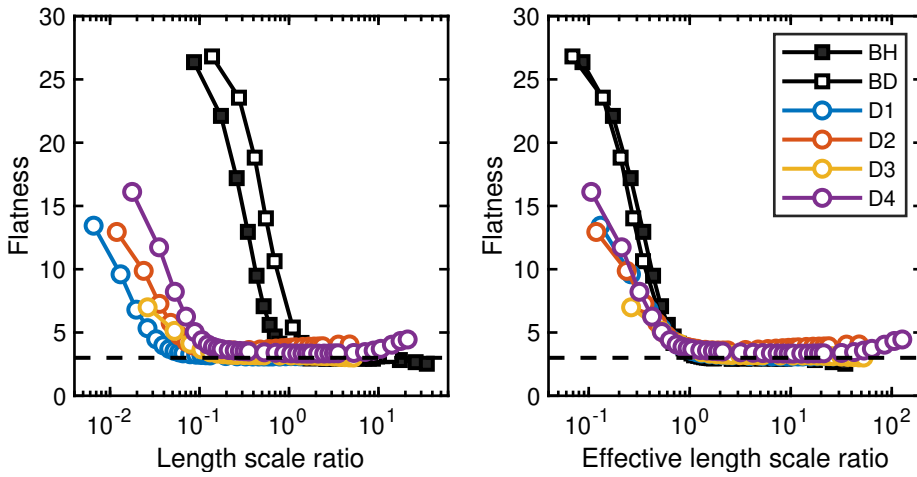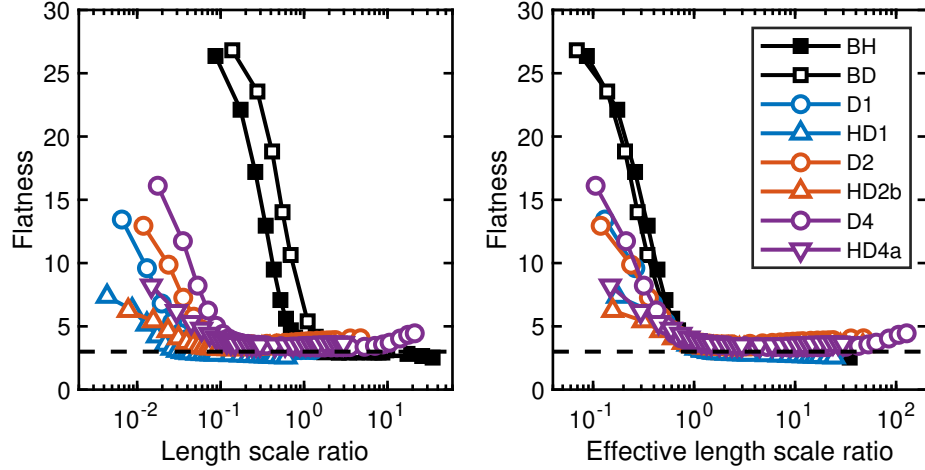

Figure 3.3: Scale-dependent velocity flatness for D_2 particles. *Left panel:* flatness as the function of R. *Right panel:* flatness as the function of R_{eff}. Note the log-linear scale.

Effect of particle inertia mentioned above can be investigated by employing particles made of different materials. Left panel of Fig. 3.4 shows again the velocity flatness as the function of R. Now we plot pairs of data sets (highlighted by the same colour) obtained in similar conditions, i.e., similar temperature and heat flux, but with different particle materials: solid hydrogen (H_2), deuterium (D_2) and deuterium hydride (HD). Their density is equal to ca. $88\,\mathrm{kg/m^3}$ for H_2, $145\,\mathrm{kg/m^3}$ for HD and $200\,\mathrm{kg/m^3}$ for D_2 [57]. Following Ref. [25], we can express the acceleration of a particle p in a fluid f as

$$\frac{\mathrm{d}\boldsymbol{u}_p}{\mathrm{d}t} = \frac{1+C}{\rho_p/\rho_f + C}\frac{\mathrm{D}\boldsymbol{u}_f}{\mathrm{D}t}, \qquad (3.6)$$

where C is the added mass coefficient, ρ_p and ρ_f denote the particle and fluid densities and $\mathrm{D}\boldsymbol{u}_f/\mathrm{D}t$ represents the substantial derivative of the fluid velocity. For spherical particles ($C = 1/2$) accelerating in He II ($\rho_f \approx 145\,\mathrm{kg/m^3}$ [18]) we obtain that HD particles accelerate 1.25-times more and hydrogen particles accelerate 1.70-times more than deuterium ones.

Analogous trends are apparent in the correction factor values (Tab. 3.1). Of course, the effect of the heater proximity is the most prominent, which means that $c > 1$ for D and HD data sets. However, by comparing data sets D1, D2, D4 with HD1, HD2b and HD4a we find that c values for HD particles are about 2-times larger than the corresponding values for D_2 particles, which means that less-accelerating deuterium particles effectively experience less dense vortex tangles. This is also consistent with the results obtained from data sets BD and BH, where the ratio of correction factors is even closer to that of particle accelerations.
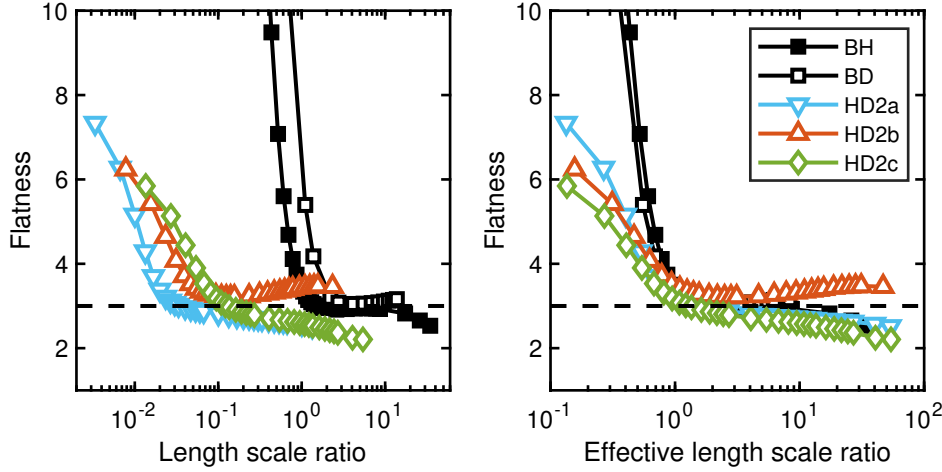

Figure 3.4: Scale-dependent velocity flatness for D_2 and HD particles. Same colours highlight data sets obtained in similar experimental conditions. *Left panel:* flatness as the function of R. *Right panel:* flatness as the function of R_{eff}. Note the log-linear scale.

Finally, we now focus on the effect of the heat flux. In Fig. 3.5 we compare scale-resolved flatnesses for data sets HD2a–HD2c, which differ only by the applied heat flux. From the obtained correction factors, which systematically decrease as v_{ns} increases, we conclude that, as v_{ns} increases, the particles experience gradually less dense vortex tangles. As it is reported in Ref. [92], the ratio between the viscous drag force from the normal component and the pressure gradient force from the superfluid component increases as the heat flux increases. In consequence, the particles are less likely to become trapped in the vortex tangle at higher v_{ns}, which explains the observed dependence.

In conclusion, there is a clear experimental evidence suggesting that the tangle of quantized vortices is significantly denser in the heater proximity than in the bulk. Enhancement of the vorticity generation near this boundary can be estimated, at lest qualitatively, by the scale-resolved measures of the velocity distribution flatness, keeping in mind the underlying effects of the particle inertia and the applied heat flux, which can slightly modulate experimental observations.

We can partly explain this outcome by considering the presence of vortex pinning centres that are present on any solid surface submerged in He II [88], combined with the presence of a solid boundary. While the pinning centres are relevant for the superfluid component, the boundary likely affects the flow of the normal component. Following Ref. [93], we can say that the normal component is slower

Figure 3.5: Scale-dependent velocity flatness for HD particles, obtained at different heat fluxes. *Left panel:* flatness as the function of R. *Right panel:* flatness as the function of R_{eff}. Note the log-linear scale.

in the proximity of channel walls than in the bulk, as it is constrained by the no-slip boundary condition valid for viscous fluids. If we assume at the same time that heat is homogeneously transported across the channel,[8] we find that quantized vortices tend to concentrate in regions defined by a relatively small local fluid velocity, i.e., in the proximity of channel walls.

3.3 Flight-crash events

Turbulent energy is usually supplied at larger length scales than those at which it is dissipated by the action of viscosity. Consequently, in a steady three-dimensional turbulence a one-directional flux of energy between scales is established, famously breaking the time reversal symmetry. Neat signature of this time irreversibility is the occurrence of flight-crash events, which were first identified in classical turbulence [95, 96]. It was observed that the particles, suspended in a turbulent flow, tend to loose their energy more quickly than they gain it, at all scales.

Here we study this phenomenon in quantum turbulence, where the energy dissipation processes substantially differ from classical ones, thanks to the presence of the quantized vortex tangle. Numerical simulations performed in the zero temperature limit found that the energy contained in the tangle dissipates via the phonon emission, vortex reconnections and exciatation of the Kelvin waves [97]. At temperatures above $1\,\text{K}$, these processes are combined with the viscous dissipation in the normal component.

We investigate two kinds of turbulent flows. We consider a steady counterflow,

---

[8]Inhomogeneous distribution of heat across the channel leads to the occurrence of temperature gradients. Recent experimental measurements [94] report that these gradients can be observed in thermal counterflow solely for heat fluxes of the order of $1\,\text{kW/m}^2$, which are significantly larger than those considered in the present work.

Table 3.2: Experimental conditions of the considered data sets. CF1–CF3: thermal counterflow; OG1–OG3: oscillating grids. T: thermodynamic temperature; q: applied heat flux; u_{abs}: mean particle velocity; s_{q}: quantum scale, estimated from Eq. (1.7) for data sets CF1–CF3; for sets OG1–OG3, see Ref. [22].

	T [K]	q [W/m^2]	u_{abs} [mm/s]	s_{q} [μm]
CF1	1.50	193	3.1	35
CF2	1.50	349	4.6	31
CF3	1.76	616	3.0	27
OG1	1.95	–	22.4	5
OG2	1.75	–	20.0	5
OG3	1.50	–	20.9	5

visualized in our square channel (Fig. 3.1) in a 13 mm wide and 8 mm high field of view located sufficiently away from the channel walls. We employ solid HD particles for this task. The second flow type considered is turbulence generated by a pair of grids oscillating in phase with 3 Hz frequency and 10 mm amplitude. The flow is probed by solid deuterium particles in the same field of view, located between the grids, see Ref. [22] for more details. Keep in mind that thermally and mechanically generated flows of He II are fundamentally different [27]. In counterflow, two macroscopic velocity fields are observed, while in mechanically driven flows the normal and superfluid components share a single velocity field on scales substantially larger than the mean intervortex distance.

Six large data sets were acquired and their experimental conditions are summarized in Tab. 3.2. The counterflow sets are denoted as CF1–CF3, while the oscillating grid data are labelled OG1–OG3. Note that the latter cases are characterized by relatively dense tangles and large particle velocities, which implies that only length scales larger than the mean intervortex distance are probed, see Ref. [22] for the estimation of the quantum scale.

The signature of time irreversibility in the Lagrangian framework is studied by calculating longitudinal velocity increments, introduced in Ref. [98]. Increment $\mathrm{d}u(\tau)$ is computed as the projection of the velocity difference onto the direction of the corresponding position difference, see Fig. 3.6; τ now represents the time lag between the velocities and positions considered. Flight-crash events are neatly imprinted in this scalar quantity, since its statistical distribution becomes negatively skewed when the particles experience such events. We can therefore introduce two characteristic parameters, dimensional skewness $\mathrm{Sk_d}$, defined as the third central moment of $\mathrm{d}u(\tau)$, and non-dimensional skewness Sk, defined as

$$\mathrm{Sk} = \frac{\mathrm{Sk_d}}{\mathrm{d}u_\sigma(\tau)^3} = \frac{\left\langle [\mathrm{d}u(\tau) - \mathrm{d}u_m(\tau)]^3 \right\rangle}{\mathrm{d}u_\sigma(\tau)^3}, \tag{3.7}$$

where $\mathrm{d}u_m(\tau)$ is the mean increment and $\mathrm{d}u_\sigma(\tau)$ indicates its standard deviation.

For each data set we calculate $\mathrm{d}u(\tau)$ for a range of time lags τ such that the resulting statistical set of longitudinal increments has at least 10^5 samples. The
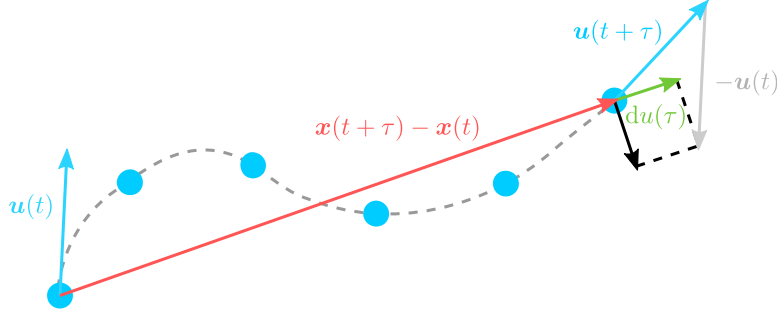
Figure 3.6: Longitudinal velocity increment (green) is obtained by projecting the velocity difference into the direction of the corresponding position difference (red). Adapted from [98].

length scale, at which the flow is probed, can be then defined as $s_{\mathrm{p}} = u_{\mathrm{abs}}\tau$, where u_{abs} is the mean particle velocity and the non-dimensional length scale ratio $R = s_{\mathrm{p}}/s_{\mathrm{q}}$ is then taken as the control parameter.[9]

The skewness of $\mathrm{d}u(\tau)$ is plotted as the function of R in Fig. 3.7, for CF (lines) and OG data (points). Black dashed line denotes an analogous dependence obtained from the numerical simulation of classical turbulence at a Taylor-based Reynolds number $R_\lambda = 280$ [98]. Striking difference between the classical and quantum turbulence is evident, especially for $R < 1$, i.e., at scales smaller than the quantum scale. For large enough scales, the overlap with the classical data is somehow better. Especially, we can note that OG data display a qualitatively similar behaviour, i.e., the obtained values of Sk are negative and increase with the probed scale.

Partial similarity of the classical turbulence and the grid turbulence in He II is studied in the left panel of Fig. 3.8, where the absolute values of dimensional skewness $\mathrm{Sk_d}$ are plotted as the function of R. We find that experimental data from OG data sets follow $|\mathrm{Sk_d}| \sim R$ at large length scales, which is consistent with the classical result reported in [98]. On the other hand, $|\mathrm{Sk_d}|$ values obtained for CF data are a few orders of magnitude smaller than their classical counterparts. Additionally, these values do not seem to appreciably depend on the probed scale, but instead they remain close to zero in the full range of investigated scales. This behaviour significantly differs from what is observed for OG data, which is particularly apparent from the right panel of Fig. 3.8.

In order to understand the experimental outcomes one must first take into account that the small-scale particle dynamics is influenced mainly by the interactions that take place between a particle and individual quantized vortices [69]. However, this concept is puzzling on the first look, especially if we consider recent numerical investigations of the quantized vortex reconnections [99, 100], which show that they are, in fact, time irreversible, since the reconnecting vortices were found to approach more slowly than they separate. On the other hand, these processes

---

[9]This definition is equivalent to the time ratio t_R introduced in our original publication [80]. Employed time scales were defined for the sake of consistency with Ref. [98]. Here, we prefer to be consistent with §3.2 of the present work.
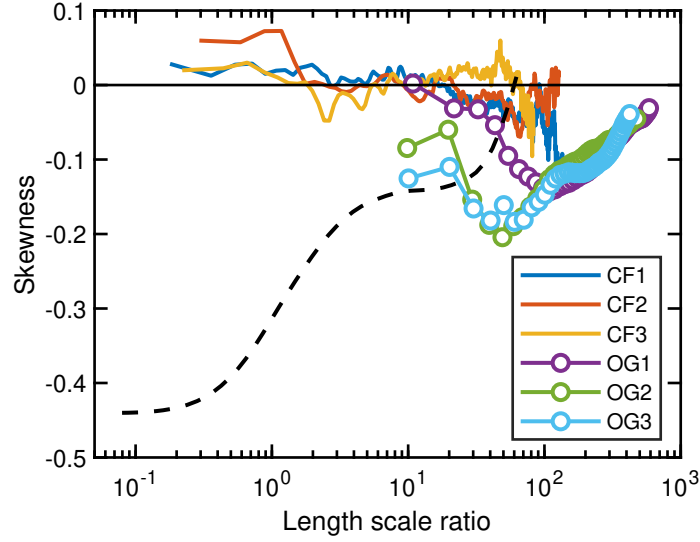
Figure 3.7: Skewness of the longitudinal velocity increment distributions as the function of the length scale ratio R. Colour lines and points: experimental data. Black dashed line: classical data from Ref. [98], see the main text for details. Note the log-linear scale.
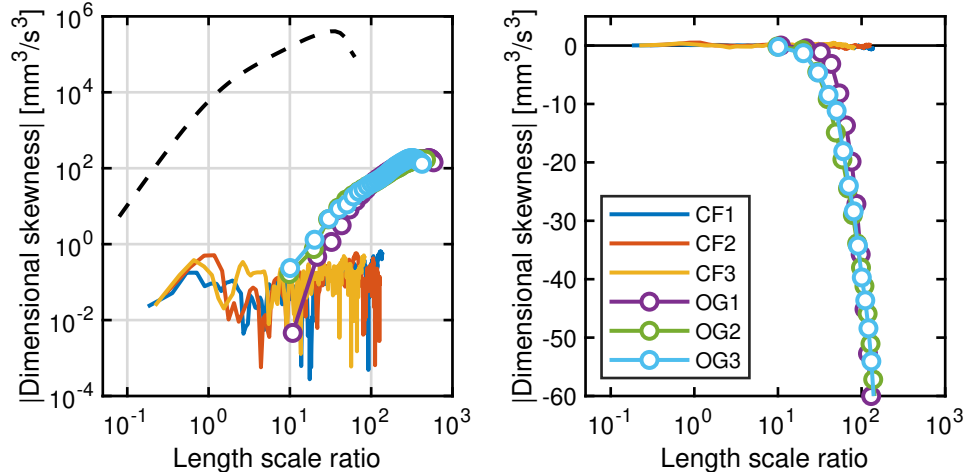
Figure 3.8: Dependence of the dimensional skewness. *Left panel:* log-log plot of its absolute value as function of the length scale ratio R. *Right panel:* dimensional skewness plotted in the log-linear scale with emphasis on counterflow data sets.

take place only in a limited range of length scales, which are larger than the size of the vortex core (approximately $1\,\text{Å}$ for He II), but smaller than the typical particle size (ca. $1\,\mu\text{m}$). In other words, the time reversal symmetry breaking processes within the vortex tangle cannot be probed by micron-sized particles, which explains why the lack of the flight-crash events is observed at small scales. This argument is supported by the direct visualization of vortex reconnections via similarly sized solid hydrogen particles [101], which were found to be time reversible.

If the probed scale falls behind the quantum scale, the particles experience a collective behaviour of the vortex tangle alongside with viscous effects taking place in the normal fluid, which have been found to behave quasi-classicaly [69].

This is consistent with the presence of negatively skewed distributions of $\mathrm{d}u(\tau)$ for grid turbulence in He II. The lack of similar effects in thermal counterflow is, however, not clear and requires further attention. At this point we can only speculate that the difference might be related to the fact that, in steady thermal counterflow, quantized vortices are polarized in planes perpendicular to the heat flux direction [7], while in the mechanically generated grid turbulence the vortex tangle is expected to be essentially isotropic.

3.4   Bimodal particle dynamics

Where do particles go in channel counterflow? Answering this simple question is in fact quite challenging, considering that both components of He II interact with the particles and influence their motion. In consequence, several motion regimes are distinguished by date, depending on the channel geometry, the bath temperature and the applied heat flux. Generally speaking, at relatively small heat fluxes, we find particles moving in the direction of the normal component (i.e., moving up in the standard experimental setting) as well as in the direction of the superfluid [31, 102]. As the heat flux increases, the number of particles moving up increases as well and, for relatively large heat fluxes, the particles only move in the normal fluid direction and their trajectories gradually become less straight [31].

The mean velocity of the particles moving in the normal fluid direction is reported to be either close to the normal fluid velocity v_n [102,103], or close to $v_\mathrm{n}/2$ [53,103]. The latter is usually observed in a relatively fast counterflow, i.e., for relatively large heat fluxes and dense vortex tangles, see Eq. (1.7). Decrease in the particle velocity from v_n to $v_\mathrm{n}/2$ is likely associated with frequent interactions between the particles and quantized vortices [104].

Observation of all the above regimes within a single set up is reported in Ref. [105]. The authors specifically measured the PDFs of the particle vertical velocity and they identified three qualitatively distinct regimes: (i) bimodal distributions with the maximums located near v_s and v_n for the smallest heat fluxes, (ii) bimodal distributions with the maximums near $v_\mathrm{n}/2$ and v_n for intermediate heat fluxes and (iii) unimodal distributions with a single peak near $v_\mathrm{n}/2$ for the largest heat fluxes.

Here we focus on the second case, which was investigated in our $25\,\mathrm{mm}$ square channel (Fig. 3.1) for the counterflow velocities exceeding $10\,\mathrm{mm/s}$. Three large data sets, labelled B1–B3, with more than one million samples each are analyzed, see Tab. 3.3 for details. Particle velocities are obtained by the Gaussian convolution with the corresponding time scale equal to ca. 5τ, where τ is the sampling time (the camera frame rate $f = 1/\tau$ is $250\,\mathrm{Hz}$ or $800\,\mathrm{Hz}$). While the horizontal velocity distributions display one peak located near zero, the PDFs of the vertical component clearly show two nearby peaks, see Fig. 3.9. We fit the former distributions by a simple Gaussian, and the latter ones with a sum of two Gaussians, plotted in the same figure by colour lines. For the vertical velocity

PDFs we therefore obtain two central velocities, denoted v_1 and v_2, see Tab. 3.3. Note in passing that the fits describe only the central parts of the PDFs; heavy tails are not captured by the fits and will be discussed later.

Table 3.3: Experimental conditions. T: thermodynamic temperature; P: applied heating power; f: camera frame rate; v_1, v_2 central velocities obtained from the vertical velocity distributions; v_n: estimated normal fluid velocity; v_{ns}: counterflow velocity; R: length scale ratio. See text for details.

	T [K]	P [W]	f [Hz]	v_1 [mm/s]	v_2 [mm/s]	v_n [mm/s]	v_{ns} [mm/s]	R
B1	1.39	1.22	800	9.7	22.1	24.6	26.5	2.0
B2	1.36	0.61	800	5.4	13.6	16.2	17.3	0.8
B3	1.52	1.23	250	4.2	10.3	12.8	14.7	2.3
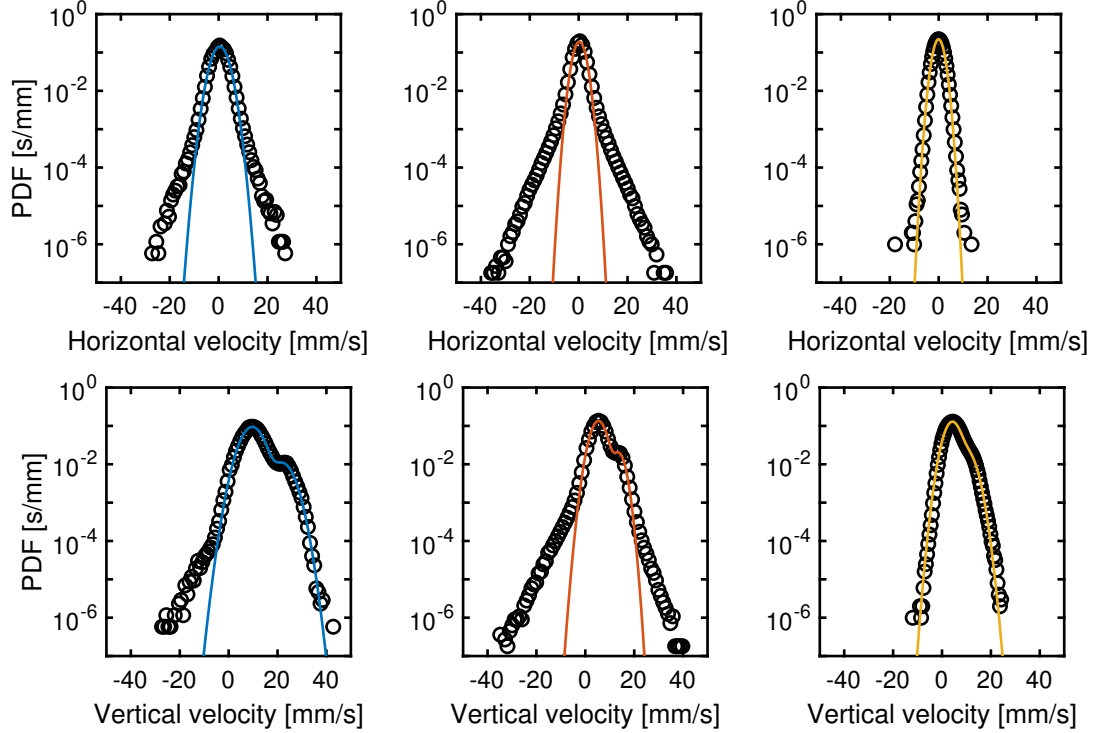
Figure 3.9: PDFs of the particle velocity (black points) and the corresponding Gaussian fits (colour lines). Left, middle and right columns: data sets B1, B2 and B3, respectively. Note the log-linear scale.

If we compare the central velocities with the normal fluid velocity, calculated from Eq. (1.4), we find only a partial agreement, that is, the calculated value of v_n is only approximately equal to v_2; a similar outcome is obtained for $2v_1$. The discrepancy can be explained by heat leaks from the channel to the experimental volume of the cryostat. As thermal counterflow is expected to occur also outside of the visualization cell, the effective area over which the dissipated heat spreads is a priori unknown, but we can assume that the value is close to the cross section of the experimental volume, $(51\,\text{mm})^2$ in our case. Here, we introduce a novel

technique for the estimation of v_n based solely on the observed particle dynamics, that is, central velocities v_1 and v_2.

Due to the density mismatch between solid deuterium (employed as the source of particles) and liquid helium, their settling cannot be neglected and modifies the central velocities. The effect can be accounted for by introducing a slip velocity v_{sl}. Based on Ref. [105], we can write $v_1 = v_n/2 + v_{sl}$ and $v_2 = v_n + v_{sl}$. It then follows that

$$2v_1 = v_2 + v_{sl}, \tag{3.8}$$

which is neatly verified by our data.[10] Linear fit of Eq. (3.8) yields $v_{sl} = -2.5\,\text{mm/s}$. If we set this value equal to the terminal velocity of a spherical deuterium particle settling in He II, we can employ Eq. (2.3) to estimate the corresponding particle size. For $1.4\,\text{K}$, we obtain that the particle radius is ca. $5\,\mu\text{m}$, which agrees well with the typical size of particles employed in our experiments (see Fig. 2.1 for the typical size distribution).

Equation (3.8) and relations leading to this equation allow us to estimate the normal fluid velocity as $v_n = v_2 - v_{sl}$. We can now calculate the counterflow velocity as $v_{ns} = (\rho/\rho_s)\,v_n$ and estimate the ratio R of the probed and quantum length scales. To estimate the probed scale we use the effective time scale of the Gaussian kernel, which yields $s_p \approx 5u_{abs}\tau$. The quantum scale is estimated from Eq. (3.3) and the resulting values of v_n, v_{ns} and R are summarized in Tab. 3.3.

The key observation of this experiment is displayed in the left panel of Fig. 3.10, where we plot vertical positions of several particles as the function of time. The particles intermittently switch between two different velocities, which can be recognized by two distinct slopes. Time evolution of the velocity and acceleration of the highlighted trajectory is shown in the right panel of Fig. 3.10. We can see that the regimes can be now distinguished as intervals of a relatively constant velocity separated by brief events of large acceleration or deceleration. When we plot these data in the velocity-acceleration space, we obtain a trajectory shaped like a repeating loop, displayed by white points in Fig. 3.11.

Owing to the specific trajectory shape, we suggest a separation scheme that splits the velocity-acceleration space into four subspaces called slow (S), fast (F), acceleration (A) and deceleration (D), indicated in Fig. 3.11 by red lines. The curves that split the space are: (i) a hyperbola with the focus in $[v_1, 0]$ and semi-axes of lengths $2\sigma(v_1)$ and $2\sigma(a_y)$, (ii) a hyperbola with the focus in $[v_2, 0]$ and semi-axes of lengths $2\sigma(v_2)$ and $2\sigma(a_y)$ and (iii) a segment between points $[v_2 - 2\sigma(v_2), 0]$ and $[v_1 + 2\sigma(v_1), 0]$. Central velocities v_1, v_2 and the corresponding standard deviations $\sigma(v_1)$, $\sigma(v_2)$ are obtained from the Gaussian fits of the PDFs (Fig. 3.9), while the standard deviation of the particle vertical acceleration $\sigma(a_y)$ is directly calculated from the data. The mean acceleration is found to be practically zero, for all considered cases.

The scheme allows us to split individual trajectories into segments corresponding to one of the four motion regimes (S, F, A, D). Lengths of the segments, defined as the position difference between their first and last points, are found

---

[10]The dependence is plotted as Fig. 5 in Ref. [81], reproduced here as Attachment 4.
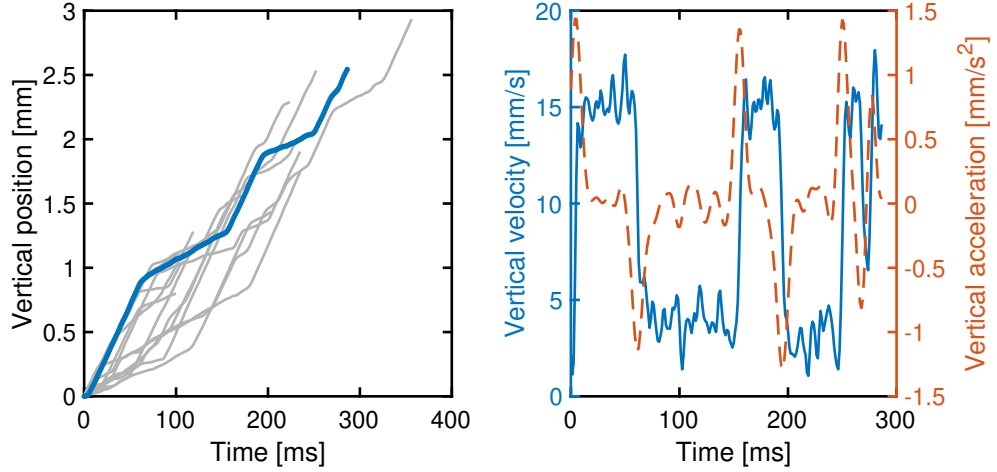
Figure 3.10: *Left panel:* several exemplary trajectories from the data set B2. *Right panel:* vertical velocity and acceleration of the highlighted trajectory as the function of time.

to be comparable to the intervortex distance for A and D segments; however, much broader length distributions are observed for the segments of type S and F. Relatively common are lengths that exceed the intervortex distance, indicating that the particles can travel long distances without changing their motion type. The vortex tangle, experienced by the particles, appears spatially inhomogeneous, which is a feature observed also in numerical simulations of quantum turbulence [106].

Note that a similar separation scheme was introduced already in Ref. [105]. The authors split their data solely on the basis of the vertical particle velocity into two groups, denoted G1 and G2 and loosely corresponding to the respective motion regimes S and F. The distributions of the horizontal particle velocity are reported to be heavy-tailed for the G1 data and nearly Gaussian for the G2 data. Based on this observation, the authors claim that particles from the G2 group only interact with the normal component of He II. Our data suggest a different physical picture, though. When we plot the horizontal velocity distributions of particles that belong to the S and F regimes, see Fig. 3.12, we find that non-classical tails are apparent in both cases, indicating that interactions with the vortex tangle cannot be neglected for neither of the motion regimes.

The discrepancy between our experimental results and those reported in Ref. [105] is likely due to differently sized data sets. While our sets B1–B3 contain 1.4, 8.6 and 1.1 million velocity points, respectively, the conclusions formulated in Ref. [105] are based on data sets that contain at least one order of magnitude less points than ours.[11] It is then not surprising that relatively small data sets failed to resolve the tails, which reflect the occurrence of extreme yet relatively rare events.

One may note that the tails in Fig. 3.12 are well-visible only for data sets B1 and B2. For B3, we find instead that both motion regimes display nearly Gaussian

---

[11]Size of the data sets reported in Ref. [105] can be estimated from the published PDFs, whose areas are normalized by the total number of considered data points.
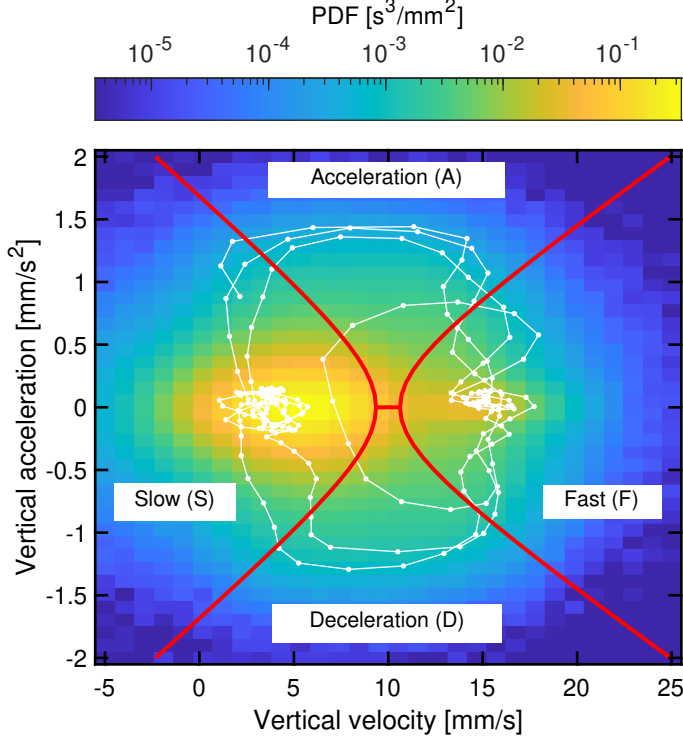
Figure 3.11: Velocity-acceleration space for the data set B2. Colour map in the background: bivariate PDF of the velocity-acceleration pairs. White points: trajectory from Fig. 3.10. Red lines: individual separation curves that split the space into four motion types, see text for details.

distributions. Such outcome is consistent with the velocity distribution shown in the top right panel of Fig. 3.9, which lacks the tails as well. The estimated length scale ratio, ca. 2.3, is the largest one considered and this data set is visualized with the smallest camera frame rate. It is likely that these factors combined led to a quasi-classical particle dynamics, usually observed for larger values of R.

Nevertheless, our results strongly suggest that the particle-vortex interactions are fairly ubiquitous in thermal counterflow. It now seems that a more promising approach towards the investigation of turbulence in the normal component offer metastable He_2^* molecules that can be generated in He II by femtosecond laser pulses [107]. Clouds of these molecules, which can be made visible by the laser-induced fluorescence, interact solely with the normal component of He II.

Furthermore, we argue that the strength of these interactions differs between the motion regimes. The trajectories of particles moving with the normal fluid velocity are found straighter than slower ones [31,103], which suggests that erratic trajectories can be related to frequent interactions of the particles with the vortex tangle. Here we quantify the shape of individual trajectory segments by the velocity orientation angle, ϑ introduced in Ref. [102] and defined as

$$\vartheta = \arctan\left(\frac{u_y}{u_x}\right), \tag{3.9}$$

where u_x, u_y are the Cartesian components of the particle velocity vector $\boldsymbol{u}$. Note that ϑ can be defined in the full angular range, from $-\pi$ to π. In this notation,
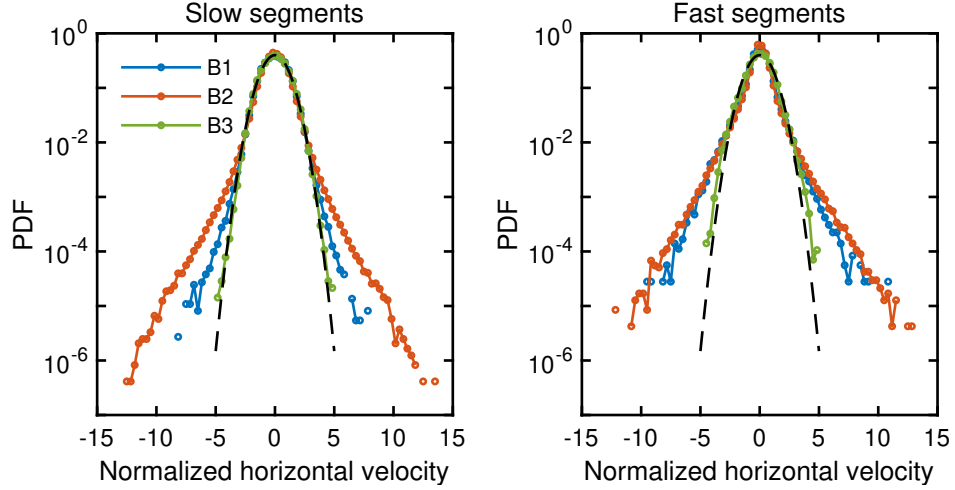
Figure 3.12: PDFs of the horizontal particle velocity of the motion type S (left) and F (right). Data are normalized by the subtraction of the mean value and the division by the standard deviation. Black dashed line: normal (Gaussian) distribution. Note the log-linear scale.

the normal fluid direction corresponds to $\vartheta = \pi/2$.

We plot PDFs of the orientation angle in the left panel of Fig. 3.13, for all data sets (colour points). The distributions sharply peak near $\pi/2$, which indicates a strong preferential orientation of the particle velocity vector in the direction of the normal fluid. For the sake of comparison, we plot a similar distribution, obtained at $1.39\,\mathrm{K}$ with the heater switched off (black line). In this case, the detected particle motion is only due to the decaying flow caused by resuspension pulses[12] and the particles do not display any preferred direction of motion. Small equidistant peaks are artefacts common for visualization experiments, discussed in our original publication [81].

Nonzero width of the ϑ distributions obtained in thermal counterflow accounts for the deviations from straight tracks. To resolve the contributions from the respective motion regimes, we use the outlined separation scheme. In the right panel of Fig. 3.13 we plot the distributions of ϑ for S, F, A and D segments, respectively; their standard deviations are displayed in the inset. We find that the particles follow the most erratic trajectories when they are found in the regime S, the straightest ones are instead observed for the fastest regime F. This likely means that fast particles experience relatively weak interactions with the vortices, e.g., via the pressure gradient forces (Eq. 2.6), while slow particles are subjected to strong interactions originating from nearby vortices, perhaps those that currently trap the particles in question.

As we have shown, the presence of the particle-vortex interactions leads to specific motion patterns in the direction parallel to the heat flux. However, we remind that non-classical velocity distributions are observed as well in the horizontal direction. It is hence sound to assume that more complex motion patterns might

---

[12]We regularly inject pure He gas into He II to resuspend the particles back to the camera FOV.
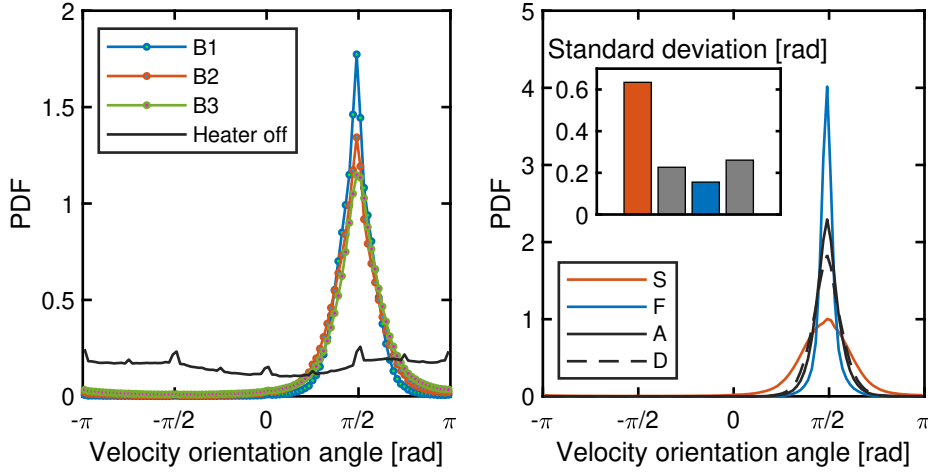
Figure 3.13: PDFs of the velocity orientation angle ϑ. *Left panel:* distributions of unconditioned data. *Right panel:* distributions conditioned by the motion regime. Data from the data set B2. Inset: standard deviation of ϑ for each motion regime, shown in the order that corresponds to the typical time evolution of the particle motion, i.e., S $\rightarrow$ A $\rightarrow$ F $\rightarrow$ D.

exist in the full, multi-dimensional velocity-acceleration space. Our data display a hint of such behavior, but additional experimental efforts are required to obtain firm conclusions. On the other hand, it should be relatively easy to employ the outlined tools for the analysis of dedicated numerical simulations of quantum turbulence [66].

4 Counterflow jets

Steady jets form when the fluid is continuously pushed through a small opening (nozzle) into a sufficiently large quiescent reservoir. Since the nozzle geometry has a significant impact on the resulting flow [108], from now on we focus only on round jets, formed past nozzles with the circular cross section. The jets usually obtain their energy from the steady influx of momentum and are routinely realized in classical [109] and cryogenic experimental facilities [110], as well as in a large number of engineering and industrial applications.

Somehow peculiar are the counterflow jets that exist only in quantum fluids such as He II [111]. They gain their energy from the heat dissipated by a heater enclosed in a small volume, open to the surrounding helium bath through the nozzle. When the heater is powered, thermal counterflow establishes inside the nozzle; the normal component flows out and the superfluid component flows into the enclosure.

In this chapter we briefly review the properties of the counterflow jets (§4.1). In §4.2 we summarize our results on the measurement of the vortex line density in the counterflow jets, carried out at Institut Néel in Grenoble. Scaling laws observed in the acquired data are discussed in §4.3.

4.1 Introduction

The dynamics of round jets depends on the nozzle diameter D and the fluid velocity at the nozzle exit. Following Ref. [59], the characteristic velocity in the case of the counterflow jets is the normal fluid velocity, v_n inside the nozzle and the corresponding jet Reynolds number is defined as

$$\mathrm{Re_j} = \frac{\rho D v_\mathrm{n}}{\mu_\mathrm{n}},\qquad(4.1)$$

where ρ is the He II density and μ_n represents the dynamic viscosity of the normal component; both quantities are tabulated in Ref. [18]. Direct visualization of the counterflow jets [59] indicates they become turbulent when $\mathrm{Re_j} > 5000$. In comparison, a classical jet with a similarly defined Reynolds number becomes turbulent at $\mathrm{Re} \approx 2000$ [108].

Turbulent counterflow jets were extensively studied in the past, because they represent a boundary-free alternative to the channel counterflow [111], making
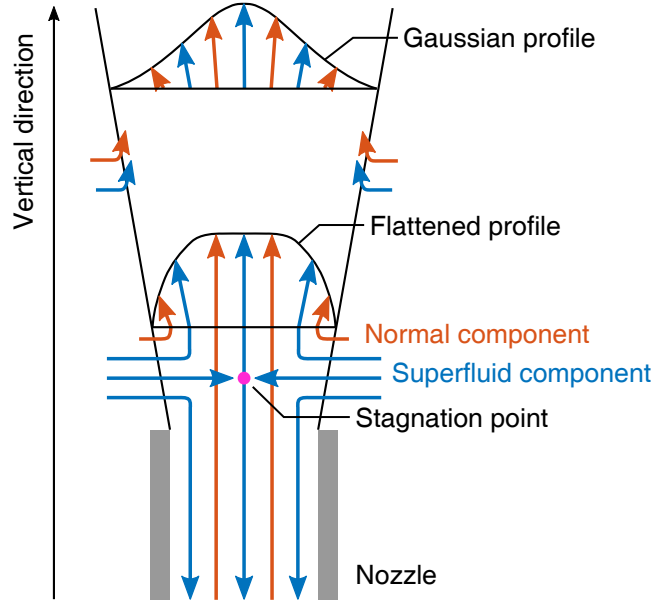
Figure 4.1: Flow fields of the normal and superfluid components in a counterflow jet. Adapted from [117].

them suitable for the investigation of the mutual friction forces. Presence of the vortex tangle in these jets, first detected by negative ion trapping [112], suggests that the coupling between He II components, mediated by the quantized vortices, cannot be neglected. Indeed, subsequent measurements of temperature gradients along the jet axis [113] and the second sound investigations [114, 115] lead to the conclusion that the normal and superfluid components are tightly coupled some small distance above the nozzle and they flow with zero relative velocity.

The flow field of the superfluid component is then twofold, as sketched in Fig. 4.1. The superfluid flows in the direction opposite to the normal fluid inside the nozzle and in its close vicinity. Above the nozzle a stagnation point can be found, followed by the region where the superfluid component flows together with the normal fluid. Coflowing arrangement above the nozzle requires a transfer of momentum between the normal fluid ejected from the nozzle and the otherwise stationary superfluid component. This is achieved by the process analogous to turbulent entrainment known for classical jets [108, 111]. As a result, the coflow velocity becomes $f_n v_n$, where $f_n = \rho_n / \rho$ is the temperature-dependent normal fluid fraction. Such velocity scaling was confirmed experimentally by the laser Doppler velocimetry measurements performed as close as $0.5D$ above the nozzle [116, 117].

The velocity field in the region above the nozzle is spatially inhomogeneous. Experimental evidence suggests that the radial profile of the fluid velocity is first flattened [59], but a self-similar profile quickly develops, at a distance of a few nozzle diameters [118]. Two similar shapes of the velocity profiles are reported in literature, the Görtler and the Gaussian one [108, 118]; robust experimental evidence favours the second one [119], which can be expressed in the cylindrical

coordinate system (r, y) as

$$v(r, y) = v_0(y) \exp\left[-\left(\frac{r}{\beta y}\right)^2\right],\tag{4.2}$$

where $v_0(y)$ is called the centerline velocity and β denotes the jet growth rate. For classical jets, $\beta \approx 0.11$ [109]. The centerline velocity follows in both classical and counterflow jets [108, 118]

$$\frac{v_0}{f_\mathrm{n} v_\mathrm{n}} \sim \left(\frac{y}{D}\right)^{-1}.\tag{4.3}$$

Note that for classical jets, $f_\mathrm{n} v_\mathrm{n}$ is replaced in the equation above by the fluid velocity at the nozzle exit.

Equations (4.2) and (4.3) indicate that the kinetic energy of the flow is adiabatically transferred between the planes perpendicular to the nozzle symmetry axis. If we consider that the kinetic energy, normalized by the fluid density, is equal to $v^2/2$, the total energy contained in the jet, per unit height, is equal to

$$\mathcal{E}_y = \frac{\mathrm{d}E}{\mathrm{d}y} = \int_0^\infty 2\pi r \frac{v^2(r, y)}{2}\,\mathrm{d}r = \pi v_0^2 \int_0^\infty \exp\left[-2\left(\frac{r}{\beta y}\right)^2\right] r\,\mathrm{d}r = \frac{\pi}{4}\left(v_0 \beta y\right)^2.\tag{4.4}$$

It follows from the right-hand side that $\mathcal{E}_y$ is constant because of the $v_0 \sim y^{-1}$ scaling introduced by Eq. (4.3), which means that the energy is indeed conserved between planes.

Below, we present spatially resolved measurements of the vortex line density $L(r, y)$ in counterflow jets, as the spatial structure of L is largely unknown by date. Such data can be regarded as complementary ones to the just outlined structure of the fluid velocity.

4.2 Measurement of the vortex line density

The central tool of this work is a pair of miniature second sound tweezers, described in §2.2. The sensor consists of a small open cavity, where we transmit a standing wave of the second sound, whose amplitude is sensitive to the local value of the vortex line density found in the cavity. A counterflow jet is generated at the bottom of a 100 L helium cryostat, see Fig. 4.2 for the photography of the experimental setup. We use a nozzle made of brass, with $D = 2\,\mathrm{mm}$ diameter, attached to the bottom flange of the cryostat insert. The nozzle encloses a custom pyramidal box equipped with the heater.

The box (sketched in Fig. 5.8 below) is 3D-printed from Cu-filled PLA. Pyramidal shape of the box reflects the square shape of the heater, placed at the bottom of the box. Inner walls of the device are coated with Stycast 2850-FT epoxy to suppress the penetration of He II through the plastic, partially preventing heat losses from the box towards the surrounding bath. Linear contraction of the box along its height aims to decrease the fluid recirculation inside the box.

A steady jet is formed above the nozzle shortly after we supply the heater with a constant current. In this work, we consider heating powers supplied to the heater in the range from 190 mW to 780 mW, which were used to generate jets at three distinct temperatures, 1.65 K, 1.95 K and 2.10 K, see Tab. 4.1 for detailed information on the data sets.
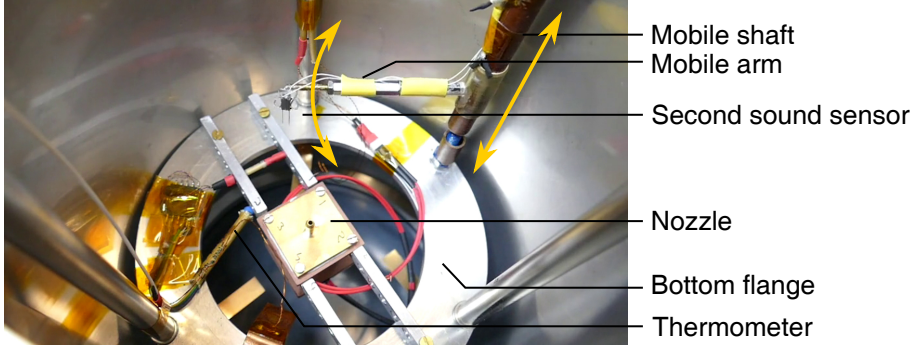
Figure 4.2: Photography of the bottom flange of the cryostat insert. Nozzle enclosing the heater box is attached to the flange, while the second sound sensor is mounted on a mobile arm that allows its displacement in two directions marked by yellow arrows. See the main text for details.

Table 4.1: Experimental conditions of individual data sets. Displayed symbols are used in Figs. 4.5–4.7. T: thermodynamic temperature; $f_n = \rho_n/\rho$: normal fluid fraction; P: dissipated power; v_n: normal fluid velocity inside the nozzle, Eq. (1.4); Re_j: jet Reynolds number, Eq. (4.1).

		T [K]	f_n	P [mW]	v_n [m/s]	$\text{Re}_j\,/10^3$
○	JA1	1.646	0.19	194	0.78	175
□	JA2	1.650	0.19	381	1.51	338
△	JA3	1.637	0.19	776	3.24	726
▽	JB1	1.947	0.48	194	0.26	55
◇	JB2	1.947	0.48	381	0.52	108
✶	JB3	1.952	0.48	776	1.03	215
✕	JC3	2.095	0.73	776	0.65	107

Note that the values of v_n, obtained from Eq. (1.4), should be rather regarded as over-estimates of the actual values, as we assume that the flow inside the nozzle is isothermal. In reality, the temperature inside the heater box is higher than the one reported in Tab. 4.1. Relevant temperature increase can be estimated from Ref. [113] as

$$\Delta T = H \left(\frac{4P}{\pi D^2}\right)^3 b(T), \tag{4.5}$$

where $H = 8\,\text{mm}$ is the length of the nozzle, the term $4P/(\pi D^2)$ denotes the heat flux in the nozzle and $b(T) < 2 \cdot 10^{-14}\,\text{K·s}^6\text{·kg}^{-3}\text{·m}^{-1}$ is a proportionality

coefficient related to the force of mutual friction.[13] Cubic scaling of ΔT with the heating power results in the large span of temperature increments: we obtain $0.04\,\mathrm{K}$ for $194\,\mathrm{mW}$, $0.28\,\mathrm{K}$ for $381\,\mathrm{mW}$ and $2.4\,\mathrm{K}$ for $776\,\mathrm{mW}$, respectively. Such outcome suggests that, in the case of the highest heating power, the boiling of the normal-phase helium must occur in the nozzle. However, such scenario is unlikely to happen, as the heat might as well leak from the heater box through its walls or via the joint between the plastic device and the nozzle. Moreover, the box was tested in an optical cryostat and we did not observe bubbles leaving the nozzle, at similar temperatures and heating powers as discussed here.

Our claims are supported by the direct visualization of the counterflow jets, obtained in the experimental cell depicted in Fig. 5.8 below, at $1.65\,\mathrm{K}$ and for similar heating powers as reported in Tab. 4.1. We know from the preliminary data that the typical velocity achieved by deuterium particles is of the order of $100\,\mathrm{mm/s}$, i.e., 10-times less than the values of v_n calculated in Tab. 4.1.

In conclusion, it is likely that the actual values of $\mathrm{Re_j}$ are smaller than those reported in Tab. 4.1 roughly by one order of magnitute. However, these values are still larger than the critical Reynolds number reported in Ref. [59], which means that the jets are convincingly turbulent.

The second sound twezers are attached to a mobile arm, which perpendicularly extends from the vertical shaft located off the cryostat symmetry axis. A pair of room-temperature stepper motors (Dynamixel MX-64AR) precisely displace and rotate the shaft, which in turn displaces the sensor along a circle that intentionally crosses the cryostat axis. We denote the sensor angular position as η and we set $\eta = 0$ to the position at which the sensor is located above the nozzle. The angle can be then transformed into the radial distance r of the sensor as

$$r = 2d_\mathrm{arm} \sin\left(\frac{\eta}{2}\right), \tag{4.6}$$

where $d_\mathrm{arm} = 73\,\mathrm{mm}$ is the effective length of the mobile arm.

The setup is designed to systematically sweep across the jet axis, at different axial distances y. For each sensor position, defined by η, r and y, we attempt to measure the corresponding second sound amplitude. For data sets JA1–JA3 we directly measure this amplitude by driving the second sound at a fixed frequency, $f_0 = {}$ $= 37.22\,\mathrm{kHz}$ (we have previously found that f_0 corresponds to the 18th harmonic mode displayed in Fig. 2.9). Excitation with a constant frequency is here possible because, at $T \approx 1.65\,\mathrm{K}$, the temperature dependence of the second sound velocity plateaus [18]. Hence, small temperature fluctuations, occurring in almost every cryogenic experiment, have only a negligible effect on the resonance frequency.

We suppress the experimental noise by performing multiple sweeps (usually 25) at the same axial distance, which are later averaged. An example of the averaged signal is displayed in Fig. 4.3. Colour lines represent individual angular sweeps performed equidistantly between $18\,\mathrm{mm}$ and $63\,\mathrm{mm}$ away from the nozzle. A

---

[13]The value of $b(T)$ is estimated from Fig. 14 in Ref. [113] for $T = 1.65\,\mathrm{K}$; for other temperatures considered in this work, the coefficient is not larger than the value reported in the main text. Note that the coefficient is originally given in cgs units.

systematic decrease of the second sound amplitude near $\eta = 0$ neatly depicts a dense vortex tangle localized along the jet axis, which spreads in the radial direction with the axial distance. Note that the signal minimums display a constant offset, which is estimated as $\eta_0 = (1.9 \pm 0.3)°$ and marked by the black dashed line in Fig. 4.3. This value corresponds to the actual angular position at which the sensor crosses the jet symmetry axis and we use it to recalibrate the positions of the sensor.
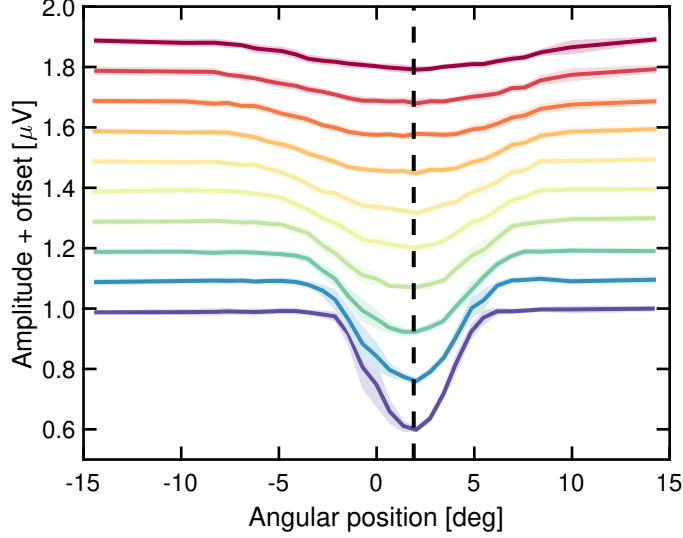

Figure 4.3: Acquired second sound signal for the data set JA3 as the function of the jet angular position η. Colour lines: average amplitude obtained from 25 angular sweeps. Colour areas: one standard deviation interval. Different colours code different axial distances of the sensor, from $18\,\mathrm{mm}$ (dark blue) to $63\,\mathrm{mm}$ (dark red) with steps of $5\,\mathrm{mm}$. Black dashed line: average of signal minimums marks the offset $\eta_0 = 1.9°$, used to recalibrate the positions of the sensor.

It is not possible to employ the same approach for data sets JB1–JB3 and JC3, which were obtained at temperatures where the second sound velocity is steeply temperature dependent. We hence perform here a full frequency sweep at each sensor position and we estimate the corresponding sound amplitude from the circle fit of the in-phase and quadrature signal components (Fig. 2.7).

Vortex line density L is calculated as the function of r and y by using Eq. (2.15). Note that the amplitude A_0 and the peak width Δ_0 were found by direct fitting of the frequency sweeps acquired in quiescent He II (data sets JA1–JA3) or from the frequency sweeps measured at the maximum and minimum angular positions, i.e., far away from the jet (data sets JB1–JB3 and JC3). The resulting maps of the vortex line density—some of them are plotted in Fig. 4.4—provide a neat and unprecedented visualization of the vortex tangles in this kind of flow.

Note that the largest measured vortex line density is of the order of $10^{10}\,\mathrm{m^{-2}}$, which corresponds to the mean intervortex distance equal to $10\,\mathrm{\mu m}$. This value is of the same order of magnitude as the typical intervortex distance (denoted as s_q) observed in the visualization experiments summarized in §3. However, in the present case, the tangle density quickly decreases with the axial and radial distances. Finite sensitivity of the sensor, combined with the presence of experi-
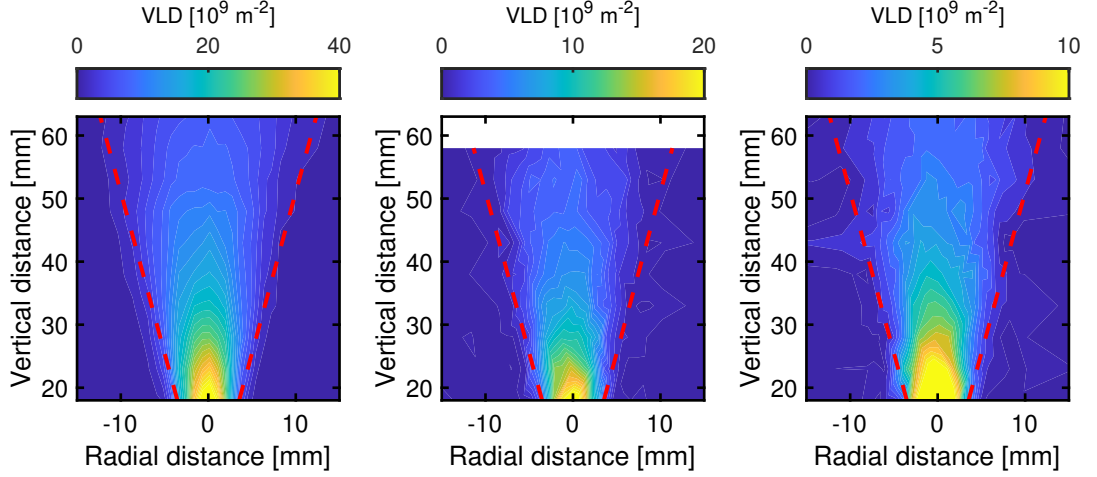
Figure 4.4: Maps of the vortex line density in cylindrical coordinates (r, y). Displayed data sets: JA3 (left), JB3 (middle) and JC3 (right panel). Note different colour scales, indicated by the colour bars above the maps. Red dashed line: cross section of the cone with the opening half-angle of 11.1°, see §4.3 for additional information.

mental noise, limits the maximum accessible axial distance to ca. 70 mm ($35D$). We also start our measurements at the minimum distance of 18 mm ($9D$), because the second sound waves are likely advected from the sensor by the action of a large fluid velocity in the close vicinity of the nozzle, which leads to the parasitic sound attenuation, not directly linked to the vortex tangle [78]. Considering that the velocity of He II is of the order of 100 mm/s at the nozzle exit, we can estimate from Eq. (4.3) that this velocity is reduced to about 10 mm/s at the minimum distance probed by the second sound sensor.

4.3 Scaling laws

Although the fluid velocity and the vortex line density are conceptually different quantities, we find that radial VLD profiles display a shape similar to a unimodal Gaussian peak, i.e., analogous to Eq. (4.2) valid for the velocity profiles. We introduce the fitting function for the vortex line density,

$$L(r, y) = L_0(y) \exp\left[-\left(\frac{r}{r_{\mathrm{j}}(y)}\right)^2\right], \tag{4.7}$$

where two free parameters are the centerline density L_0 and the jet width r_{j}. Good agreement between the experimental data and Eq. (4.7) allows us to determine these parameters and to analyze their dependence on the axial distance y.

We start with the jet width. A neat linear scaling of r_{j} with y is apparent, see Fig. 4.5. We only plot here the profiles with a large enough amplitude, i.e., large enough L_0, as they are not appreciably affected by the experimental noise. We specifically plot profiles that meet $L_0 \geq 2.2 \cdot 10^9\,\mathrm{m}^{-2}$; weaker profiles follow this trend only qualitatively. Since all the displayed data collapse onto a single line,

we conclude that the growth of the jet width does not depend on temperature nor the applied heat flux. Considering that a similar behaviour holds also for the growth of the velocity profile width (Eq. 4.2), we can write

$$r_{\rm j} = \beta_L(y - y_0), \tag{4.8}$$

where β_L denotes the growth rate of the vortex tangle and y_0 is the virtual origin of the jet. Collective linear fit of the displayed data (black line in Fig. 4.5) yields $y_0 = (-1.8 \pm 1.6)$ mm, which means that the jet origin nearly matches the tip of the nozzle. For the growth rate we obtain $\beta_L = 0.139 \pm 0.006$.
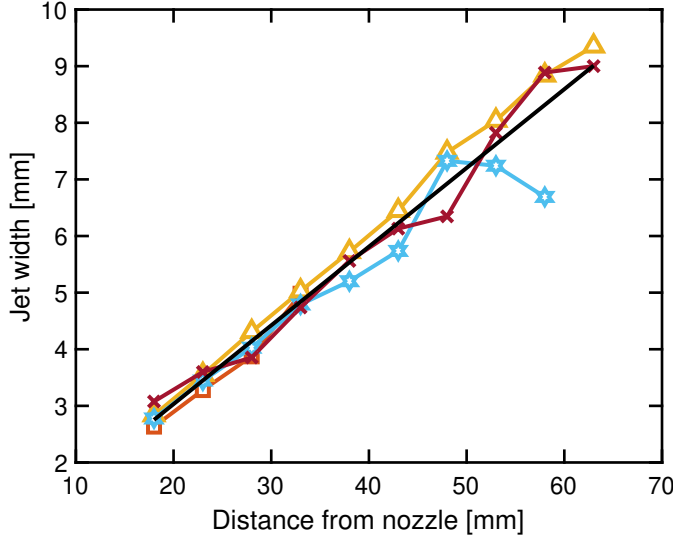
Figure 4.5: Jet width, $r_{\rm j}$, obtained from the fits of Eq. (4.7), as the function of the axial distance. Only values from the profiles that meet $L_0 \geq 2.2 \cdot 10^9 \, \text{m}^{-2}$ are displayed. Black line: collective linear fit reveals the jet growth rate $\beta_L = = 0.139 \pm 0.006$. Symbols as in Tab. 4.1.

This value is larger by about $20\,\%$ than the growth rate of the velocity profiles, equal to $\beta = 0.11$ for classical jets, whose Reynolds numbers are of the order of 10^5 [109], i.e., comparable to $\text{Re}_{\rm j}$ achieved in the present work (Tab. 4.1). Similar results are reported for jets with $\text{Re}_{\rm j}$ of the order of 10^4, with different nozzle geometries [120]. We can hence say that both the fluid velocity and the vortex line density display mutually compatible spatial structures.

Following the two-sigma rule for Gaussian peaks, $95\,\%$ of the vortex tangle is localized within the interval $[-\sqrt{2}r_{\rm j}, \sqrt{2}r_{\rm j}]$. In other words, we can enclose the vortex tangle by a cone with the half-angle equal to $\arctan(\sqrt{2}\beta_L) = (11.1 \pm 0.5)^\circ$. Cross section of this cone is displayed by red dashed lines in each panel of Fig. 4.4.

Centerline VLD, L_0 is plotted as the function of y in the left panel of Fig. 4.6 for all considered data sets. It steeply decreases with the axial distance, following a power law. The corresponding exponent is found to vary between the data sets. We estimate it as $-3/2$, which agrees well with the scaling of the largest L_0 values. If we plot L_0 as the function of the rescaled coordinate, $(y/D)^{-3/2}$, we obtain nearly-linear functions featuring a wide range of slopes. In order to visualize the anticipated scaling and compare individual data sets, we normalize

the slopes to unity, see the right panel of Fig. 4.6, where we observe that all data sets collapse approximately onto a single line, confirming the suggested power law scaling.
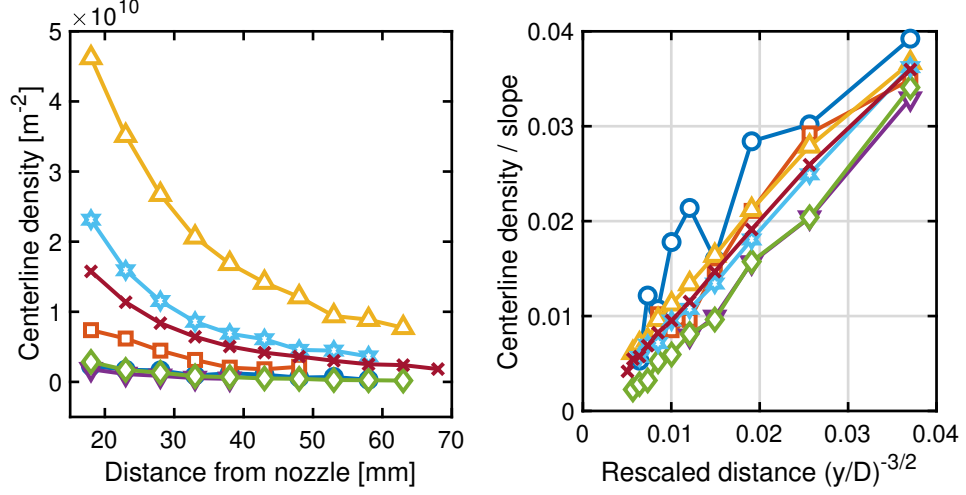
Figure 4.6: *Left panel:* centerline VLD, L_0 as the function of the axial distance y. *Right panel:* same data plotted as the function of the rescaled distance, normalized to a unit slope. Symbols as in Tab. 4.1.

The obtained scaling exponent can be interpreted in terms of the fluid velocity. If we consider that the centerline velocity follows $v_0 \sim (y/D)^{-1}$ (Eq. 4.3), we find for the centerline density that $L_0 \sim v_0^{3/2}$. Such scaling between the vortex line density and the fluid velocity is typical to the coflow of He II components (Eq. 1.8). For instance, it is reported in Ref. [32] that this exponent holds for a mechanically forced channel flow of He II in the wide velocity range, at least from 1 mm/s to 1 m/s, and for temperatures between 1.17 K and 2.16 K. Since the present data securely fall into these intervals, we can say that the observed scaling further verifies the idea of the coflowing He II components in the counterflow jets, as sketched in Fig. 4.1.

Although the outlined interpretation of $L_0 \sim y^{-3/2}$ is compatible with the current knowledge on the counterflow jets, our experimental observations are somehow limited. In particular, we currently probe a relatively narrow range of axial distances, between 9 and 35 nozzle diameters, which deny a precise determination of the scaling exponent. Indeed, linear fits of $\log(L_0)$ versus $\log(y)$ dependence display deviations from the expected $-3/2$ slope, especially for data sets JA1, JB1 and JB2. Further experimental effort is required to reduce the experimental noise, e.g., by performing multiple scans along the jet vertical axis, and to prove that the measured dependencies are reproducible.

Direct visualization of the counterflow jets, already mentioned above, indicates that the mean vertical velocity of solid deuterium particles is consistent with the Gaussian radial profile, Eq. (4.2). However, the scaling of the centerline velocity given by Eq. (4.3) was not reproduced in our experiments; although we observe that v_0 decreases with the axial distance, a power-law dependence, reported for the counterflow jets in Ref. [118], is yet to be verified in our setup.

A useful step towards the validation of the proposed VLD profile shape is to calculate the total length of vortex lines, observed at the given axial distance. Upon the assumption of axial symmetry of the vortex tangle, we can calculate the vortex line length per unit height as

$$\mathcal{L}_y = \frac{\mathrm{d}\mathcal{L}}{\mathrm{d}y} = \int_0^\infty 2\pi r L(r,y)\,\mathrm{d}r = 2\pi L_0 \int_0^\infty \exp\left[-\left(\frac{r}{r_\mathrm{j}}\right)^2\right] r\,\mathrm{d}r = \pi L_0 r_\mathrm{j}^2, \qquad (4.9)$$

where we used Eq. (4.7) to plug in for $L(r,y)$ before explicitly solving the integral.

Note that $\mathcal{L}_y$ can be estimated in two independent ways. One is to evaluate the right-hand side of Eq. (4.9). The other one is to evaluate the integrand from the left-hand side, i.e., $2\pi r L(r,y)$, and numerically integrate between the endpoints $(-r_\mathrm{max}, 0)$ or $(0, r_\mathrm{max})$, where r_max is the maximum radial distance probed by the sensor. Since the VLD profiles are symmetric, the absolute value of both integrals should be the same, so we take for the estimate of $\mathcal{L}_y$ their (absolute) average.

We plot both outlined estimates of $\mathcal{L}_y$ as the function of the axial distance in Fig. 4.7. Colour symbols indicate the result of a direct numerical integration using the trapezoidal rule; the corresponding grey symbols denote the same quantity estimated from L_0 and r_j.
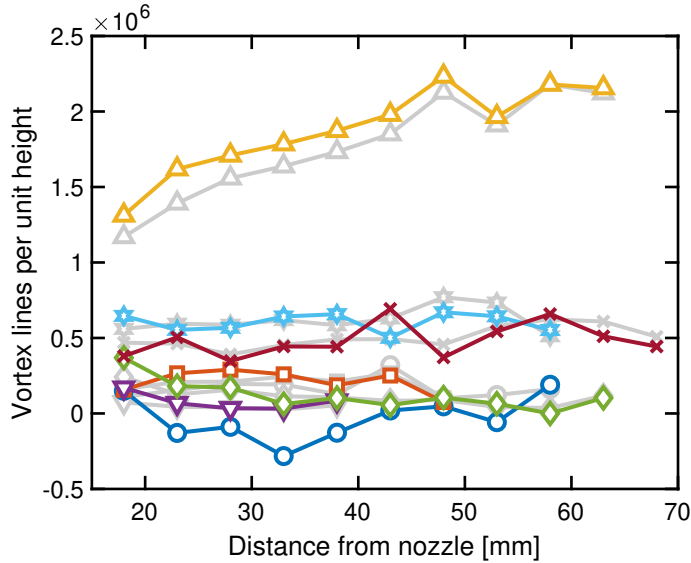
Figure 4.7: Length of the vortex lines per unit height as the function of the axial distance. Colour symbols: result of numerical integration. Grey symbols: estimate based on L_0 and r_j, see the right-hand side of Eq. (4.9). Symbols as in Tab. 4.1.

Note first that the direct integration and use of Eq. (4.9) provides comparable results. Somehow different are only values obtained for the data set JA1 (blue circles), where we observe that some values of $\mathcal{L}_y$ obtained by the integration are negative. These unphysical data points originate from Eq. (2.15), which yields negative VLD when $A > A_0$. The occurrence of such data points is related to the small signal-to-noise ratio of the measured second sound amplitude. For the remaining data sets we consistently obtain $\mathcal{L}_y > 0$, as expected.

The most significant outcome is that the line length is roughly constant for most of the data sets. In fact, the only obvious exception is the data set JA3 (yellow triangles), which we cannot explain at this point. If we consider that the energy contained by a quantized vortex is proportional to its length, the conservation of $\mathcal{L}_y$ between the planes perpendicular to the jet axis suggests, by analogy to $\mathcal{E}_y$ introduced in §4.1, another mechanism of energy transfer along the jet axis. In particular, it seems that the radial growth of the vortex tangle embedded in the jet might be due to the diffusion of the vortex lines rather than due to the generation of new vortices or stretching of the existing ones.

However, the outlined physical model is inconsistent with the proposed scaling laws for the jet width and the centerline density. If we consider that $r_\mathrm{j} \sim y$ and $L_0 \sim y^{-3/2}$, it follows from Eq. (4.9) that $\mathcal{L}_y \sim y^{1/2}$, in contrast to the experimental results. Instead, if we assume that $\mathcal{L}_y$ is constant and the jet width grows linearly with y, we should find that $L_0 \sim y^{-2}$ and, by consequence, that $L_0 \sim v_0^2$, i.e., the scaling analogous to thermal counterflow (Eq. 1.7).

It now seems that the vortex tangle in the jet combines the features of the coflow and counterflow turbulence, which is a rather unexpected behaviour. Especially interesting is the question of the VLD generation mechanism. Is the entire vortex line length produced in the close vicinity of the nozzle, i.e., in the counterflow regime? Does the vortex tangle holds memory of its generation process? Or, do the vortices additionally nucleate in the self-similar region further away? In order to shed more light on this physical problem (compared to the presented outcomes), further investigations are likely needed.

5   Macroscopic vortex rings

Somehow complementary flow structures to the jets, discussed in the previous chapter, are vortex rings, commonly subjected for experimental and theoretical enquiries [121]. Vortex rings are toroidal vortices, which usually gain their energy from a finite momentum influx, supplied, e.g., by the stroke of a piston. By analogy with the counterflow jets, we focus in this chapter on thermally generated turbulent rings in He II, which we study by the flow visualization and the second sound attenuation techniques. We show below that the macroscopic vortex rings are, in fact, conceptually different from the quantized vortex loops, which play an important role in quantum turbulence at small scales [122].

Basic concepts required for further discussions are introduced in §5.1. In §5.2 we describe how the rings can be visualized and in §5.3 we analyze their motions in the framework of the classical similarity theory [123], following mainly our own work [124]. Preliminary outcomes of the performed second sound study, supported by flow visualization, are reported in §5.4.

5.1   Introduction

In the most common experimental set up, the vortex rings are generated by a piston that ejects a relatively small amount of the fluid into a quiescent reservoir through some opening, e.g., an orifice or a nozzle. The geometry of the opening, as well as the piston velocity history affects the ring generation process and the occurrence of instabilities in the flow [121, 125]. Here, we consider rings that are formed past a circular nozzle of diameter D due to a piston that displaces the fluid with a constant velocity V_p over a distance L_p called the stroke. Following Ref. [121], the ring Reynolds number can be defined as $\mathrm{Re_r} = V_\mathrm{p} L_\mathrm{p}/2\nu_f$, where $\nu_f = \mu_f/\rho_f$ denotes the fluid kinematic viscosity.

In He II, we can replace the piston by a heater and we can generate the rings thermally, by supplying a short power pulse to the heater [126]. If we assume that the power pulse is orthogonal and the heat conductivity of He II is sufficiently large to diffuse the heat fast enough [18], we find that the analogue of V_p in He II becomes the normal fluid velocity v_n, and L_p becomes $v_\mathrm{n} t_\mathrm{p}$, where t_p indicates the pulse duration. The ring Reynolds number can be then rewritten as

$$\mathrm{Re_r} = \frac{\rho v_\mathrm{n}^2 t_\mathrm{p}}{2\mu_\mathrm{n}}, \tag{5.1}$$

where ρ is the density of He II and μ_n is the dynamic viscosity of the normal fluid component.

Despite the simplicity of their thermal generation, first macroscopic vortex rings in He II were generated by displacing a piston. Their direct visualization [127] revealed that they are similarly sized and propagate with a velocity comparable to that of the classical vortex rings. Acoustic measurements performed in a similar set up [128, 129] indicate that the rings consist of the normal and superfluid components, and the velocity circulation measured in both components is equal. In Ref. [129], the authors suggest that quantized vortices formed in the nozzle are responsible for the coupling of the He II components into a single velocity field, in a process similar to the counterflow jets [111]. This idea is generally accepted and consistent with the second sound measurements of thermally generated vortex rings [130] and recent numerical simulations [131].

Besides the Reynolds number, a vortex ring is also characterized by its circulation Γ_r. According to the slug model [121], one can write

$$\Gamma_r = \frac{V_p L_p}{2} = \frac{v_n^2 t_p}{2}. \tag{5.2}$$

Neat correspondence between the model and the experimentally obtained circulation was confirmed for both classical and superfluid rings [129, 132], at least relatively close to the nozzle.

Following Ref. [125], the formation of laminar or turbulent rings depends simultaneously on the Reynolds number (note $\mathrm{Re}_r = \rho \Gamma_r / \mu_n$) and the aspect ratio L_p/D, which is defined for thermally generated rings as

$$\frac{L_p}{D} = \frac{v_n t_p}{D}. \tag{5.3}$$

In approximate terms, if $\mathrm{Re}_r \gtrsim 10^4$ and $L_p/D \gtrsim 4$, the vortex rings are considered turbulent, which can be experimentally recognized by the formation of a visible wake that follows the ring along its path [125, 133].

5.2   Lagrangian pseudovorticity

We first investigate the vortex rings by flow visualization. Specifically, we use solid deuterium particles, whose motions are captured at 1 kHz or 2 kHz frame rates, in a 25 mm wide and 22 mm high field of view, located above the circular nozzle of $D = 5$ mm diameter. The nozzle is a part of the experimental cell, shown in Fig. 5.1, and is placed above a flat resistive heater. We supply the heater with orthogonal pulses of 500 ms or 1000 ms duration and various heat fluxes, ranging from ca. 350 W/m² to 4500 W/m², in the temperature range from 1.28 K to 1.95 K. We observe that the vortex rings form some distance above the nozzle and travel in the vertical direction.

We analyze 15 data sets, each consisting of multiple vortex ring realizations. For the sake of argument, we consider here eight representative sets, labelled
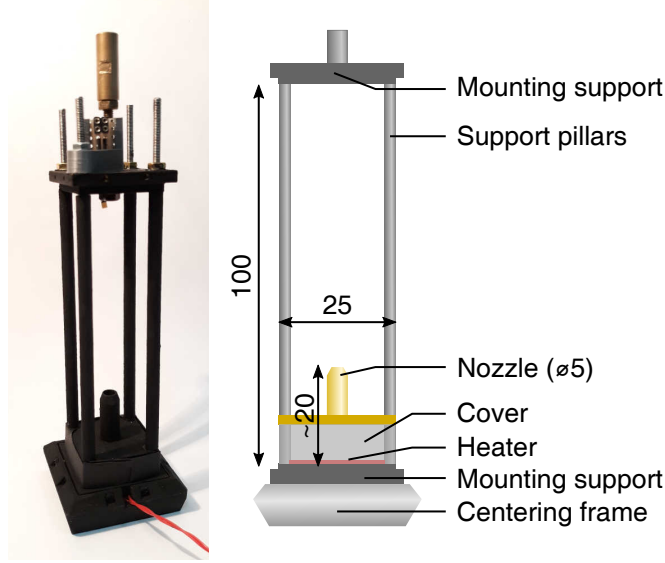
Figure 5.1: Photography (left) and scheme (right) of the experimental cell. Centering frame is 3D-printed from PLA, the remaining parts are made of brass. The parts are coated with black paint to reduce reflections of the laser light. Dimensions are given in millimeters.

LR0–LR5, that fully illustrate the underlying dynamics of all studied rings.[14] Individual data sets differ in temperature, the applied heat flux and the pulse duration, see Tab. 5.1 for experimental conditions. The obtained Reynolds numbers and aspect ratios indicate that all rings can be considered turbulent. We indeed observe that the rings are followed by visible wakes, consistently with literature.

Note that the values of the heat flux reported in Tab. 5.1 are obtained by dividing the power applied to the heater by the heater area, i.e., $(25.4\,\text{mm})^2$, because the heater is not tightly enclosed by the cover (see Fig. 5.1) and it is likely that some heat manages to escape to the surrounding bath, bypassing the much smaller nozzle.

To visualize the rings, we illuminate the particles, previously dispersed in the open volume above the nozzle, by a thin laser sheet that crosses the symmetry axis of the setup. Therefore, we only access the ring cross section, which appears as a pair of counter-rotating vortices. The vortices appreciably affect nearby particles: we commonly observe trajectories that are bent into loops, making the time-dependent position of the ring visible to a naked eye. Aiming for a quantitative analysis though, we make the rings visible to a computer thanks to a custom scalar parameter called Lagrangian pseudovorticity [134], proved to be suitable for the visualization of large vortices in the Lagrangian framework. Pseudovorticity is defined as

$$\theta(\boldsymbol{x}, t) = \left\langle \frac{[(\boldsymbol{x}_i - \boldsymbol{x}) \times \boldsymbol{u}_i]_z}{|\boldsymbol{x}_i - \boldsymbol{x}|^2} \right\rangle_i. \tag{5.4}$$

In the equation above, $\boldsymbol{x}$ and t denote position and time coordinates where θ is

---

[14]All 15 data sets are discussed in Ref. [124], attached to this work.

Table 5.1: Experimental conditions of the representative data sets. T: thermodynamic temperature; q: heat flux; t_{p}: pulse duration; v_{n}: normal fluid velocity at the nozzle exit, Eq. (1.4); L_{p}/D: aspect ratio, Eq. (5.3); $\mathrm{Re_r}$: ring Reynolds number, Eq. (5.1).

	T [K]	q [W/m^2]	t_{p} [ms]	v_{n} [mm/s]	L_{p}/D	$\mathrm{Re_r}/10^3$
LR0	1.50	2780	500	65.0	6.5	108.3
LR1	1.29	350	1000	23.0	4.7	22.9
LR2a	1.50	770	1000	18.0	3.6	16.6
LR2b	1.50	770	1000	18.0	3.6	16.6
LR3	1.75	4230	1000	35.9	7.1	70.8
LR4	1.75	3060	1000	26.0	5.2	37.0
LR5a	1.95	4120	1000	17.4	3.5	15.7
LR5b	1.95	4220	1000	17.8	3.6	16.6

calculated. Vectors $\boldsymbol{x}_i$ and $\boldsymbol{u}_i$ represent the position and velocity of the ith particle.[15] Subscript z indicates the only non-zero component of the vector product, since both its factors are effectively two-dimensional vectors. Ensemble averaging, indicated by the angle brackets, is performed over all particles that fall into the inspection area sketched in Fig. 5.2. It consists of an annulus with 1 mm inner and 5 mm outer radii, centred in $\boldsymbol{x}$. Annular geometry is intentionally chosen to eliminate diverging contributions of the particles that are located too close to the inspection point. The size of the inspection area approximately matches that of the observed vortices. Averaging is carried out also in the time domain, where we employ a 10 ms wide sliding window, centred in t.

Choice of the inspection area size and shape results from the systematic search for an optimal parametrization. In particular, we investigated how the mean signal, i.e., $\langle\theta^2\rangle_{\boldsymbol{x},t}$, depends on the outer inspection radius. We found that we obtain the maximum signal for a 10 mm radius, which correlates with the size of the vortex pair. The final (outer) radius of the inspection area was then taken as the half of this value, in order to optimize it for individual (clockwise and counter-clockwise) vortices.

Analytical relation between θ and Eulerian vorticity $\boldsymbol{\omega} = \nabla \times \boldsymbol{u}$ can be found for an idealized case of homogeneously distributed tracers that follow a smooth velocity field. It follows that pseudovorticity is equal to the half of vorticity in the vicinity of the inspection point.[16] However, the assumptions leading to this straightforward relation are not usually met in experiments. For instance, deuterium particles are usually inhomogeneously distributed in the camera FOV and they only rarely sample the vortex cores. Nevertheless, we can say that θ is, in the realistic case, at least a qualitative measure of the actual flow vorticity.

In order to find how the pseudovorticity is distributed in space we compute θ on

---

[15]We calculate the particle velocity by convolving its position with the Gaussian velocity estimator, described in §2.1.

[16]For derivation see §2.1 of Ref. [124], attached to this work.
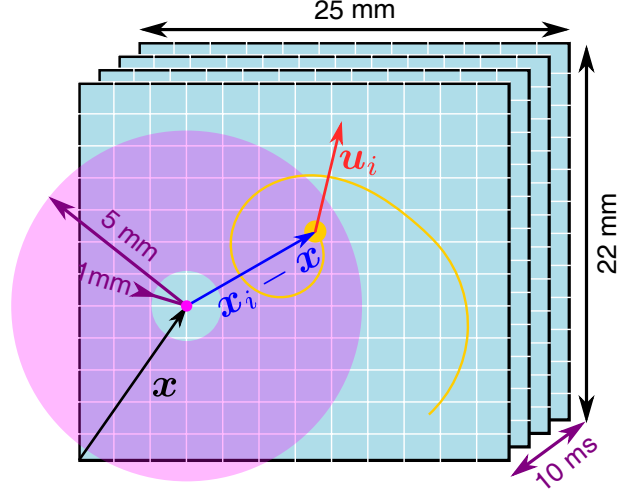
Figure 5.2: Calculation of the Lagrangian pseudovorticity θ. For each mesh point (purple point) we calculate the normalized vector product of the position (blue) and velocity vectors (red) for all particles (yellow point) that fall into the inspection area (purple area), defined as an annulus in space coordinates and as a sliding window in time. The resulting pseudovorticity is obtained as the averaged contribution of individual particles.

a regular mesh that consists of 115×101 inspection points, fully covering the camera field of view. This way, we obtain quasi-Eulerian, time-dependent maps of pseudovorticity (θ-maps). Realizations of the rings that fall into the same data set are found to produce comparable θ-maps, which allows us to merge them by extending the ensemble averaging in Eq. (5.4) over multiple acquired movies. This step leads to the data sets that contain more than 1 million positions each; the increased particle concentration in the field of view then reduces the background noise. A typical example of the resulting averaged θ-map obtained with the data set LR0 is displayed in the left panel of Fig. 5.3. Note that areas of positive and negative pseudovorticity representing the vortex pair can be easily distinguished in the figure.

We typically observe that the vortex pair first emerges from the background signal near the bottom end of the field of view. Subsequently, the vortices become more apparent and propagate towards the top end, where they eventually disappear. Their upwards journey can be precisely tracked by separating the vortices from the background signal. We achieve this by setting a positive threshold θ_0, ranging from $0.15\,\mathrm{s}^{-1}$ to $0.25\,\mathrm{s}^{-1}$ in the present experiment. Inspection points are filtered and only those meeting $|\theta| > \theta_0$ are kept. We then typically obtain two separate regions that represent the clockwise ($\theta > 0$) and counter-clockwise ($\theta < 0$) vortices, respectively, see the right panel of Fig. 5.3. Vortex positions, $\boldsymbol{p}_+$ and $\boldsymbol{p}_-$ are calculated as the $|\theta|$-weighted averages of the filtered inspection points. Reconstructed trajectories of the vortices are plotted by red lines in the right panel of Fig. 5.3.

Position of the entire ring $\boldsymbol{p}$ is defined as the joint $|\theta|$-weighted position of the two vortices. Cartesian components of $\boldsymbol{p}$ are plotted as the function of time in
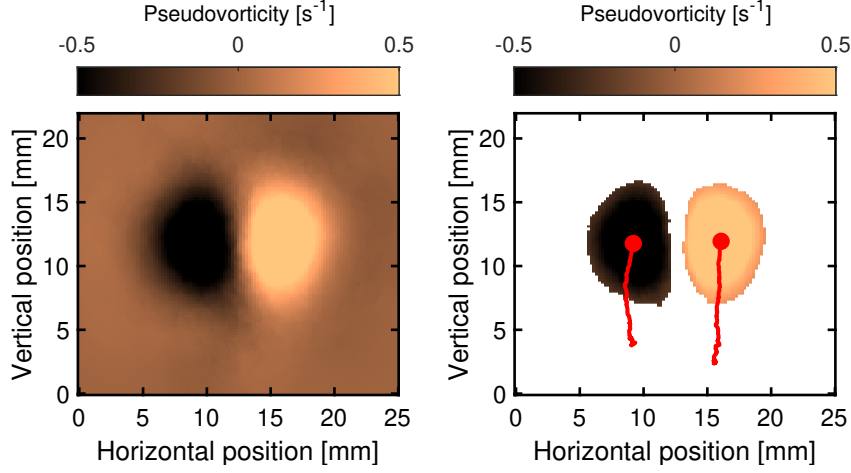
Figure 5.3: *Left panel:* map of pseudovorticity θ obtained $1.15\,\text{s}$ after the heat pulse. Data from the data set LR0. Tip of the nozzle is located $11\,\text{mm}$ below the bottom edge of the map. *Right panel:* pair of counter-rotating vortices can be isolated by setting the threshold $\theta_0 = 0.25\,\text{s}^{-1}$ (see the main text for details). Red points: respective positions of the vortex pair. Red lines: trajectories reconstructed from the previous θ-maps.

the left panel of Fig. 5.4 for the same data set LR0. Note that the horizontal position component remains constant in time and the vertical one systematically increases, indicating that the rings propagate vertically, as expected. Deviations can be seen at the beginning and at the end of the investigated time interval. Such spurious data usually originate from the relatively small number of filtered inspection points and they usually correspond to a weak signal-to-noise ratio. Interval when the vortex area (i.e., the number of considered inspection points) is at least $30\,\%$ of its maximum is marked by black dotted lines.

Ring velocity is obtained by differentiation of $\boldsymbol{p}$ with respect to time. This is achieved by the convolution with the Gaussian velocity estimator, Eq. (2.11), see the middle panel of Fig. 5.4. Note that the vertical velocity component is systematically non-zero and varies between ca. $5\,\text{mm/s}$ and $30\,\text{mm/s}$ in the present case. Apparent velocity decrease occurs for late times, which suggests that the ring has a tendency to slow down. Ring radius, displayed in the right panel of Fig. 5.4, is defined as $r_\text{r} = |\boldsymbol{p}_+ - \boldsymbol{p}_-|/2$ according to [135]. Note that r_r increases in time, which is consistent with the behaviour of classical vortex rings [136] as well as mechanically generated rings in He II [127].

Decrease of the ring velocity and increase of its size in time is observed also for other data sets. Note that this behaviour is typical for the rings that propagate in classical fluids [136] and can be explained by energy losses due to turbulent entrainment and viscous dissipation. Instead, the quantized vortex loops tend to shrink and accelerate [122] as they loose their energy via the interaction with the normal fluid. This fundamental difference between small and large-scale vortex rings coexisting in the same fluid is remarkable. It exists due to the circulation, which is constrained exactly to κ for the quantized loops, while for large vortex rings it is a continuous quantity, which tends to slowly decrease in time [135].
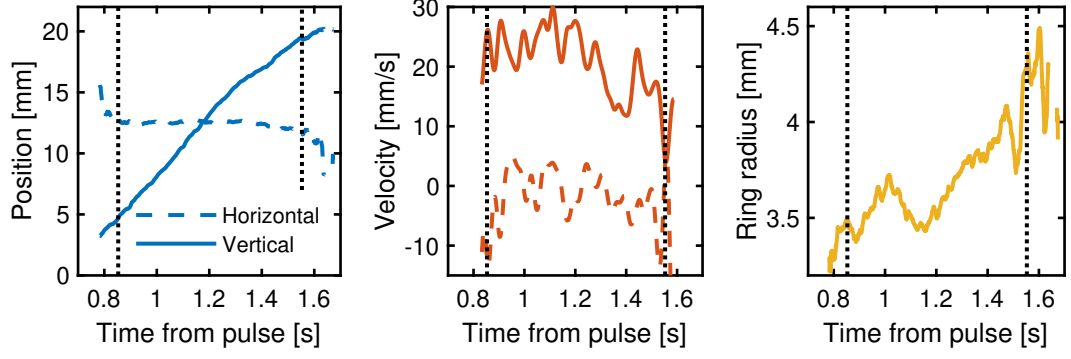
Figure 5.4: Tracking of the vortex ring. *Left panel:* ring position. *Middle panel:* ring velocity. *Right panel:* ring radius. Black dotted lines: interval where the vortex area is at least 30 % of its maximum value. Data from the data set LR0.

We have not yet mentioned that the experimental cell used to generate the rings is attached to a mobile shaft, which allows us to vertically displace the nozzle with respect to the camera position, in order to study vortex rings in a wider range of nozzle distances than the camera FOV. Notable reproducibility of the ring dynamics is demonstrated in Fig. 5.5, where we plot pairs of ring trajectories obtained under similar conditions (see Tab. 5.1), but at different distances from the nozzle. Neat overlap of the trajectories suggests that the rings can be precisely tracked for distances up to 30 mm ($6D$), in the current experimental set up.
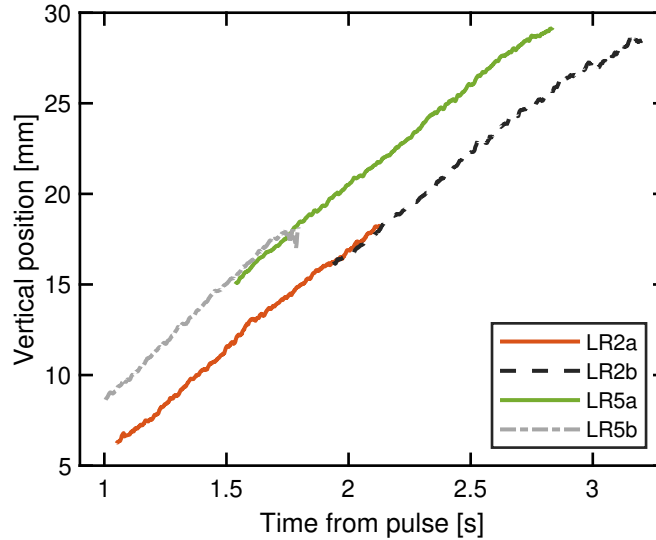
Figure 5.5: Demonstration of the highly reproducible ring dynamics. Trajectories obtained at different positions of the camera FOV neatly overlap, which indicates that the ring dynamics is well defined up to 30 mm ($6D$) away from the nozzle. Displayed positions correspond to the vortex areas that cover at least 30 % of their maximum values.

5.3 Classical scaling laws

The idea of quasi-classical dynamics of macroscopic vortex rings in He II can be elaborated further. In particular, we aim to check if the similarity theory, developed for turbulent vortex rings propagating in a classical fluid [123], can be applied to our data. The theory describes the rings as self-similar objects, whose dynamics is governed only by two dimensional parameters, the fluid density and the hydrodynamic impulse; viscous dissipation can be neglected for turbulent rings [123]. If the fluid is Newtonian and the interactions with the flow boundaries are neglected, both parameters are constant in time. These assumptions allow us to construct the corresponding stream function and it follows from its dimensional analysis that

$$r_{\mathrm{r}} \sim (y_{\mathrm{r}} - y_0), \tag{5.5}$$

$$(y_{\mathrm{r}} - y_0)^4 \sim (t - t_0), \tag{5.6}$$

where r_{r}, y_{r} is the ring radius and its vertical position, respectively. Virtual space and time origins, denoted as y_0 and t_0, vary with individual ring realizations and can be found experimentally.

Our data follow both these rules. We show it by plotting the representative data sets and their linear fits in Fig. 5.6. In this figure, we already subtracted virtual origins y_0 and t_0 from the data so that individual dependencies pass through the plot origins for clarity. We can say that the linear scaling of the ring radius (left panel) is somehow less clear than that of its vertical position (right panel). This suggests that θ-maps are performing well mainly for tracking the ring position, while the estimate of the ring size is considerably noisy, at least in the investigated parameter range.
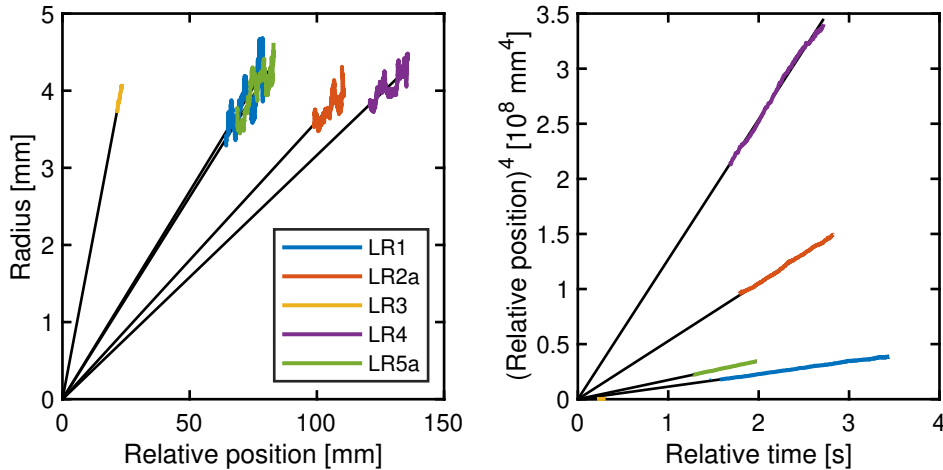
Figure 5.6: Verification of the scaling rules predicted by the similarity theory of turbulent vortex rings. *Left panel:* ring radius r_{r} as the function of the vertical position $y_{\mathrm{r}} - y_0$, Eq. (5.5). *Right panel:* power-raised position $(y_{\mathrm{r}} - y_0)^4$ as the function of time $t - t_0$, Eq. (5.6). Black lines: corresponding linear fits previously used to determine virtual origins y_0 and t_0 and adequately shifted in this figure.

The ring propagation velocity, v_{r} is expected to scale with time and distance as

well. These dependencies can be expressed in terms of time-independent constants c_t, c_y and c_r [135], defined as

$$c_t = v_r^{4/3}\left(t - t_0\right), \tag{5.7}$$

$$c_y = v_r^{1/3}\left(y_r - y_0\right), \tag{5.8}$$

$$c_r = v_r^{1/3}r_r. \tag{5.9}$$

Our data verify these equations. Specifically, we observe that the values of c_t, c_y and c_r fluctuate[17] around their mean values, which differ among individual realizations, as displayed in Tab. 5.2. This outcome is consistent with the similarity theory, which predicts that only the ratios c_y/c_t and c_r/c_t are universal. We verify this by plotting c_y and c_r as the function of c_t in Fig. 5.7, for all available data sets. Neat linear scaling in the left panel (blue points) is in excellent agreement with the predicted slope $c_y/c_t = 4$ (black dashed line). However, the relation between c_r and c_t (red squares in the right panel) is not systematic.

Table 5.2: Time-independent constants obtained from the similarity theory, Eqs. (5.7) – (5.9). Reported are the mean values and standard deviations.

	c_y [mm$^{4/3}$s$^{-1/3}$]	c_t [mm$^{4/3}$s$^{-1/3}$]	c_r [mm$^{4/3}$s$^{-1/3}$]
LR1	274.9 ± 18.7	69.9 ± 17.5	7.6 ± 0.6
LR2a	174.1 ± 12.1	42.8 ± 11.9	8.5 ± 0.5
LR3	194.4 ± 10.0	47.5 ± 9.9	11.0 ± 0.5
LR4	369.3 ± 18.9	90.2 ± 17.8	10.0 ± 0.6
LR5a	169.5 ± 10.6	43.2 ± 11.0	8.9 ± 0.6
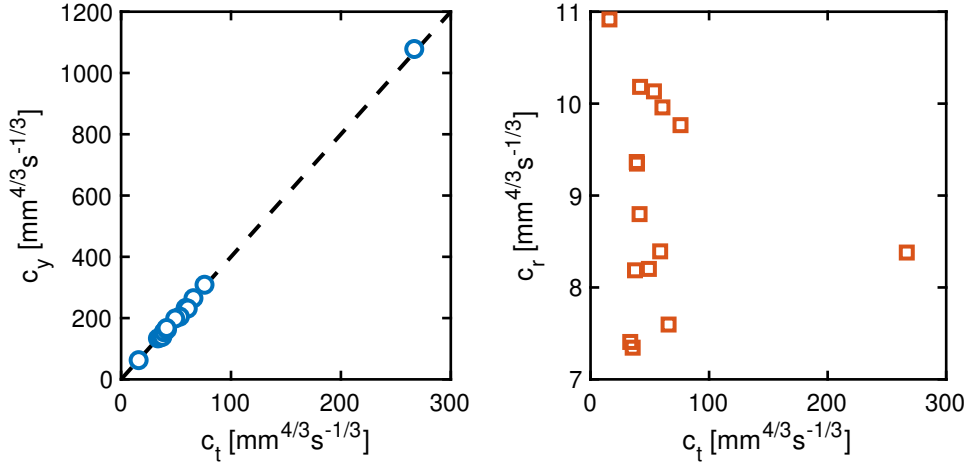
Figure 5.7: *Left panel:* c_y as the function of c_t (blue points). Black dashed line: predicted $c_y/c_t = 4$ slope. *Right panel:* c_r as the function of c_t (red squares). Note that data from all available data sets is plotted.

Consistency between the theory and experiment implies that our vortex rings move as they were moving in a classical fluid. Moreover, this outcome highlights the usefulness of the Largangian pseudovorticity and the underlying tracking

---

[17]Fluctuations are found to be normally distributed.

scheme developed. On the other hand, the missing universality of the ratio c_r/c_t (right panel of Fig. 5.7) points out that the ring radius is not correctly estimated by the outlined tracking scheme. Other, say, physical reasons for such behaviour are not clear at the moment.

5.4   Second sound study

The second sound attenuation and the flow visualization techniques are combined to investigate the vortex rings generated in He II in the cell shown in Fig. 5.8. Similarly to the previous experiment, the rings gain their energy from brief power pulses, supplied to a resistive heater enclosed in the pyramidal box already introduced in §4.2, and open to the surrounding bath via a circular nozzle of $D = 2\,\text{mm}$ diameter. The cell features an open volume above the nozzle that is $50\,\text{mm}$ high and can be seeded with solid particles. Custom-made second sound channel is located above this open volume and its detailed description can be found in §2.2. Two second sound transducers are located at a distance $d = (68.5 \pm 1)$ mm from the nozzle. Reported are results obtained at two temperatures, $1.66\,\text{K}$ and $1.51\,\text{K}$, which correspond to the normal fluid fractions, f_n equal to ca. $20\,\%$ and $12\,\%$, respectively.
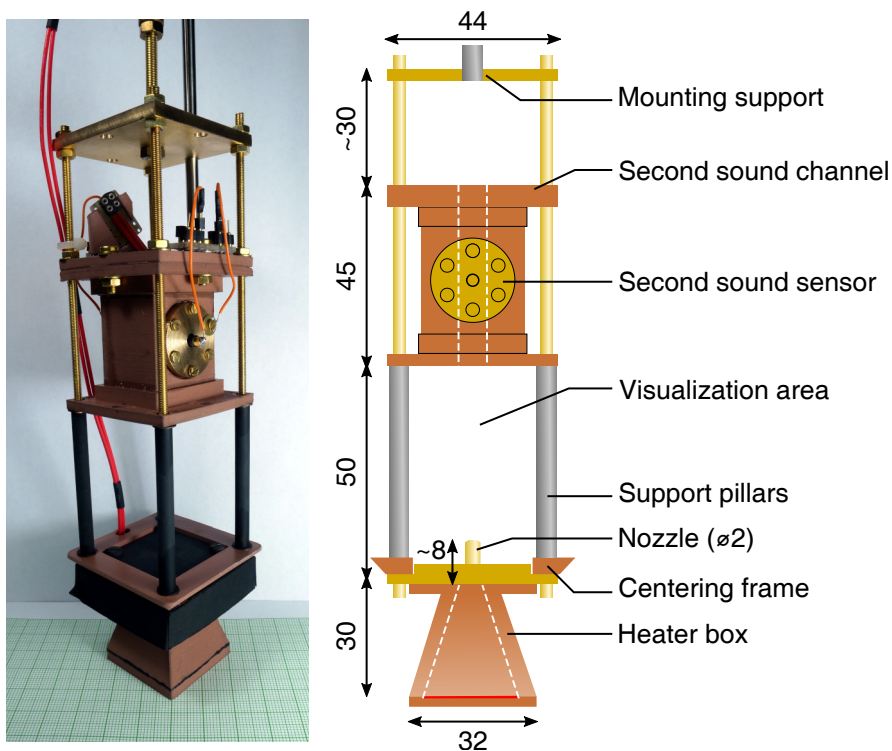
Figure 5.8: Photography (left) and scheme (right) of the experimental cell. The heater box, the centering frame and the second sound channel are 3D-printed from Cu-filled PLA, remaining parts are made of brass. The nozzle and the support pillars are coated with black paint. Dimensions are in millimeters. White dashed lines indicate the inner walls of the heater box and the second sound channel.

Resonant second sound wave is continuously excited in the channel by applying a sine wave with 7 V RMS amplitude to one of the sensors. Fine-tuning of its frequency is controlled by a PID loop, ensuring that the resonant condition is always met. For VLD measurements we take the 4$^{\text{th}}$ harmonic mode that occurs in the present channel near 3610 Hz at 1.66 K and 3545 Hz at 1.51 K. In-phase and quadrature components of the transmitted signal are read from the second sensor at ca. 15 Hz sampling rate.

Power pulses (up to 0.7 W of the heating power and 1500 ms duration) are programmatically supplied to the heater. We check the shape of the pulses by measuring the corresponding current and voltage by a pair of synchronized multimeters with 250 Hz sampling rate. Obtained data confirm that the pulses are orthogonal, and we use them for the precise timing of the experiment (the instant when the pulse starts is taken for the time origin of the second sound data). More than a thousand ring realizations were acquired and split into multiple data sets, summarized in Tab. 5.3.

Heat flux used to compute the ring Reynolds number and the aspect ratio is calculated by dividing the pulse power with the heater area, consistently to §5.2. It is clear from the scheme in Fig. 5.8 that the heater area is significantly larger than the nozzle cross section. Values reported in Tab. 5.3 should be then regarded as their conservative estimates. All observed rings appear turbulent, since the wakes are clearly formed behind them. Occurrence of these wakes suggests that the actual values of $\mathrm{Re_r}$ and L_p/D are larger than what we report in Tab. 5.3, indicating that the deposited heat effectively spreads over a smaller area than the heater cross section.

On the other hand, if we consider for this area solely the nozzle cross section—$\pi \left(D/2 \right)^2 = 3.1 \, \mathrm{mm}^2$, roughly 200-times smaller than the heater area—we obtain an unrealistic increase of $\mathrm{Re_r}$ by 4 orders of magnitude and that of L_p/D by 2 orders of magnitude. The use of this area also results in the calculated normal fluid velocity of the order of 1 m/s inside the nozzle.

A more adequate physical picture arises if we assume that the flow inside the heater box is not isothermal similarly to the case of the counterflow jets and consistent with the reported temperature gradients in turbulent counterflow [90, 113]. If we take into account that the heater box contains approximately 10 cm^3 of He II, adiabatic addition of 1 J of heat at 1.66 K would increase the temperature inside the box by ca. 0.3 K. This in turn leads to the decrease of v_n, see Eq. (1.4), $\mathrm{Re_r}$ and L_p/D. Additionally, a further decrease of v_n inside the nozzle is possible due to heat leaks through the joints between the brass nozzle and plastic walls of the heater box, similarly to our discussion in §4.2.

Again, a realistic order-of-magnitude estimate of v_n can be obtained from visualization. At 1.66 K, we observe that the particle velocity above the nozzle is of the order of 100 mm/s (see, e.g., Fig. 5.13 below, where this velocity is estimated to ca. 83 mm/s). Following this observation, we can say that realistic values of $\mathrm{Re_r}$ are about 100-times larger and those of L_p/D are about 10-times larger than what is reported in Tab. 5.3.

Table 5.3: Experimental conditions of the acquired data sets. T: thermodynamic temperature; f_n: normal fluid fraction; N_r: number of ring realizations in the data set; P: applied power; t_p: heat pulse duration; $Q = Pt_p$: dissipated heat; L_p/D: aspect ratio, Eq. (5.3); Re_r: ring Reynolds number, Eq. (5.1). Superscripts denote the availability of visualization data.

	N_r	P [mW]	t_p [ms]	Q [J]	L_p/D	$\mathrm{Re}_r/10^3$
			$T = 1.66\,\mathrm{K}$, $f_n = 0.20$			
RA1*†	40	242	519 ± 6	0.13	1.3	1.4
RA2*†	50	242	821 ± 9	0.20	2.0	2.2
RA3	39	242	1518 ± 10	0.37	3.7	4.0
RA4*†	50	483	321 ± 9	0.16	1.5	3.3
RA5*†	50	483	520 ± 9	0.25	2.5	5.4
RA6*†	50	483	818 ± 8	0.40	3.9	8.5
RA7	45	483	1520 ± 8	0.73	7.3	15.8
RA8*	50	675	223 ± 9	0.15	1.5	4.5
RA9*	35	675	321 ± 7	0.22	2.2	6.5
RA10*†	30	675	523 ± 8	0.35	3.5	10.6
RA11*†	30	675	819 ± 10	0.55	5.5	16.7
			$T = 1.51\,\mathrm{K}$, $f_n = 0.12$			
RB1	50	96	522 ± 10	0.05	0.9	0.7
RB2	50	97	1522 ± 9	0.15	2.8	2.2
RB3	50	240	219 ± 11	0.05	1.0	1.9
RB4	50	240	319 ± 7	0.08	1.4	2.8
RB5	30	240	520 ± 7	0.12	2.3	4.5
RB6	30	240	818 ± 7	0.20	3.7	7.1
RB7	30	240	1520 ± 7	0.36	6.8	13.2
RB8	7	481	117 ± 17	0.06	1.0	4.1
RB9	38	481	220 ± 10	0.11	2.0	7.7
RB10	50	481	321 ± 7	0.15	2.9	11.2
RB11	30	481	519 ± 5	0.25	4.7	18.0
RB12	30	481	820 ± 10	0.39	7.3	28.5
RB13	30	481	1521 ± 11	0.73	13.6	52.9
RB14	50	672	221 ± 11	0.15	2.8	15.0
RB15	50	672	321 ± 9	0.22	4.0	21.8
RB16	30	672	522 ± 9	0.35	6.5	35.4
RB17	30	672	821 ± 9	0.55	10.3	55.7

* Visualization data available 9.3 mm above the nozzle.
† Visualization data available 24.3 mm above the nozzle.

Vortex line density

The current understanding of large vortex rings in He II [129] indicates that a localized vortex tangle propagates alongside the normal-fluid ring, so that both helium components display equal circulation. Presence of the vortex tangle is

detected by the second sound as the decrease of its amplitude. Since the tangle is localized and moves with respect to the second sound sensor, the measured sound amplitude changes in time. In particular, we see that it abruptly decreases at first (this corresponds to the arrival of the ring between the sensors) and then slowly recovers (this reflects a non-zero vorticity present in the wake). The second sound response is found to be highly reproducible and we can average multiple ring realizations into a single response curve. This is achieved by the synchronization of individual signals with respect to the heat pulse start and by their subsequent averaging within adjacent 70 ms time windows. A typical example of the resulting second sound amplitude is displayed as the function of time in the left panel of Fig. 5.9 (red line), alongside with the corresponding heat pulse (black line).
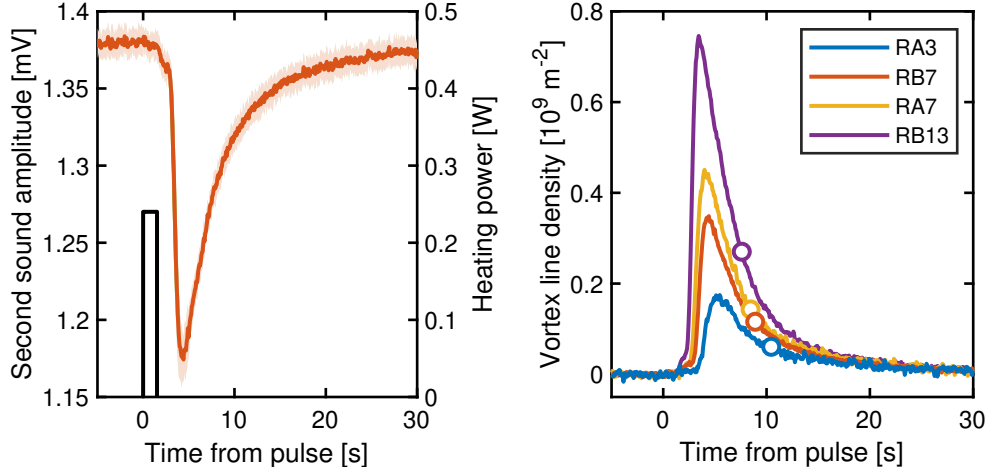
Figure 5.9: *Left panel:* typical second sound response to a vortex ring that propagates along the second sound channel. Data from the data set RB7. Red line: averaged signal from 30 realizations. Pale red area: one standard deviation interval. Black line, right axis: the mean heat pulse. *Right panel:* examples of the calculated VLD profiles. Open points: characteristic time t_{B}, Eq. (5.10).

Time-dependent vortex line density $L(t)$ is computed from the averaged second sound amplitude by employing Eq. (2.15). Unattenuated amplitude A_0 is calculated as the mean value of the first 50 points from each response curve and the resonance width Δ_0 is taken from full frequency sweeps, regularly acquired in quiescent He II during the experiment. The resulting vortex line density profiles can be considered as central outcomes of the second sound setup and four representative cases are plotted in the right panel of Fig. 5.9.

Note that individual $L(t)$ profiles appear to share the same shape, which can be verified by finding an adequate set of normalization parameters. Natural candidates for these parameters are the peak amplitude $L_{\mathrm{m}} = \max{[L(t)]}$ and the corresponding arrival time t_{m} (defined as $L(t_{\mathrm{m}}) = L_{\mathrm{m}}$). We can also calculate the profile area $L_I = \int L(t)\,\mathrm{d}t$ and the characteristic time t_{B}, defined as

$$t_{\mathrm{B}} = \sum_t tL(t) \bigg/ \sum_t L(t) \,. \tag{5.10}$$

This time can be understood as the centroid of the profile and its estimate is more robust against the experimental noise than t_{m}. It turns out that this is

71

particularly useful because t_B and t_m are linearly correlated, see the left panel of Fig. 5.10. In other words, t_B can be employed as the characteristic time scale of the VLD profiles. Similarly, L_I is less affected by the noise compared to L_m because L_I is an integral quantity. Linear scaling between these parameters is observed as well, see the right panel of Fig. 5.10. Slight departure from the linear scaling is apparent only for relatively weak rings ($L_I \leq 10^9\,\mathrm{s/m^2}$), which can be attributed to low signal-to-noise ratios of these profiles.
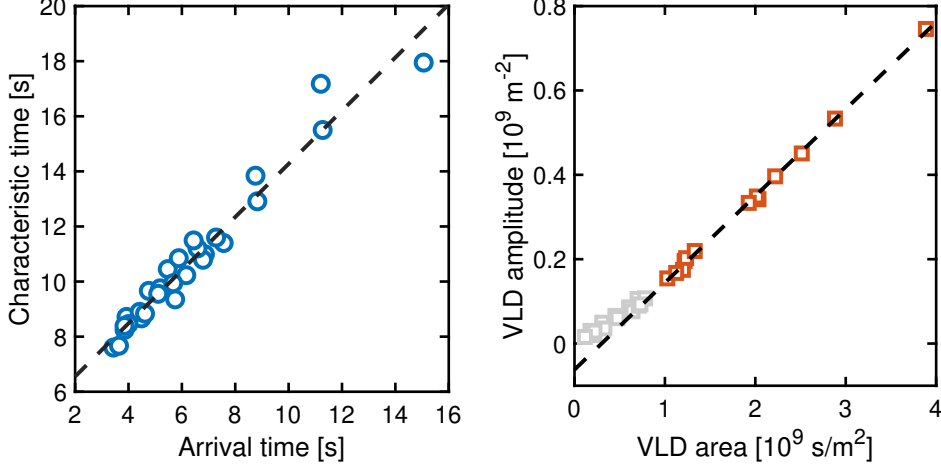
Figure 5.10: *Left panel:* linear scaling of t_B with t_m. Points: experimental data. Dashed line: linear fit. *Right panel:* linear scaling of L_m with L_I. Squares: experimental data. Dashed line: linear fit of points that meet $L_I > 10^9\,\mathrm{s/m^2}$ (these points are highlighted by red colour).

Normalization of the VLD profiles aims to remove the dependence on the specific ring realization. This can be achieved by non-dimensionalization of both coordinates. Specifically, we normalize time by t_B and the vortex line density by L_I/t_B. The obtained non-dimensional profiles $L'(t')$ are of unit area and neatly overlap; we show this by small grey points in Fig. 5.11.

Ensemble average of dimensionless profiles (blue line in Fig. 5.11) reflects only the geometric features of the flow structure that consists of the vortex ring and its wake. Sharp peak at the beginning corresponds to a dense vortex tangle constituting the vortex ring; turbulent wake can be associated with the following gradual decrease of L'. Since the rings move with a velocity of the order of $10\,\mathrm{mm/s}$ and a non-zero vortex line density is observed typically for $20\,\mathrm{s}$ past the arrival time, the measured signals correspond to a flow structure that is roughly $20\,\mathrm{cm}$ ($100D$) long.

Non-dimensional profile can be fitted with the following function:

$$L'(t') = p_a H\left(t' - p_b\right)\left(t' + 1 - p_b\right)^{p_c} * G\left(p_\sigma\right), \tag{5.11}$$

where four parameters p_a, p_b, p_c and p_σ are free, H denotes the Heaviside step function and $G(p_\sigma)$ is the Gaussian blur kernel with the standard deviation p_σ that accounts for the finite size of the second sound sensors. Eq. (5.11) simply reflects the observed behaviour of the dimensionless profile: the model function is first zero, then sharply rises at $t' = p_b$ and decays with the power-law exponent p_c.

Levenberg-Marquardt fit of Eq. (5.11) yields $p_a = 2.15$, $p_b = 0.39$ and $p_c = -2.98$ for the fixed $p_\sigma = 0.07$ in non-dimensional units. The resulting function, plotted as the red line in Fig. 5.11, displays an excellent agreement with the experimental data.
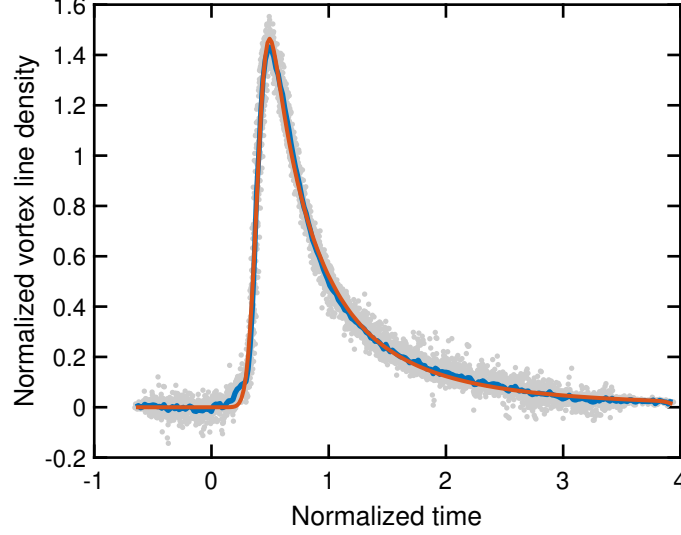
Figure 5.11: Normalized profile of the vortex line density. Time is normalized by t_B, the vortex line density is normalized by L_I/t_B. Grey points: overlapping experimental data (only data sets that meet $L_I > 10^9\,\mathrm{s/m^2}$ are displayed). Blue line: ensemble average of the experimental data. Red line: fit of Eq. (5.11).

The width of the blur kernel was set manually, in order to improve the fit; we can however argue that its (dimensional) value, $0.07t_B$ is physically sound. If we assume that the ring velocity can be estimated as d/t_m, where $d = 68\,\mathrm{mm}$ is the distance between the nozzle and the sensor pair (we discuss the ring velocity in more detail below), we obtain that the spatial analogue of the kernel width is $0.07dt_B/t_m$. If we consider that $t_B/t_m \approx 1$ (the slope of the linear fit displayed in the left panel of Fig. 5.10 is ca. 0.97), we find that the spatial extent of the kernel is $0.07d \approx 5\,\mathrm{mm}$, which is comparable to the radius of the second sound sensors ($4\,\mathrm{mm}$).

We can now compare p_σ with the (normalized) time needed for L' to reach its maximum value from zero; the latter is smaller than p_b and we estimate it from Fig. 5.11 as $t'_{\mathrm{sig}} \approx 0.2$, by subtracting the latest time when L' is practically zero from the time when L' peaks to the maximum value. Roughly speaking, $t'_{\mathrm{sig}} \approx 3p_\sigma$, which hints that the vertical size of the dense vortex tangle that propagates through the channel is ca. $15\,\mathrm{mm}$.

Moreover, we can also estimate the expected radius of the ring inside the second sound channel from the similarity theory developed for classical turbulent rings [136] (see below). We obtain $D + 0.01d = 2.68\,\mathrm{mm}$, where we take the initial nozzle radius equal to D and we let it expand over the distance d according to the growth rate reported in Ref. [136].

Perhaps the most interesting outcome of the fit is that the vortex line density in the wake decays with the power-law exponent $p_c \approx -3$. Interpretation of this

outcome is, however, not straightforward, because of the lack of a linear (Galilean) transformation between the laboratory and ring frames of reference. As we will show below, the ring velocity is not constant in time and the corresponding transformation is hence non-linear.

Control parameters

Control parameters, summarized in Tab. 5.3, are expected to tune the resulting velocity and strength of the vortex rings. We aim to estimate these characteristics from the second sound response and check whether and how they depend on the relevant control parameters.

For instance, we can calculate the average ring velocity $\langle v_r \rangle$ based on the arrival time t_m and the distance d separating the sensors from the nozzle, as

$$\langle v_r \rangle = \frac{d}{t_m}. \tag{5.12}$$

However, the instantaneous velocity, v_r is not constant. It likely decreases in time (or with the travelled distance) because turbulent rings tend to loose their kinetic energy into the wake [136]. Following the similarity theory introduced in Ref. [136], the ring velocity depends on distance as

$$v_r(y) = v_0 \left(\frac{\alpha y}{r_0} + 1 \right)^{-(3+C_D)}, \tag{5.13}$$

where $\alpha = \mathrm{d}r_r / \mathrm{d}y \approx 0.01$ denotes the growth rate of the ring radius and C_D is the drag coefficient related to the entrainment of the surrounding fluid. Parameters v_0 and r_0 indicate the initial ring velocity and radius, respectively. They correspond to the point where the vortex ring is fully formed and the concept of similarity becomes applicable. This point is also taken for the origin of t and y. Note that Eq. (5.13) results in the same asymptotic behaviour as Eqs. (5.5) and (5.6) if $C_D \ll 1$. We also note that the ring formation process limits the applicability of this theory to distances larger than ca. 15 nozzle diameters [136].

For the sake of argument, let us here neglect the formation process and assume that the ring follows Eq. (5.13) right after the heat pulse, just above the nozzle. By integrating $v_r(y)$ we obtain for the travelled distance

$$y = \frac{r_0}{\alpha} \left\{ \left[\frac{\alpha v_0 \left(4 + C_D \right) t}{r_0} + 1 \right]^{1/(4+C_D)} - 1 \right\}. \tag{5.14}$$

This equation is also valid for time t_m and position d. We can then express v_0 as

$$v_0 = \frac{r_0}{(4 + C_D) \alpha t_m} \left[\left(\frac{\alpha d}{r_0} + 1 \right)^{4+C_D} - 1 \right]. \tag{5.15}$$

Now, if we assume that $2r_0 \approx D$ and α and C_D are constant for all rings, we find that v_0 depends only on t_m ($v_0 \sim t_m^{-1}$). By comparing Eqs. (5.12) and (5.15) it

follows that $\langle v_r \rangle$ is, in fact, proportional to v_0 and their ratio is

$$\frac{v_0}{\langle v_r \rangle} \approx \frac{D}{2\left(4 + C_D\right)\alpha d}\left[\left(\frac{2\alpha d}{D} + 1\right)^{4+C_D} - 1\right] \approx 5.3, \qquad (5.16)$$

where we took for $\alpha = 0.01$ and $C_D = 2$, following the experimental results reported in [136]. Due to multiple simplifications considered above we should take this result with caution, but it nevertheless suggests that the mean ring velocity can be considered as a semi-quantitative estimate of v_0 and should be then recognized as a valid physical parameter.

Systematic dependence of $\langle v_r \rangle$ emerges if we plot it as the function of the heat dissipated during the power pulse, further rescaled by the normal-fluid fraction, i.e., Q/f_n, see the left panel of Fig. 5.12. Note that data obtained at two different temperatures (empty and full points) neatly overlap in this plot.

Although such outcome is intriguing, we need to keep in mind that the accuracy of $\langle v_r \rangle$ is affected by the ring formation process, which may vary between individual data sets. More experimental effort is required to clarify this behaviour and—more importantly—to provide its physical interpretation. Note that no clear dependence is apparent when we plot the same data as the function of the ring circulation, Γ_r, which is a relevant control parameter for the rings with thin cores [122]. We also note that Γ_r is proportional to $P^2 t_p$, while $Q = P t_p$.

The strength of the vortex rings can be quantified by L_I, the VLD profile area, which is found to scale linearly with the modified heat, see the right panel of Fig. 5.12. Data obtained at both temperatures collapse onto a single line within the full range of the applied Q values, which are limited by the maximum equal to ca. $0.75\,\mathrm{J}$. For greater values of Q we observe that the self-similarity of VLD profiles no longer holds, i.e., the profiles get deformed, which likely means that a jet-like structure forms past the nozzle instead of a localized vortex ring.
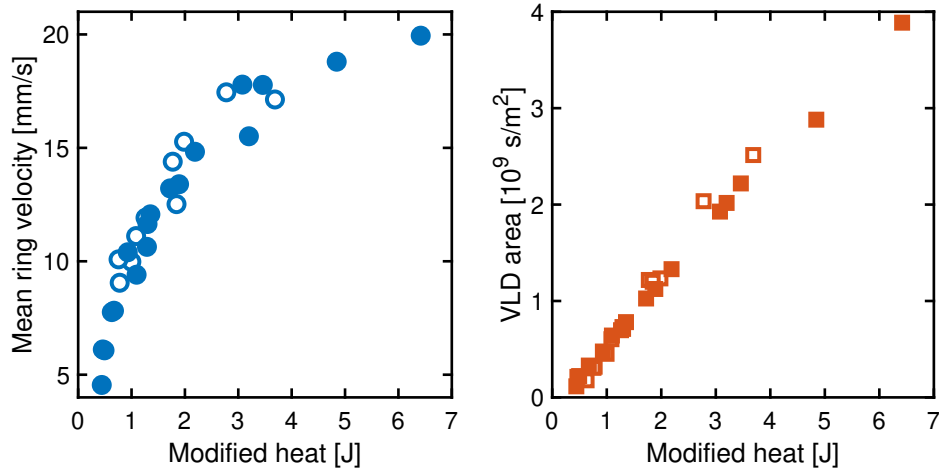
Figure 5.12: *Left panel:* mean ring velocity $\langle v_r \rangle$ as the function of the modified heat Q/f_n. *Right panel:* VLD profile area L_I as the function of the modified heat. Open symbols: data sets RA1–RA11 ($T = 1.66\,\mathrm{K}$). Filled symbols: data sets RB1–RB17 ($1.51\,\mathrm{K}$).

The already mentioned lack of a Galilean transformation between the laboratory

and ring frames of reference impedes a straightforward interpretation of $L(t)$. Finite size of the second sound sensors (their radius is $R_\mathrm{s} = 4\,\mathrm{mm}$) results in the measurement of a spatially averaged VLD. As the first-order estimate of this effect we can model the obtained values of $L(t)$ as

$$L(t) = \frac{1}{2R_\mathrm{s}} \int\limits_{-R_\mathrm{s}}^{R_\mathrm{s}} L\left[\xi + y(t)\right] \mathrm{d}\xi = \int\limits_{-\infty}^{\infty} S(\xi) \cdot L\left[\xi + y(t)\right] \mathrm{d}\xi = (L * S)\left[y(t)\right], \quad (5.17)$$

where we additionally assume that L is only a function of the axial distance y, whose time dependence is given by Eq. (5.14). The right-hand side of Eq. (5.17) denotes the convolution of VLD with the characteristic function of the sensor $S(\xi)$, which is here an orthogonal step function from $-R_\mathrm{s}$ to R_s with the functional value equal to $1/(2R_\mathrm{s})$ (its integral is equal to 1). Integral of $L(y)$ is finite and proportional to the total length of the vortex lines in the channel and integral of $L(t)$ approximately equals to L_I even if we extend the integration limits to infinity. Since all the functions are integrable, it follows from the Fubini theorem that the integral of a convolution can be split into the product of integrals, i.e.,

$$L_I \approx \int\limits_{-\infty}^{\infty} L(t)\,\mathrm{d}t = \int\limits_{-\infty}^{\infty} S(\xi)\,\mathrm{d}\xi \cdot \int\limits_{-\infty}^{\infty} L\left[y(t)\right]\mathrm{d}t. \quad (5.18)$$

Because the first integral on the right-hand side is equal to 1, L_I differs from the spatially-integrated vortex line density only by the non-linear transformation between t and y. In an idealized case when the ring velocity is constant and equal to, say, v_0, we would obtain that

$$L_I = \frac{1}{v_0} \int\limits_{-\infty}^{\infty} L(y)\,\mathrm{d}y. \quad (5.19)$$

Equations (5.18) and (5.19) provide the physical interpretation of L_I. Since the right-hand side is proportional to the total length of the vortex lines observed in the channel, L_I is a relevant measure of the vortex ring strength.

It then follows, for an identical heat pulse employed, that the ring generated at a lower temperature will move faster and display a larger peak of VLD than the ring produced at a higher temperature. Such behaviour is to some extent intuitive, if we consider that the normal component likely exits the nozzle with a higher velocity when the temperature decreases. However, the simple scaling of $\langle v_\mathrm{r} \rangle$ and L_I with the normal fluid fraction does not fully match the temperature scaling of v_n in thermal counterflow (Eq. 1.4) and one has to take into account the underlying ring formation mechanism. Do identical energy injections generate rings with the same initial velocity and strength, or is their formation temperature dependent? If not, do large vortex rings in He II loose their energy at different rates for different temperatures? We believe that additional experiments are needed to answer these questions and to clarify the outlined behaviour.

Complementary results of flow visualization

We employ solid deuterium particles to visualize the vortex rings in the open volume of the experimental cell from Fig. 5.8, under similar experimental con-

ditions and with the same control parameters as the selected data sets listed in Tab. 5.3. Cross sections of the vortex rings are captured in the field of view ca. 12.7 mm wide and 8 mm high, now located at two different distances, $d_1 = 9.3$ mm and $d_2 = 24.3$ mm, measured between the bottom edge of the camera FOV and the nozzle tip. In agreement with the previous work, the movies depict vortex pairs that propagate vertically in a well-defined and reproducible manner, which allows us to merge multiple ring realizations into large data sets prior to their analysis. In comparison to the visualization study reported in §5.2, the rings are now smaller (the nozzle diameter is 2 mm instead of 5 mm), move faster and their wakes are more prominent.

The acquired positions and velocities of the particles[18] are split into multidimensional bins. We resolve 50 bins according to their horizontal position and additional bins of 0.1 s width according to time (number of bins depends on the movie length). For each bin combination we calculate the average horizontal position x and the average vertical velocity $\langle u_y \rangle$ of the particles, to obtain the velocity profiles, i.e., $\langle u_y \rangle$ expressed as the function of x (particle dynamics along the FOV height is therefore averaged). Typical profiles are displayed in Fig. 5.13.
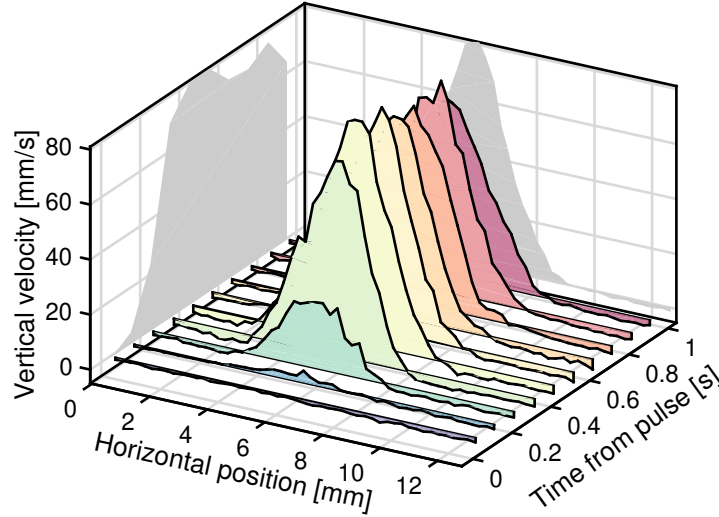

Figure 5.13: Typical velocity profiles. Data from the data set RA9 (Tab. 5.3, the field of view is located 9.3 mm away from the nozzle) are split into 50 horizontal position and 10 time bins. Grey shadows in the background: profile maximums in the given spatial and time dimensions.

Time evolution of the velocity profiles is similar for all data sets. At first, the profile is flat. Small negative values of $\langle u_y \rangle$ are compatible with the gravitational settling of deuterium particles. Relatively shortly after the heater is powered, we observe a small positive velocity in the middle. Afterwards, the profile quickly develops, i.e., we see that the particles move upwards in the full height of the camera field of view. Shape of the fully developed profiles is close to a single-peaked Gaussian. Constant peak position, combined with the apparent symmetry of the profiles, suggests that individual vortex rings propagate along similar trajectories.

---

[18]We calculate the particle velocity by convolving its position with the Gaussian velocity estimator, described in §2.1.

Constant width of the developed profiles additionally indicates that the size of the observed flow structure does not appreciably change between the data sets.

We can demonstrate these features explicitly by plotting the position of the peak velocity x_m, defined as $\langle u_y \rangle (x_m) = \max(\langle u_y \rangle)$, as the function of time, for all available data sets in a single plot, see the left panel of Fig. 5.14. Small blue and red points denote two locations of the field of view, and we see that the measured peak positions are roughly constant within these groups. A small relative difference between the two groups indicates a non-zero tilt of the ring trajectories (estimated to be ca. 4°), which likely originates from the slight misalignment of the experimental cell inside the cryostat. A somehow larger scatter of the ring positions in the more distant field of view can be linked to the occurrence of turbulent instabilities, which are typical for vortex rings obtained at large Re_r [135].
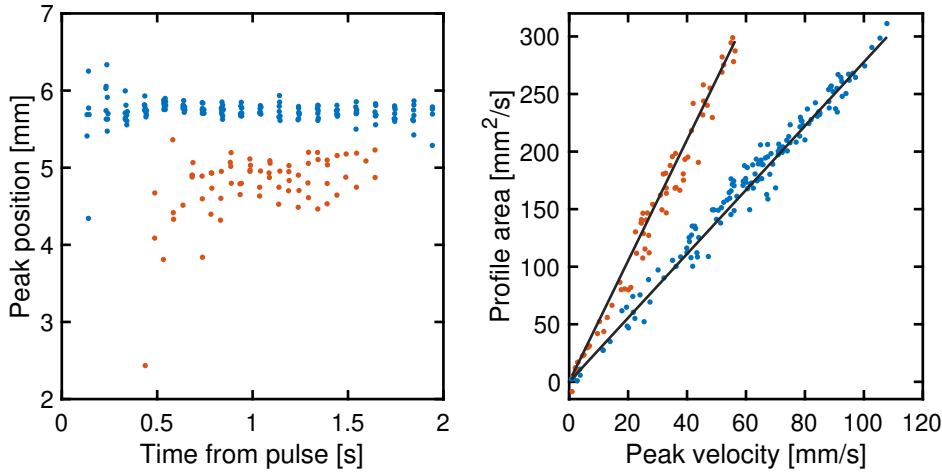
Figure 5.14: *Left panel:* position of the velocity peak x_m as the function of time. *Right panel:* linear scaling of the profile area as the function of the peak velocity. Blue (red) points: field of view located 9.3 mm (24.3 mm) away from the nozzle. Black lines: linear fits with zero intercept reveal the size of the observed ring–wake structure (see the main text).

Constant width of the profiles can be verified by direct fitting. However, we suggest an alternative approach. After having checked that some of the profiles are Gaussian-like, we numerically compute their areas and plot them as the function of the peak velocity, see the right panel of Fig. 5.14. Neat linear dependencies, obtained in both field of view locations, confirm the idea of a constant width. Because the area, A_g below a Gaussian peak with the amplitude a_g and standard deviation σ_g is equal to $A_g = \sqrt{2\pi} a_g \sigma_g$, the slopes of linear dependencies in the right panel of Fig. 5.14 are equal to $\sqrt{2\pi} \sigma_g$.

We can estimate the apparent radius of the ring–wake structure as $r_r = 2\sigma_g$, in the accordance with the two-sigma rule valid for Gaussian peaks. It seems that r_r does not depend on temperature nor the applied heat flux or the pulse duration. However, r_r clearly increases with the distance from the nozzle. For two locations of the field of view we obtain

$$r_{d1} = (2.21 \pm 0.03) \text{ mm},$$
$$r_{d2} = (4.19 \pm 0.08) \text{ mm}.$$

We note in passing that this effect is not directly visible from the individual velocity profiles, because they contain information that is averaged along the FOV height.

The corresponding growth rate can be estimated as

$$\frac{r_{\mathrm{d2}} - r_{\mathrm{d1}}}{d_2 - d_1} = 0.13 \pm 0.01.$$

This value is about 10-times larger than the growth rate $\alpha \approx 0.01$ reported for classical rings [123, 136], but comparable to the growth rate of the counterflow jets β, measured in §4. It hence seems that the current data reflect rather the turbulent wake than the vortex ring. It is likely that the actual ring radius is $r_{\mathrm{r}} \leq r_{\mathrm{d1}} \approx D$, which is consistent with the previous visualization study (see the left panel of Fig. 5.6).

We note in passing that both visualization experiments failed to reproduce the classical value of the ring growth rate, despite the motion of large rings in He II was found to be classical-like.[19] Eventual observation of the ring growth rate in He II compatible with α may strengthen the analogy between the superfluid and classical vortex rings, built in this work and in Ref. [124].

The access to a more detailed information, e.g., the ring propagation velocity, is limited with the currently available data. The latter can be approximately estimated from the time evolution of the velocity profiles, to be of the order of 10 mm/s, with no clear dependence on control parameters. In order to obtain more refined results, several technical challenges are needed to be overcome. For example, the potential use of the Lagrangian pseudovorticity requires a significantly larger density of tracer particles than that achieved in the current experiment, which are needed to be captured with a large enough camera frame rate, in a relatively small field of view. It would be hence easier to visualize larger rings that propagate more slowly, but such requirements compete with those imposed by the second sound attenuation technique. In particular, the size of the vortex rings is limited by the width of the second sound channel (10 mm sides). Moreover, the detection of spatially confined tangles of quantized vortices in smaller vortex rings is more sensitive than in larger ones, since dense tangles attenuate the second sound waves more efficiently than dilute ones.

We can nevertheless conclude that the simultaneous use of the flow visualization and the second sound attenuation techniques is possible. Preliminary data presented in this section can be considered as the proof-of-concept, as we showed that the combination of two distinct experimental techniques offers a useful tool for the complex characterization of large vortices that propagate in He II.

---

[19]The growth rates of the vortex rings displayed in the left panel of Fig. 5.6 are equal to the slopes of the respective linear fits.

Conclusions

Interactions between small solid particles and the quantized vortices were exploited in view to address physical phenomena that occur in the channel counterflow and are not yet fully understood. First, we studied the role of the heater, which doubles as a solid boundary and the flow generator. We devised a method for the qualitative estimation of the vortex line density, based on the scale-dependent velocity flatness. We found that the vortex tangle is appreciably denser in the area located immediately above the heater, compared to the bulk (Fig. 3.3). This outcome is robust and is verified by two types of particles that differ in density (solid D_2 and HD). Our observation provides experimental evidence that the vortex tangle develops inhomogeneity in thermal counterflow, in the direction of the heat flux. The findings are published as research articles (Refs. [61, 79]) and reproduced here as Attachments 1 and 2.

The ability of the particles to gain or lose their kinetic energy was investigated in quantum turbulence via longitudinal velocity increments. The classical phenomenon of flight-crash events, which is responsible for negatively skewed distributions of the increments, was not found in thermal counterflow of He II, for length scales both smaller and larger than the mean intervortex distance (Fig. 3.7). The observed difference is linked to the existence of non-classical energy transport mechanisms in quantum turbulence, which influence the motion of the flow-probing particles. Instead, for mechanically generated turbulence in He II, probed only at scales larger than the mean intervortex distance, the observed particle dynamics qualitatively corresponds to the classical result. In this case, the collective behaviour of the vortex tangle resembles the action of classical viscosity. A detailed discussion is provided in our own publication (Ref. [80]), which is reproduced here as Attachment 3.

Apart from the statistical properties of a large number of trajectories, we also followed the motion of individual particles in the counterflow. In the specific range of temperatures and normal fluid velocities, we neatly observed that the particles intermittently switch between two distinct motion regimes (Fig. 3.10), associated with the bimodal distribution of the vertical particle velocity. A novel technique for the estimation of the normal fluid velocity, based solely on the observed particle dynamics, was developed. The method yields comparable results as Eq. (1.4), but it does not require information on the bath temperature and the applied heat flux.

Two motion regimes are typically associated with the particles that are trapped by the vortex tangle and the particles that travel undisturbed by quantized vor-

tices [105]. We introduced a custom separation scheme (Fig. 3.11) aimed to independently analyze the motion regimes and we showed that the particle-vortex interactions are more pervasive than previously thought. Signatures of these interactions are present in both motion regimes (Fig. 3.12), albeit the interaction strength differs between them. The study is published as a research article (Ref. [81]) and reproduced here as Attachment 4.

Counterflow jets are conceptually similar to the counterflow in a uniform channel. However, the flow field of the counterflow jets significantly differs from that in the channel counterflow, as both components of He II are coflowing in the volume above the nozzle (Fig. 4.1). We experimentally probed the vortex tangle embedded in the jet and we mapped its spatial distribution (Fig. 4.4) for the first time, to the best of the author's knowledge. The majority of the vortex tangle is localized within a cone, which is derived from the growth rate of radial profiles of the vortex line density and whose opening half-angle is found to be ca. 11.1°, regardless of the bath temperature or the applied heating power. The radial profiles are nearly-Gaussian, which is consistent with the corresponding velocity field.

The vortex line density measured along the jet axis displays a power-law decrease with the distance from the nozzle (Fig. 4.6). The corresponding exponent is found close to $-3/2$, which is compatible with the expected dependence of the fluid velocity. However, our preliminary data are not conclusive and a future study is likely required to validate the proposed dependence.

If a steady heating is substituted by short heat pulses, the experimental setup for counterflow jets can be used to thermally generate vortex rings in He II. We visualized and tracked the propagation of the rings that are about $10\,\mathrm{mm}$ in diameter by using the Lagrangian pseudovorticity (Eq. 5.4), a custom scalar field that is computed from the positions and velocities of the visualized particles. Time evolution of the ring trajectory and size is in good agreement with the similarity theory developed for turbulent rings propagating in a classical fluid [123] (Figs. 5.6 and 5.7). The tracking method, as well as the ring propagation, are further discussed in our publication [124], reproduced here as Attachment 5.

In order to probe the quantized vortex tangle embedded in the rings, we have successfully combined the particle tracking velocimetry and the second sound attenuation techniques in a single experiment (Fig. 5.8). In comparison to the previous study, the investigated vortex rings have a smaller diameter (ca. $4\,\mathrm{mm}$) and their wakes are more pronounced. The collected profiles of the vortex line density were found self-similar and highly reproducible (Figs. 5.9 and 5.11). They neatly reflect the ring–wake structure that passes between the second sound sensors. Parameters that describe individual profiles are related to the ring velocity and the total length of vortex lines produced by the heat pulse. We found that these parameters depend on the deposited heat and bath temperature (Fig. 5.12), although the physical interpretation of such behaviour is unclear at the moment.

Complementary visualization data confirm that a vortex ring develops after each heat pulse; the rings propagate vertically towards the second sound channel. The estimated size of the ring–wake structure (right panel of Fig. 5.14) is found to

grow with the distance from the nozzle, at the rate comparable to that of the counterflow jets, which suggests that the visualized particle motion is affected mainly by the turbulent wake.

To summarize, we believe that the presented thesis contributes to the understanding of several aspects of turbulent flows of He II. However, some of the outcomes are not definitive. In particular, our second sound studies, presented in §4.3 and §5.4, are mostly based on preliminary data and they leave several questions unanswered. We hope that such open problems will always stimulate the interest of the research community in quantum turbulence, a complex yet exciting branch of fluid dynamics.

Bibliography

[1] A. Tsinober. *An Informal Conceptual Introduction to Turbulence.* Springer, Dordrecht, 2009.

[2] L. F. Richardson. Atmospheric diffusion shown on a distance-neighbour graph. *Proceedings of the Royal Society of London A:*, 110:709–737, 1926.

[3] A. N. Kolmogorov. The local structure of turbulence in incompressible viscous fluid for very large Reynolds numbers. *Proceedings of the Royal Society of London A*, 434:9–13, 1991.

[4] P. Kapitza. Viscosity of liquid helium below the λ-point. *Nature*, 141:74, 1938.

[5] J. F. Allen and H. Jones. New phenomena connected with heat flow in helium II. *Nature*, 141:243–244, 1938.

[6] J. G. Daunt and K. Mendelssohn. Surface transport in liquid helium II. *Nature*, 143:719–720, 1939.

[7] M. S. Mongiovì, D. Jou, and M. Sciacca. Non-equilibrium thermodynamics, heat transport and thermal waves in laminar and turbulent superfluid helium. *Physics Reports*, 726:1–71, 2018.

[8] S. W. Van Sciver. *Helium Cryogenics.* Springer-Verlag, New York, 2012.

[9] L. Skrbek and K. R. Sreenivasan. Developed quantum turbulence and its decay. *Physics of Fluids*, 24:011301, 2012.

[10] R. P. Feynman. Application of quantum mechanics to liquid helium. In C. J. Gorter, editor, *Progress in Low Temperature Physics*, volume 1, pages 17–53. Elsevier, 1955.

[11] W. F. Vinen. The detection of single quanta of circulation in liquid helium II. *Proceedings of the Royal Society of London A*, 260:218–236, 1961.

[12] W. Guo, M. La Mantia, D. P. Lathrop, and S. W. Van Sciver. Visualization of two-fluid flows of superfluid helium-4. *Proceedings of the National Academy of Sciences*, 111:4653–4658, 2014.

[13] E. Varga, M. J. Jackson, D. Schmoranzer, and L. Skrbek. The use of second sound in investigations of quantum turbulence in He II. *Journal of Low Temperature Physics*, 197:130–148, 2019.

[14] M. S. Paoletti and D. P. Lathrop. Quantum turbulence. *Annual Review of Condensed Matter Physics*, 2:213–234, 2011.

[15] L. Tisza. Transport phenomena in helium II. *Nature*, 141:913, 1938.

[16] L. Landau. Theory of the superfluidity of helium II. *Physical Review*, 60:356–358, 1941.

[17] R. J. Donnelly. The two-fluid theory and second sound in liquid helium. *Physics Today*, 62:34, 2009.

[18] R. J. Donnelly and C. F. Barenghi. The observed properties of liquid helium at the saturated vapor pressure. *Journal of Physical and Chemical Reference Data*, 27:1218–1274, 1998.

[19] C. F. Barenghi, L. Skrbek, and K. R. Sreenivasan. Introduction to quantum turbulence. *Proceedings of the National Academy of Sciences*, 111:4647–4652, 2014.

[20] J. Maurer and P. Tabeling. Local investigation of superfluid turbulence. *Europhysics Letters*, 43:29–34, 1998.

[21] R. E. Honey, R. Hershberger, R. J. Donnelly, and D. Bolster. Oscillating-grid experiments in water and superfluid helium. *Physical Review E*, 89:053016, 2014.

[22] P. Švančara and M. La Mantia. Flows of liquid ^{4}He due to oscillating grids. *Journal of Fluid Mechanics*, 832:578–599, 2017.

[23] D. Schmoranzer, M. J. Jackson, Š. Midlik, M. Skyba, J. Bahyl, T. Skokánková, V. Tsepelin, and L. Skrbek. Dynamical similarity and instabilities in high-Stokes-number oscillatory flows of superfluid helium. *Physical Review B*, 99:054511, 2019.

[24] D. I. Bradley, R. George, A. M. Guénault, R. P. Haley, S. Kafanov, M. T. Noble, Yu. A. Pashkin, G. R. Pickett, M. Poole, J. R. Prance, M. Sarsby, R. Schanen, V. Tsepelin, T. Wilcox, and D. E. Zmeev. Operating nanobeams in a quantum fluid. *Scientific Reports*, 7:4876, 2017.

[25] M. La Mantia and L. Skrbek. Quantum turbulence visualized by particle dynamics. *Physical Review B*, 90:014519, 2014.

[26] C. J. Gorter and J. H. Mellink. On the irreversible processes in liquid helium II. *Physica*, 15:285–304, 1949.

[27] E. Varga, S. Babuin, and L. Skrbek. Second-sound studies of coflow and counterflow of superfluid ^{4}He in channels. *Physics of Fluids*, 25:065101, 2015.

[28] S. Babuin, M. Stammeier, E. Varga, M. Rotter, and L. Skrbek. Quantum turbulence of bellows-driven ^{4}He superflow: Steady state. *Physical Review B*, 86:134515, 2012.

[29] Y. A. Sergeev, C. F. Barenghi, and D. Kivotides. Motion of micron-size particles in turbulent helium II. *Physical Review B*, 74:184506, 2006.

[30] K. W. Schwarz. Turbulence in superfluid helium: Steady homogeneous counterflow. *Physical Review B*, 18:245–262, 1978.

[31] M. La Mantia. Particle trajectories in thermal counterflow of superfluid helium in a wide channel of square cross section. *Physics of Fluids*, 28:024102, 2016.

[32] S. Babuin, E. Varga, L. Skrbek, E. Lévêque, and P.-E. Roche. Effective viscosity in quantum turbulence: A steady-state approach. *Europhysics Letters*, 106:24006, 2014.

[33] D. V. Osborne. The rotation of liquid helium II. *Proceedings of the Physical Society of London A*, 63:909, 1950.

[34] G. P. Bewley, D. Lathrop, and K. R. Sreenivasan. Visualization of quantized vortices. *Nature*, 441:588, 2006.

[35] A. W. Baggaley, J. Laurie, and C. F. Barenghi. Vortex-density fluctuations, energy spectra, and vortical regions in superfluid turbulence. *Physical Review Letters*, 109:205304, 2012.

[36] E. Rusaouen, B. Rousset, and P.-E. Roche. Detection of vortex coherent structures in superfluid turbulence. *Europhysics Letters*, 118:14005, 2017.

[37] J. Salort, B. Chabaud, E. Lévêque, and P.-E. Roche. Energy cascade and the four-fifths law in superfluid turbulence. *Europhysics Letters*, 97:34006, 2012.

[38] N. P. Müller, J. I. Polanco, and G. Krstulovic. Intermittency of velocity circulation in quantum turbulence. *Physical Review X*, 11:011053, 2021.

[39] C. F. Barenghi, V. S. L'vov, and P.-E. Roche. Experimental, numerical, and analytical velocity spectra in turbulent quantum fluid. *Proceedings of the National Academy of Sciences*, 111:4683–4690, 2014.

[40] D. Kivotides, J. C. Vassilicos, D. C. Samuels, and C. F. Barenghi. Kelvin waves cascade in superfluid turbulence. *Physical Review Letters*, 86:3080–3083, 2001.

[41] W. F. Vinen, M. Tsubota, and A. Mitani. Kelvin-wave cascade on a vortex in superfluid ^{4}He at a very low temperature. *Physical Review Letters*, 91:135301, 2003.

[42] K. Morris, J. Koplik, and D. W. I. Rouson. Vortex locking in direct numerical simulations of quantum turbulence. *Physical Review Letters*, 101:015301, 2008.

[43] P.-E. Roche, C. F. Barenghi, and E. Lévêque. Quantum turbulence at finite temperature: The two-fluids cascade. *Europhysics Letters*, 87:54006, 2009.

[44] L. Galantucci, A. W. Baggaley, C. F. Barenghi, and G. Krstulovic. A new self-consistent approach of quantum turbulence in superfluid helium. *The European Physical Journal Plus*, 135:547, 2020.

[45] S. W. Van Sciver and C. F. Barenghi. Visualization of quantum turbulence. In M. Tsubota and W. P. Halperin, editors, *Progress in Low Temperature Physics*, volume 16, pages 247–303. Elsevier, 2009.

[46] M. Raffel, Ch. E. Willert, S. Wereley, and J. Kompenhans. *Particle Image Velocimetry – A Practical Guide*. Springer-Verlag, Berlin, Heidelberg, 2007.

[47] T. Dracos. *Three-Dimensional Velocity and Vorticity Measuring and Image Analysis Techniques*, chapter Particle Tracking Velocimetry (PTV). Springer, Dordrecht, 1996.

[48] M. R. Maxey and J. J. Riley. Equation of motion for a small rigid sphere in a nonuniform flow. *Physics of Fluids*, 26:883, 1983.

[49] F. Toschi and E. Bodenschatz. Lagrangian properties of particles in turbulence. *Annual Review of Fluid Mechanics*, 41:375–404, 2009.

[50] T. Zhang, D. Celik, and S. W. Van Sciver. Tracer particles for application to PIV studies of liquid helium. *Journal of Low Temperature Physics*, 134:985–1000, 2004.

[51] R. J. Donnelly, A. N. Karpetis, J. J. Niemela, K. R. Sreenivasan, W. F. Vinen, and C. M. White. The use of particle image velocimetry in the study of turbulence in liquid helium. *Journal of Low Temperature Physics*, 126:327–332, 2002.

[52] T. Zhang and S. W. Van Sciver. Large-scale turbulent flow around a cylinder in counterflow superfluid ^{4}He (He(II)). *Nature Physics*, 1:36–38, 2005.

[53] T. Zhang and S. W. Van Sciver. The motion of micron-sized particles in He II counterflow as observed by the PIV technique. *Journal of Low Temperature Physics*, 138:865–870, 2005.

[54] D. P. Meichle and D. P. Lathrop. Nanoparticle dispersion in superfluid helium. *Review of Scientific Instruments*, 85:073705, 2014.

[55] D. Celik and S. W. Van Sciver. Tracer particle generation in superfluid helium through cryogenic liquid injection for particle image velocimetry (PIV) applications. *Experimental Thermal and Fluid Science*, 26:971–975, 2002.

[56] E. Fonda, K. R. Sreenivasan, and D. P. Lathrop. Sub-micron solid air tracers for quantum vortices and liquid helium flows. *Review of Scientific Instruments*, 87:025106, 2016.

[57] O. Bostanjoglo and R. Kleinschmidt. Crystal structure of hydrogen isotopes. *The Journal of Chemical Physics*, 46:2004–2005, 1967.

[58] K. L. Chopra and J. B. Brown. Suspension of particles in liquid helium. *Physical Review*, 108:157, 1957.

[59] M. Murakami and N. Ichikawa. Flow visualization study of thermal counterflow jet in He II. *Cryogenics*, 29:438–443, 1989.

[60] M. La Mantia, T. V. Chagovets, M. Rotter, and L. Skrbek. Testing the performance of a cryogenic visualization system on thermal counterflow by using hydrogen and deuterium solid tracers. *Review of Scientific Instruments*, 83:055109, 2012.

[61] P. Švančara, P. Hrubcová, M. Rotter, and M. La Mantia. Visualization study of thermal counterflow of superfluid helium in the proximity of the heat source by using solid deuterium hydride particles. *Physical Review Fluids*, 3:114701, 2018.

[62] G. P. Bewley. The generation of particles to observe quantized vortex dynamics in superfluid helium. *Cryogenics*, 49:549–553, 2009.

[63] D. R. Poole, C. F. Barenghi, Y. A. Sergeev, and W. F. Vinen. Motion of tracer particles in He II. *Physical Review B*, 71:064514, 2005.

[64] Y. Tagawa, J. M. Mercado, V. N. Prakash, W. Calzavarini, C. Sun, and D. Lohse. Three-dimensional Lagrangian Voronoï analysis for clustering of particles and bubbles in turbulence. *Journal of Fluid Mechanics*, 693:201–215, 2012.

[65] R. Monchaux, M. Bourgoin, and A. Cartellier. Preferential concentration of heavy particles: A Voronoï analysis. *Physics of Fluids*, 22:103304, 2010.

[66] J. I. Polanco and G. Krstulovic. Inhomogeneous distribution of particles in coflow and counterflow quantum turbulence. *Physical Review Fluids*, 5:032601(R), 2020.

[67] Y. A. Sergeev and C. F. Barenghi. Particles-vortex interactions and flow visualization in ^{4}He. *Journal of Low Temperature Physics*, 157:429–475, 2009.

[68] G. P. Bewley, K. R. Sreenivasan, and D. P. Lathrop. Particles for tracing turbulent liquid helium. *Experiments in Fluids*, 44:887–896, 2008.

[69] M. La Mantia, P. Švančara, D. Duda, and L. Skrbek. Small-scale universality of particle dynamics in quantum turbulence. *Physical Review B*, 94:184512, 2016.

[70] N. T. Ouellette, H. Xu, and E. Bodenschatz. A quantitative study of three-dimensional Lagrangian particle tracking algorithms. *Experiments in Fluids*, 40:301–313, 2006.

[71] I. F. Sbalzarini and P. Koumoutsakos. Feature point tracking and trajectory analysis for video imaging in cell biology. *Journal of Structural Biology*, 151:182–195, 2005.

[72] N. Mordant, A. M. Crawford, and E. Bodenschatz. Experimental Lagrangian acceleration probability density function measurement. *Physica D*, 193:245–251, 2004.

[73] P. Švančara, P. Hrubcová, and M. La Mantia. Estimation of Lagrangian velocities in thermal counterflow of superfluid helium. In J. Šafránková and J. Pavlů, editors, *WDS'18 Proceedings of Contributed Papers – Physics*, pages 168–173, Prague, 2018.

[74] M. La Mantia and L. Skrbek. Quantum, or classical turbulence? *Europhysics Letters*, 105:46002, 2014.

[75] P.-E. Roche, P. Diribarne, T. Didelot, O. Français, L. Rousseau, and H. Willaime. Vortex density spectrum of quantum turbulence. *Europhysics Letters*, 77:66002, 2007.

[76] Š. Midlik, D. Schmoranzer, and L. Skrbek. Transition to quantum turbulence in oscillatory thermal counterflow of ^{4}He. *Physical Review B*, 103:134516, 2021.

[77] G. Taubin. Estimation of planar curves, surfaces, and nonplanar space curves defined by implicit equations with applications to edge and range image segmentation. *IEEE Transactions on Pattern Analysis and Machine Intelligence*, 13:1115–1138, 1991.

[78] E. Woillez and P.-E. Roche. Local measurement of vortex statistics in quantum turbulence. *arXiv:2102.10866*, February 2021.

[79] P. Hrubcová, P. Švančara, and M. La Mantia. Vorticity enhancement in thermal counterflow of superfluid helium. *Physical Review B*, 97:064512, 2018.

[80] P. Švančara and M. La Mantia. Flight-crash events in superfluid turbulence. *Journal of Fluid Mechanics*, 876:R2, 2019.

[81] P. Švančara, D. Duda, P. Hrubcová, M. Rotter, L. Skrbek, M. La Mantia, E. Durozoy, P. Diribarne, B. Rousset, M. Bourgoin, and M. Gibert. Ubiquity of particle–vortex interactions in turbulent counterflow of superfluid helium. *Journal of Fluid Mechanics*, 911:A8, 2021.

[82] M. S. Paoletti, M. E. Fisher, K. R. Sreenivasan, and D. P. Lathrop. Velocity statistics distinguish quantum turbulence from classical turbulence. *Physical Review Letters*, 101:154501, 2008.

[83] N. Mordant, E. Lévêque, and J.-F. Pinton. Experimental and numerical study of the Lagrangian dynamics of high Reynolds turbulence. *New Journal of Physics*, 6:116, 2004.

[84] I. Marusic, B. J. McKeon, P. A. Monkewitz, H. M. Nagib, A. J. Smits, and K. R. Sreenivasan. Wall-bounded turbulent flows at high Reynolds numbers: Recent advances and key issues. *Physics of Fluids*, 22:065103, 2010.

[85] A. W. Baggaley and S. Laizet. Vortex line density in counterflowing He II with laminar and turbulent normal fluid velocity profiles. *Physics of Fluids*, 25:115101, 2013.

[86] A. W. Baggaley and J. Laurie. Thermal counterflow in a periodic channel with solid boundaries. *Journal of Low Temperature Physics*, 178:35–52, 2015.

[87] T. Xu and S. W. Van Sciver. Particle image velocimetry measurements of the velocity profile in He II forced flow. *Physics of Fluids*, 19:071703, 2007.

[88] G. W. Stagg, N. G. Parker, and C. F. Barenghi. Superfluid boundary layer. *Physical Review Letters*, 118:135301, 2017.

[89] M. La Mantia. Particle dynamics in wall-bounded thermal counterflow of superfluid helium. *Physics of Fluids*, 29:065102, 2017.

[90] E. Varga. *Experimental and numerical investigation of quantum turbulence in He II*. Doctoral thesis, Charles University, 2018.

[91] J. Bertolaccini, E. Lévêque, and P.-E. Roche. Disproportionate entrance length in superfluid flows and the puzzle of counterflow instabilities. *Physical Review Fluids*, 2:123902, 2017.

[92] M. La Mantia, D. Duda, M. Rotter, and L. Skrbek. Lagrangian accelerations of particles in superfluid turbulence. *Journal of Fluid Mechanics*, 717:R9, 2013.

[93] H. Schlichting and K. Gersten. *Boundary-Layer Theory*. Springer, Berlin, 2017.

[94] E. Varga, S. Babuin, V. S. L'vov, A. Pomyalov, and L. Skrbek. Transition to quantum turbulence and streamwise inhomogeneity of vortex tangle in thermal counterflow. *Journal of Low Temperature Physics*, 187:531–537, 2017.

[95] H. Xu, A. Pumir, G. Falkovich, E. Bodenschatz, M. Shats, H. Xia, N. Francois, and G. Boffetta. Flight-crash events in turbulence. *Proceedings of the National Academy of Sciences*, 111:7558–7563, 2014.

[96] A. Pumir, H. Xu, E. Bodenschatz, and R. Grauer. Single-particle motion and vortex stretching in three-dimensional turbulent flows. *Physical Review Letters*, 116:124502, 2016.

[97] P. Clark di Leoni, P. D. Mininni, and M. E. Brachet. Dual cascade and dissipation mechanisms in helical quantum turbulence. *Physical Review A*, 95:053636, 2017.

[98] E. Lévêque and A. Naso. Introduction of longitudinal and transverse Lagrangian velocity increments in homogeneous and isotropic turbulence. *Europhysics Letters*, 108:54004, 2014.

[99] S. Zuccher, M. Caliari, A. W. Baggaley, and C. F. Barenghi. Quantum vortex reconnections. *Physics of Fluids*, 24:125108, 2012.

[100] A. Villois, D. Proment, and G. Krstulovic. Universal and nonuniversal aspects of vortex reconnections in superfluids. *Physical Review Fluids*, 2:044701, 2017.

[101] M. S. Paoletti, M. E. Fisher, and D. P. Lathrop. Reconnection dynamics for quantized vortices. *Physica D*, 239:1367–1377, 2010.

[102] M. S. Paoletti, R. B. Fioritto, K. R. Sreenivasan, and D. P. Lathrop. Visualization of superfluid helium flow. *Journal of the Physical Society of Japan*, 77:111007, 2008.

[103] T. V. Chagovets and S. W. Van Sciver. A study of thermal counterflow using particle tracking velocimetry. *Physics of Fluids*, 23:107102, 2011.

[104] D. Kivotides. Motion of a spherical solid particle in thermal counterflow turbulence. *Physical Review B*, 77:174508, 2008.

[105] B. Mastracci and W. Guo. Exploration of thermal counterflow in He II using particle tracking velocimetry. *Physical Review Fluids*, 3:063304, 2018.

[106] D. Kivotides. Normal-fluid velocity measurement and superfluid vortex detection in thermal counterflow turbulence. *Physical Review B*, 78:224501, 2008.

[107] A. Marakov, J. Gao, W. Guo, S. W. Van Sciver, G. G. Ihas, D. N. McKinsey, and W. F. Vinen. Visualization of the normal-fluid turbulence in counterflowing superfluid ^{4}He. *Physical Review B*, 91:094503, 2015.

[108] J. H. W. Lee and V. H. Chu. *Turbulent Jets and Plumes*, chapter Turbulent Jets. Springer, Boston, 2003.

[109] I. Wygnanski and H. Fiedler. Some measurements in the self-preserving jet. *Journal of Fluid Mechanics*, 38:577–612, 1969.

[110] D. Duri, J. Salort, P. Diribarne, P.-E. Roche, and C. Baudet. Vorticity scattering measurements in a superfluid inertial round jet. *Journal of Physics: Conference Series*, 318:092027, 2011.

[111] H. W. Liepmann and G. A. Laguna. Nonlinear interactions in the fluid mechanics of helium II. *Annual Review of Fluid Mechanics*, 16:139–177, 1984.

[112] G. Careri, M. Cerdonio, and F. Dupré. Vorticity in liquid He II flow through orifices. *Physical Review*, 167:233–238, 1968.

[113] P. E. Dimotakis and J. E. Broadwell. Local temperature measurements in supercritical counterflow in liquid helium II. *Physics of Fluids*, 16:1787–1795, 1973.

[114] G. A. Laguna. Second-sound attenuation in a supercritical jet. *Physical Review B*, 12:4874–4881, 1975.

[115] P. E. Dimotakis and G. A. Laguna. Investigations of turbulence in a liquid helium II counterflow jet. *Physical Review B*, 15:5240–5244, 1977.

[116] A. Nakano and M. Murakami. Velocity measurement of He II thermal counterflow jet accompanied by second sound Helmholtz oscillation. *Cryogenics*, 34:179–185, 1994.

[117] A. Nakano, M. Murakami, and K. Kunisada. Flow structure of thermal counterflow jet in He II. *Cryogenics*, 34:991–995, 1994.

[118] M. Murakami, T. Takakoshi, M. Maeda, and A. Nakano. PIV measurement result of superfluid He II thermal counterflow jet. *AIP Conference Proceedings*, 985:183–190, 2008.

[119] C. G. Ball, H. Fellouah, and A. Pollard. The flow field in turbulent round free jets. *Progress in Aerospace Sciences*, 50:1–26, 2012.

[120] S. S. Aleyasin, M. F. Tachie, and M. Koupriyanov. PIV measurements in the near and intermediate field regions of jets issuing from eight different nozzle geometries. *Flow, Turbulence and Combustion*, 99:329–351, 2017.

[121] T. T. Lim and T. B. Nickels. *Fluid Vortices*, chapter Vortex Rings. Springer, Dordrecht, 1995.

[122] C. F. Barenghi and R. J. Donnelly. Vortex rings in classical and quantum systems. *Fluid Dynamics Research*, 41:051401, 2009.

[123] A. Glezer and D. Coles. An experimental study of a turbulent vortex ring. *Journal of Fluid Mechanics*, 211:243–283, 1990.

[124] P. Švančara, M. Pavelka, and M. La Mantia. An experimental study of turbulent vortex rings in superfluid ^{4}He. *Journal of Fluid Mechanics*, 889:A24, 2020.

[125] A. Glezer. The formation of vortex rings. *Physics of Fluids*, 31:3532–3542, 1988.

[126] G. Stamm, F. Bielert, W. Fiszdon, and J. Piechna. On the existence of counterflow induced macroscopic vortex rings in He II. *Physica B*, 194–196:589–590, 1994.

[127] M. Murakami, M. Hanada, and T. Yamazaki. Flow visualization study on large-scale vortex ring in He II. *Japanese Journal of Applied Physics*, 26:107, 1987.

[128] H. Borner, T. Schmeling, and D. W. Schmidt. Experiments on the circulation and propagation of largescale vortex rings in He II. *Physics of Fluids*, 26:1410, 1983.

[129] H. Borner and D. W. Schmidt. Investigation of large-scale vortex rings in He II by acoustic measurements of circulation. In G. E. A. Meier and F. Obermeier, editors, *Flow of Real Fluids*, pages 135–146, Springer, Berlin, Heidelberg, 1985.

[130] G. Stamm, F. Bielert, W. Fiszdon, and J. Piechna. Counterflow-induced macroscopic vortex rings in superfluid helium: Visualization and numerical simulation. *Physica B*, 193:188–194, 1994.

[131] D. H. Wacks, A. W. Baggaley, and C. F. Barenghi. Large-scale superfluid vortex rings at nonzero temperatures. *Physical Review B*, 90:224514, 2014.

[132] T. Maxworthy. Some experimental studies of vortex rings. *Journal of Fluid Mechanics*, 81:465–495, 1977.

[133] M. Gharib, E. Rambod, and K. Shariff. A universal time scale for vortex ring formation. *Journal of Fluid Mechanics*, 360:121–140, 1998.

[134] D. Duda, P. Švančara, M. La Mantia, M. Rotter, and L. Skrbek. Visualization of viscous and quantum flows of liquid ^{4}He due to an oscillating cylinder of rectangular cross section. *Physical Review B*, 92:064519, 2015.

[135] L. Gan and T. B. Nickels. An experimental study of turbulent vortex rings during their early development. *Journal of Fluid Mechanics*, 649:467–496, 2010.

[136] T. Maxworthy. Turbulent vortex rings. *Journal of Fluid Mechanics*, 64:227–239, 1974.

List of Abbreviations

CMOS .... Complementary metal-oxide semiconductor

FOV .... Field of view

NTC .... Negative temperature coefficient

PDF .... Probability density function

PID .... Proportional-integral-derivative (controller)

PIV .... Particle imaging velocimetry

PLA .... Polylactic acid

PTV .... Particle tracking velocimetry

RMS .... Root mean square

VLD .... Vortex line density

List of Publications

Publications [A–E] are directly related to the presented thesis and are reproduced as Attachments 1–5.

[A] P. Švančara, D. Duda, P. Hrubcová, M. Rotter, L. Skrbek, M. La Mantia, E. Durozoy, P. Diribarne, B. Rousset, M. Bourgoin, and M. Gibert. Ubiquity of particle-vortex interactions in turbulent counterflow of superfluid helium. *Journal of Fluid Mechanics*, 911:A8, 2021.

[B] P. Švančara, M. Pavelka, and M. La Mantia. An experimental study of turbulent vortex rings in superfluid ^{4}He. *Journal of Fluid Mechanics*, 889:A24, 2020.

[C] P. Švančara and M. La Mantia. Flight-crash events in superfluid turbulence. *Journal of Fluid Mechanics*, 876:R2, 2019.

[D] P. Švančara, P. Hrubcová, M. Rotter, and M. La Mantia. Visualization study of thermal counterflow of superfluid helium in the proximity of the heat source by using solid deuterium hydride particles. *Physical Review Fluids* 3:114701, 2018.

[E] P. Hrubcová, P. Švančara, and M. La Mantia. Vorticity enhancement in thermal counterflow of superfluid helium. *Physical Review B*, 97:64512, 2018.

[F] D. Duda, P. Švančara, M. La Mantia, M. Rotter, D. Schmoranzer, O. Kolosov, and L. Skrbek. Cavitation bubbles generated by vibrating quartz tuning fork in liquid ^{4}He close to the λ-transition. *Journal of Low Temperature Physics*, 187:376–382, 2017.

[G] P. Švančara and M. La Mantia. Flows of liquid ^{4}He due to oscillating grids. *Journal of Fluid Mechanics*, 832:578–599, 2017.

[H] M. La Mantia, P. Švančara, D. Duda, and L. Skrbek. Small-scale universality of particle dynamics in quantum turbulence. *Physical Review B*, 94:184512, 2016.

[I] D. Duda, P. Švančara, M. La Mantia, M. Rotter, and L. Skrbek. Visualization of viscous and quantum flows of liquid ^{4}He due to an oscillating cylinder of rectangular cross section. *Physical Review B*, 92:64519, 2015.

Attachments

1. Vorticity enhancement in thermal counterflow of superfluid helium

2. Visualization study of thermal counterflow of superfluid helium in the proximity of the heat source by using solid deuterium hydride particles

3. Flight-crash events in superfluid turbulence

4. Ubiquity of particle-vortex interactions in turbulent counterflow of superfluid helium

5. An experimental study of turbulent vortex rings in superfluid ^{4}He